MOBILE MAX-DOAS MEASUREMENTS OF THE TROPOSPHERIC FORMALDEHYDE COLUMN IN THE RHEIN - MAIN REGION

Sebastian Donner

20th May 2016

Master - Thesis

Max Planck Institute for Chemistry
Satellite Group

submitted to the Institute for Atmospheric Physics
of the Johannes Gutenberg University Mainz

SUPERVISORS:
Prof. Dr. Thomas Wagner
Prof. Dr. Peter Hoor

Declaration/ Erklärung

I hereby declare that this thesis is my own work, except where explicitly stated otherwise in the text or in the bibliography. This work has not been submitted in whole, or in a similar way, for any other degree.

Hiermit versichere ich die vorliegende Arbeit selbstständig und unter ausschließlicher Verwendung der angegebenen Literatur und Hilfsmittel erstellt zu haben. Die Arbeit wurde bisher in gleicher oder ähnlicher Form keiner anderen Prüfungsbehörde vorgelegt und auch nicht veröffentlicht.

Mainz, den 20. Mai 2016

Sebastian Donner
Am Rodelberg 55
55131 Mainz
sdonner@students.uni-mainz.de
Matrikelnummer: 2672593

Abstract

This thesis deals with mobile MAX-DOAS measurements which were performed in the Frankfurt/Rhein-Main area in winter 2015/spring 2016 and in Romania in summer 2015. The focus of this thesis is on the tropospheric formaldehyde column.

Two instruments were used for the measurements but in the following we concentrate on the new and better TubeMAX-DOAS instrument. First, the instrumental setup of this new instrument is explained and some basic properties of the measuring system are characterised. Here the most important finding is that the detector exhibits a non linear response to the incident photons. This effect was found to be in the order of 5% and further a correction method was developed and applied.

Then the settings for the spectral analysis are presented and sensitivity tests are performed. Effects which potentially influence the DOAS fit result are investigated. The fit results for both used instruments are compared and substantially better results are found for the new TubeMAX-DOAS instrument.

After the instrument characterisation is completed the results for the measurements in the Frankfurt/Rhein-Main area are investigated. First, the spatial distribution of HCHO around the three major measurement sites (Mainz, Frankfurt/Main and the Frankfurt Airport) is presented. Next the spatial HCHO distribution is correlated to the NO_2 distribution. Overall spatial patterns fitting the prevailing wind patterns are found. Also a close relationship between the distributions of both trace gases can be observed.

Thereafter emission ratios (HCHO/NO_x) are determined following the procedure from Klemp et al. (2002). In addition to daily ratios, mean emission ratios are calculated. Here values of 0.060, 0.060, 0.059 and 0.069 are obtained. Klemp et al. (2002) obtained emission ratios in a range from 0.029 to 0.037 which are lower values. However, this systematic difference seems to be reasonable as we used a different measurement method and performed measurements in both the in- and outflow of the cities. Accounting for all these differences we find quite reasonable results also in comparison to another study from Slemr et al. (1996) who found an emission ratio of 0.050 in the plume of Freiburg.

Finally, the results from the Rhein-Main measurements are compared to the Bucharest data. Also here consistent spatial patterns are found, but higher DSCDs are observed for Bucharest. The spatial distributions of HCHO and NO_2 are less clearly correlated than for the measurements in the Rhein-Main region. Also emission ratios are calculated for the three measurement days around Bucharest and no consistent values can be identified. These findings indicate that the influence of secondary produced formaldehyde from both anthropogenic and biogenic sources plays a more important role than in the Rhein-Main region in winter.

Zusammenfassung

In Rahmen dieses Masterarbeits-Projekts wurden im Winter 2015/Frühling 2016 in der Metropolregion Frankfurt/Rhein-Main sowie im Sommer 2015 in Rumänien mobile MAX-DOAS Messungen durchgeführt. Dabei liegt der Focus dieser Arbeit auf der troposphärischen HCHO-Säule.

Für die Messungen wurden zwei Instrumente verwendet, dennoch wird sich in dieser Arbeit auf die Ergebnisse des neuen und besseren TubeMAX-DOAS Instruments konzentriert. Zunächst werden einige grundlegende Eigenschaften des Messaufbaus des neuen Instruments charakterisiert. Dabei ist die wichtigste Erkenntnis, dass das verwendete Spektrometer einen nicht-linearen Zusammenhang zwischen seinem Signal und den einfallenden Photonen aufweist. Dieser Effekt hat eine Größe von 5 %, daher wurde eine Korrekturmethode entwickelt und angewandt.

Danach werden die Einstellungen für die spektrale Analyse beschrieben und es werden Sensitivitätsstudien durchgeführt. Dabei werden Effekte, die das Fitergebnis beeinflussen könnten, genauer untersucht. Zusätzlich wurden die Fitergebnisse der beiden verwendeten Messgeräte verglichen, wobei sich deutlich bessere Ergebnisse für das neuen TubeMAX-DOAS-Instrument ergaben.

Nach der Charakterisierung werden die Ergebnisse für die Messungen in der Metropolregion Frankfurt/Rhein-Main untersucht. Dabei wird zuerst die räumliche Verteilung von HCHO um die drei Hauptmessorte (Mainz, Frankfurt/Main und den Frankfurter Flughafen) präsentiert. Danach wird diese mit der NO_2-Verteilung korreliert. Insgesamt passen die beobachteten räumlichen Verteilungen der beiden Spurengase gut zu den vorherrschenden Windmustern. Zudem kann eine gute Korrelation der Verteilungen beider Stoffe beobachtet werden.

Danach wurden Emissions-Verhältnisse ($HCHO/NO_x$) nach einer Methode von Klemp et al. (2002) berechnet. Zusätzlich zu täglichen Emissions-Verhältnissen, werden mittlere Emissions-Verhältnisse bestimmt. Dabei erhält man folgende Werte für die Verhältnisse: 0.060, 0.060, 0.059 und 0.069. Klemp et al. (2002) hingegen erhalten deutlich niedrigere Emissions-Verhältnisse im Bereich von 0.029 bis 0.037. Diese systematischen Unterschiede sind dadurch erklärbar, dass wir ein passives Messverfahren verwenden und Daten sowohl aus dem In- als auch aus dem Outflow für die Berechnung heranziehen. Werden all diese Unterschiede berücksichtigt, erhalten wir vergleichbare Ergebnisse zu Klemp et al. (2002) und Slemr et al. (1996). Slemr et al. (1996) erhalten ein Emissions-Verhältnis von 0.050 im Outflow der Stadt Freiburg.

Schließlich werden die Ergebnisse der Rhein-Main-Messungen mit Daten verglichen, die bei Messfahrten in Bukarest aufgenommen wurden. Auch hier konnten konsistente räumliche Muster identifiziert werden, wobei sich für diese Messungen deutlich höhere DSCDs als bei den Messungen im Rhein-Main-Gebiet ergaben. Außerdem weichen die räumlichen Muster von HCHO und NO_2 mehr voneinander ab. Zusätzlich werden auch für die Bukarest Messungen Emissions-Verhältnisse berechnet, wobei sich allerdings keine konsistenten Ergebnisse zeigen. All diese Ergebnisse deuten auf den Einfluss von sekundär erzeugtem Formaldehyd hin, der sowohl anthropogenen also auch biogenen Ursprungs sein kann.

Contents

1. Motivation

The earth's atmosphere consists of two major constituents, namely oxygen and nitrogen. These two gases together with argon and carbon dioxide account for nearly $100\,\%$ of the volume of the earth's atmosphere (Kraus, 2007). Besides these gases a plenty of so-called trace gases are present in the atmosphere. Despite the fact that they only account for around $3 \times 10^{-5}\,\%$ of the volume of the earth's atmosphere, they heavily impact the radiation properties and the chemical processes within the atmosphere (Kraus, 2007). Especially the trace gases located in the troposphere, where a large fraction of the life on the earth can be found, are even more important as many of them are harmful for living beings. Therefore, it is of major importance to learn more about the composition of the troposphere and the processes which control it.

For this purpose different measurement methods are available, however, for many applications remote sensing techniques are best suited as they allow to cover large areas. Here one example are satellite measurements which provide information on the composition of the atmosphere with a good global coverage. Also some of them like the Global Ozone Monitoring Experiment 1 and 2 (GOME-1 and 2), the Scanning Imaging Absorption Spectrometer for Atmospheric Cartography (SCIAMACHY), and the Ozone Monitoring Instrument (OMI) allow to retrieve information of tropospheric trace gases on a global scale. But these data products exhibit still quite large uncertainties. Therefore, the validation of those satellite products is very important in order to quantify and improve their quality.

Very often ground-based measurements are used for this validation work. These measurements are mostly performed at one fixed location and usually represent a much smaller area than the (typically much larger) satellite footprints. Thus horizontal gradients, which are typical close to strong emission sources, have a strong effect on the validation results. Mobile MAX (Multi AXis)- DOAS (Differential Optical Absorption Spectroscopy) measurements (Hönninger and Platt (2002), Hönninger et al. (2004) and Shaiganfar et al. (2011)) of tropospheric trace gases are one good tool to cover the whole extent of a satellite ground pixel in a short period of time. This makes it possible to map existing gradients and thus to improve the validation results. Furthermore, mobile MAX-DOAS measurements can be used to estimate emissions from cities and other emission sources (Ibrahim et al., 2010). In addition, this technique is a good way to map the spatial distribution of tropospheric trace gases like HCHO and NO_2.

During this Master-Thesis project mobile MAX-DOAS measurements were performed in Romania in August/September 2015 and in the Frankfurt/Rhein-Main region from October 2015 till March 2016. In this project the focus was on the tropospheric formaldehyde (HCHO) column as this trace gas is highly involved in tropospheric chemistry.

2. Theory

This chapter gives an overview on the theoretical background of this work. First, the DOAS method is introduced (section 2.1). The second part of the chapter then describes the MAX-DOAS technique (section 2.2). Finally, some properties of the solar spectrum are summarised (section 2.3).

2.1. Differential Optical Absorption Spectroscopy (DOAS)

First, this section introduces absorption spectroscopy in general. Then the basic idea of the Differential Optical Absorption Spectroscopy (DOAS) method is explained in more detail.

2.1.1. Absorption Spectroscopy[1]

When electromagnetic radiation (light) is passing through a medium its intensity is attenuated. This attenuation is caused by the absorption (typically scattering can be ignored for short light paths) of the molecules (here gas molecules) inside the medium and can be described by Lambert-Beer's law:

$$I(\lambda, L) = I_0(\lambda) \cdot \exp\left[-\sigma\left(\lambda\right) \cdot c \cdot L\right] \tag{2.1}$$

Here $I_0(\lambda)$ is the initial intensity of the incident light, while $I(\lambda, L)$ denotes the intensity after passing through the medium with the thickness L. c describes the concentration of the absorber which has a absorption cross-section $\sigma\left(\lambda\right)$. This absorption cross-section is a function of wavelength λ and a characteristic property of any species. If all these quantities are known the concentration c can be obtained by the measured ratio $\frac{I_0(\lambda)}{I(\lambda,L)}$. Rearranging equation 2.1 yields:

$$c = \frac{\ln\left(\frac{I_0(\lambda)}{I(\lambda,L)}\right)}{\sigma(\lambda) \cdot L} = \frac{\tau}{\sigma(\lambda) \cdot L} \tag{2.2}$$

The quantity $\tau = \ln\left(\frac{I_0(\lambda)}{I(\lambda,L)}\right)$ is called optical density. Figure 2.1 summarises Lambert-Beer's law.

Under laboratory conditions, where $I_0(\lambda)$ and $I(\lambda, L)$ can be easily determined, equation 2.2 is sufficient to derive the concentration c.

However, if we want to infer trace gas concentrations in the open atmosphere there are certain problems with using the equations mentioned above. First, it is nearly impossible

---

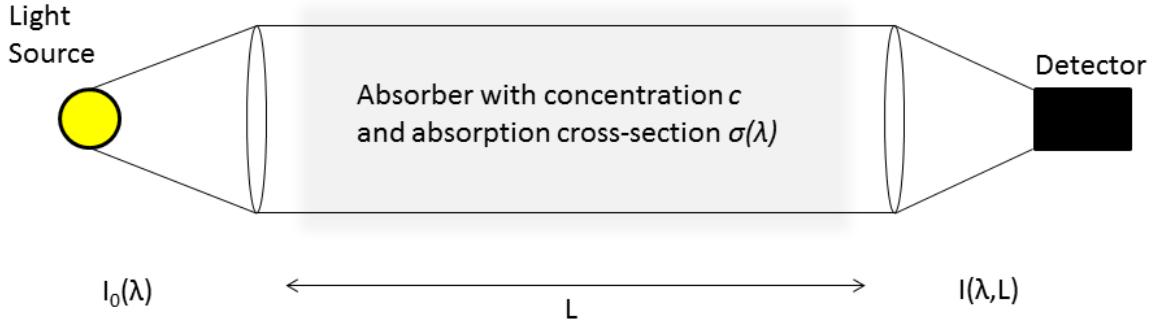[1]The information in this section is taken from Platt and Stutz (2008).

Figure 2.1.: Sketch to illustrate Lambert-Beer's law. Light emitted by a light source passes through a medium and the attenuated intensity is measured by a detector, adopted from Platt and Stutz (2008).

to determine the intensity $I_0(\lambda)$ as the light measured at the earth's surface always passes through the atmosphere. Further, the light is not only attenuated by absorption but also by scattering caused by particles in the atmosphere. In order to deal with this problems the so-called DOAS method is used.

2.1.2. The DOAS Principle[2]

As mentioned in the previous section it is difficult to apply classic absorption spectroscopy in the open atmosphere. If we want to use Lambert-Beer's law to investigate the composition of the atmosphere we have to adjust it and to take several aspects into account.

First, the atmosphere is composed of several gases which all have different concentrations and absorption cross-sections. Further, also scattering by air molecules and aerosol particles leads to extinction of the radiation. Here we have to distinguish Mie- and Rayleigh-scattering. The first describes scattering of light by particles which have a similar or a larger size compared to the wavelength of the incident light. On the contrary Rayleigh-scattering describes scattering by particles that have a smaller size compared to the wavelength of the incident light. Additionally, one has to take into account that all these effects are not constant along the light path through the atmosphere.

Taking all these effects into account and expanding Lamberts-Beer's law leads to:

$$I(\lambda, L) = I_0(\lambda) \cdot \exp\left[-\int_0^L \sum \left(\sigma_i(\lambda) \cdot c_i(s)\right) + \epsilon_R(\lambda, s) + \epsilon_M(\lambda, s) ds\right] \cdot A(\lambda) \qquad (2.3)$$

Here c_i and σ_i denote the concentrations and the absorption cross-sections of the different gases. ϵ_R and ϵ_M are the extinction coefficients for Rayleigh- and Mie-scattering, respectively. Lastly, the factor $A(\lambda)$ is an efficiency factor which accounts for the fact that scattered light is measured (Richter and Wagner, 2011) and is only needed for scattered light applications of the DOAS principle (see section 2.1.3). This factor depends particularly on the scattering

---

[2]The information in this section is taken from Platt and Stutz (2008).

in the atmosphere and the presence of clouds. In principle, all these effects have to be characterised in order to determine the concentration of a specific trace gas.

To circumvent these issues one can use the DOAS method. Here, the fact that aerosol extinction processes as well as many trace gas absorptions show broad or even smooth spectral characteristics is used. Furthermore, some trace gases show narrowband absorption structures. Therefore, the fundamental idea of DOAS is to separate broad- and narrowband structures in an absorption spectrum (for illustration see figure 2.2). In this way, the narrow trace gas absorption is isolated and then Lambert-Beer's law can be applied to the narrowband absorptions.
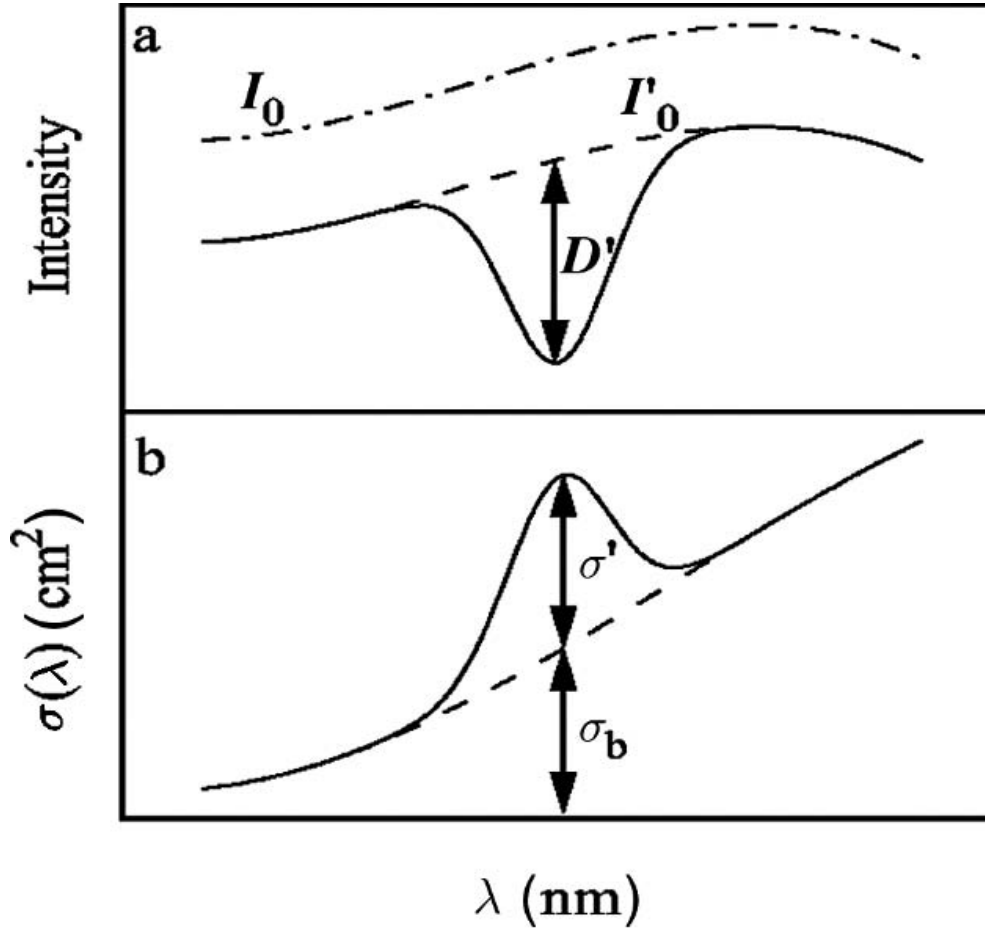

Figure 2.2.: Basic idea of DOAS: The intensity I_0 and the cross-section σ are separated into a narrow and a broad band part, taken from Platt and Stutz (2008).

As depicted in figure 2.2 the absorption cross-section is split up into a broadband part σ_b and a narrowband part σ'. Thus for a specific trace gas we can write:

$$\sigma_i = \sigma_{i,b} + \sigma_i' \tag{2.4}$$

$\sigma_{i,b}$ varies slowly with the wavelength λ, whereas σ_i' exhibits rapid variations with λ, for example caused by an absorption band (compare figure 2.2). Using this separation in equation 2.3 we get:

$$I(\lambda, L) = I_0'(\lambda) \cdot \exp\left[-\int_0^L \sum \left(\sigma_i'(\lambda) \cdot c_i(s)\right) ds\right], \qquad (2.5)$$

where

$$I_0'(\lambda) = I_0(\lambda) \cdot \exp\left[-\int_0^L \sum \left(\sigma_{i,b}(\lambda) \cdot c_i(s)\right) + \epsilon_R(\lambda, s) + \epsilon_M(\lambda, s) ds\right] \cdot A(\lambda). \qquad (2.6)$$

The quantity $I_0'(\lambda)$ summarises all broadband effects and is approximated by a polynomial fit in most practical applications. Similarly to classical absorption spectroscopy, we can define a differential optical density as follows:

$$\tau' = \ln\left(\frac{I_0'(\lambda)}{I(\lambda, L)}\right) = \int_0^L \sum \left(\sigma_i'(\lambda) \cdot c_i(s)\right) ds \qquad (2.7)$$

Using differential quantities in equation 2.2 allows to calculate so-called slant column densities (SCDs) which measure the integrated trace gas concentration along the effective light path s. The SCD is defined as:

$$SCD = \int_0^L c(s) ds \qquad (2.8)$$

With the help of this quantity equation 2.7 can be written as:

$$\tau' = \ln\left(\frac{I_0'(\lambda)}{I(\lambda, L)}\right) = \sum \left(\sigma_i'(\lambda) \cdot SCD_i\right) \qquad (2.9)$$

One major advantage of this approach is the fact that we can measure extremely weak absorptions with optical densities of around $\tau' = 10^{-4}$.

2.1.3. Airmass Factor[3]

There are two basic applications of the DOAS principle for atmospheric measurements. The first one is active DOAS measurements which use artificial light sources. Here the spectral properties of the light source and the light path are known. However, very often the absorption of the trace gas of interest is very weak which requires rather long light paths in order to increase the sensitivity to those gases. In some cases, e.g. for mobile applications, very compact measurement setups are necessary.

The second application is passive DOAS systems that mostly use the sun as a light source and investigate scattered sunlight which provides long light paths. For scattered light DOAS measurements the instrument is not looking in the direction of the sun and the light path is not equal to the direct path between sun and detector. On the contrary photons can reach the detector on a variety of different light paths and the absorptions of the trace gases depend strongly on the light path the photons take through the atmosphere. The quantity derived from DOAS measurements using scattered sunlight are SCDs which were already introduced in the previous section.

---

[3]The information in this section is taken from Hönninger et al. (2004).

As explained above, in addition to the dependence on the trace gas concentration, the SCD depends also on the light path and therefore on the measurement geometry. In order to obtain a quantity that is independent of the geometry, the SCDs are usually converted to so-called vertical column densities (VCDs). VCDs describe the trace gas concentration $c(z)$ integrated along the vertical light path through the atmosphere:

$$VCD = \int_0^\infty c(z) dz \qquad (2.10)$$

The ratio between the SCDs and the VCDs is called airmass factor (AMF) and is used to convert the SCDs into VCDs:

$$AMF = \frac{SCD}{VCD} \qquad (2.11)$$

In practice the AMFs have to be calculated by radiative transport simulations. However, for absorbers which are located close to the surface (e.g. for trace gases in the boundary layer) the AMF can be calculated using the so-called geometric approximation. This approximation is only valid for ground based measurements and we then deal with the tropospheric airmass factor AMF_{trop} and yield the following equation:

$$AMF_{trop} = \frac{1}{\sin \alpha} \qquad (2.12)$$

Here α denotes the elevation angle of the telescope used with MAX-DOAS measurements which will be introduced in the next section.

2.2. MAX-DOAS

This section introduces the principle and the geometry of MAX-DOAS measurements (section 2.2.1). The second part then explains basic quantities that are typically retrieved from MAX-DOAS observations (section 2.2.2).

2.2.1. Measurement Geometry

In contrast to zenith DOAS measurements, MAX (Multi-AXis)-DOAS measurements make use of scattered sunlight received under different elevation angles α (Hönninger et al., 2004). The measurement geometry and the respective angles are shown in figure 2.3.

Since the scattering usually takes place in the troposphere, the sensitivity to stratospheric absorbers is nearly independent on the elevation angle, whereas the sensitivity to tropospheric trace gases is strongly depending on the elevation angle (Wagner et al., 2010). This is because the light path through the tropospheric trace gas layer is enhanced, as the elevation angle becomes lower (see figure 2.3). Compared to zenith direction this leads to a higher absorption. The sensitivity for stratospheric absorbers on the other hand is increasing with increasing solar zenith angle (SZA) ϑ, as the light path through the stratosphere is enhanced in this case. Combining measurements from different elevation angles allows to retrieve information on the tropospheric abundance of trace gases and aerosols (Wagner et al., 2010).

Using this measurement geometry the airmass factor becomes a function of the wavelength λ, the SZA ϑ, the elevation angle α and the relative azimuth angle ϕ. The latter measures the azimuth angle between sun and telescope (Hönninger et al., 2004). Accordingly, we write:

$$AMF(\lambda, \vartheta, \alpha, \phi) = \frac{SCD(\lambda, \vartheta, \alpha, \phi)}{VCD} \tag{2.13}$$

In addition, also the profiles of pressure and temperature, the ground albedo, aerosols and clouds influence the AMF.
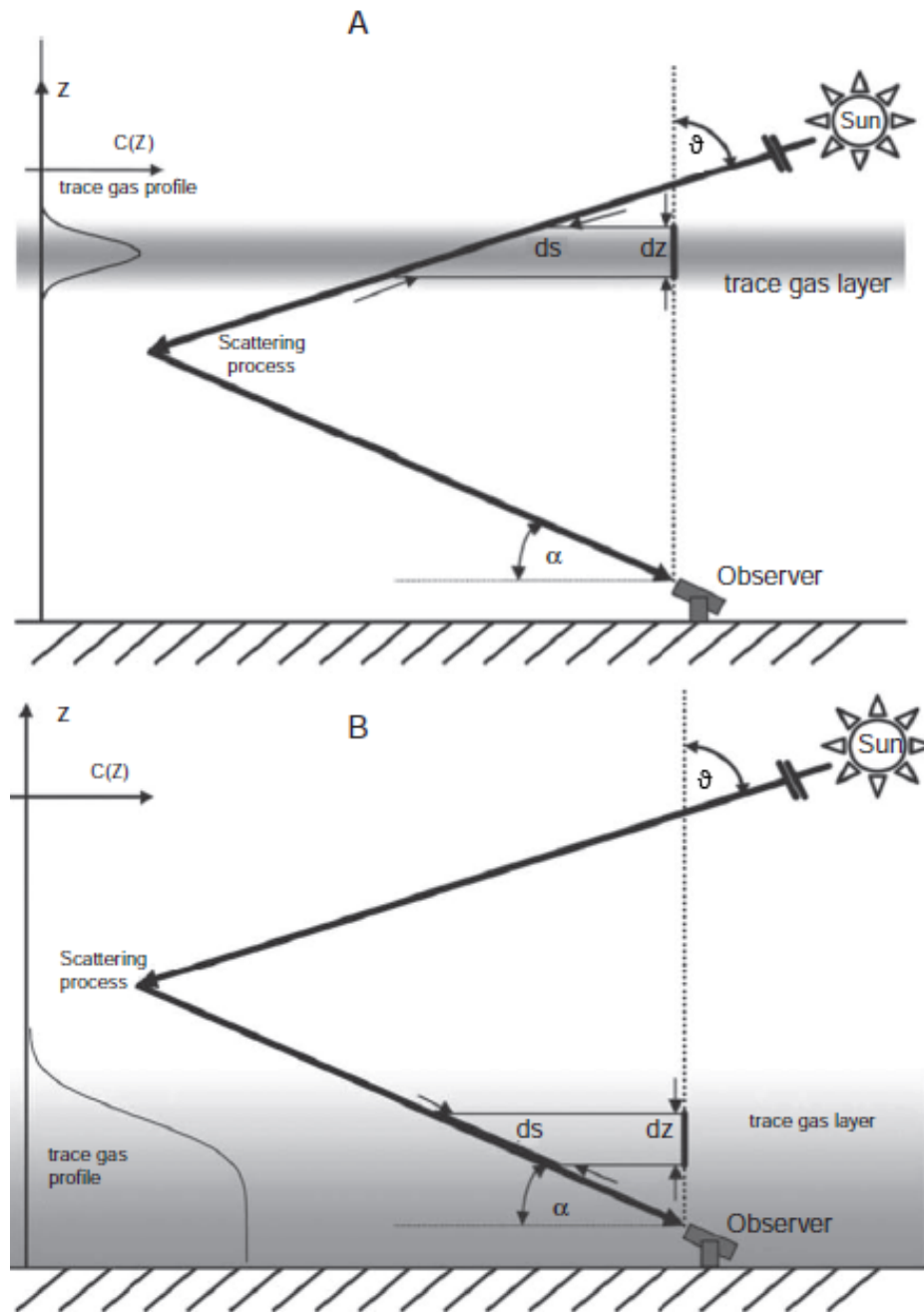
Figure 2.3.: Observation geometry for MAX-DOAS measurements. Panel A: trace gas layer located in the stratosphere. Panel B: trace gas layer located in the troposphere, taken from Platt and Stutz (2008).

2.2.2. Quantities retrieved from MAX-DOAS Measurements[4]

After the spectra were recorded using the previously explained measurement geometry they are analysed using the DOAS principle. Therefore, trace gas absorption cross-sections, a Fraunhofer reference spectrum (see section 2.3) and a polynomial of low order are fitted to the measured spectra. One then obtains the measured SCD_{meas} which was introduced in section 2.1.3. As the light passes the whole atmosphere it can be written as the sum of the tropospheric (SCD_{trop}) and the stratospheric (SCD_{strat}) slant column density:

$$SCD_{meas} = SCD_{trop} + SCD_{strat} \qquad (2.14)$$

Of course also the reference spectrum contains trace gas absorptions and therefore the analysis result only represents the difference between the SCDs of the measured spectrum and the reference spectrum (SCD_{ref}). This quantity is called differential slant column density (DSCD):

$$DSCD_{meas} = SCD_{meas} - SCD_{ref} \qquad (2.15)$$

The influence of the Fraunhofer reference spectrum is investigated in more detail in section 2.3. In order to minimise the effect of the reference spectrum, usually a spectrum with low trace gas absorption is used as reference. A spectrum recorded at noon time with an elevation angle of $90°$ usually fulfils this criterion.

As we have seen in the previous section MAX-DOAS measurements are very sensitive to tropospheric and less sensitive to stratospheric trace gases. Therefore, we can assume that the stratospheric SCD is the same for all elevation angles. This leads to

$$
\begin{aligned}
DSCD_{meas}(\alpha) &= SCD_{trop}(\alpha) + SCD_{strat} - SCD_{trop}(90°) - SCD_{strat} \\
&= SCD_{trop}(\alpha) - SCD_{trop}(90°) = DSCD_{trop}(\alpha),
\end{aligned}
\qquad (2.16)
$$

where the stratospheric contribution cancels out. $DSCD_{trop}(\alpha)$ denotes the tropospheric DSCD measured at an elevation angle of α which is the basic quantity retrieved from MAX-DOAS measurements. If all spectra are analysed using the same reference spectrum this equation also can be written in terms of the measured quantities, namely the DSCDs:

$$DSCD_{trop}(\alpha) = DSCD_{meas}(\alpha) - DSCD_{meas}(90°) \qquad (2.17)$$

2.3. Properties of the Solar Spectrum

As mentioned above passive DOAS measurements mostly use the sun as a light source. The solar spectrum, however, has some special properties which influence the measurements using scattered sun light. Two important properties will be explained in more detail below.

---

[4]The information in this section is taken from Wagner et al. (2010).

2.3.1. Fraunhofer Lines[5]

The light emitted from the sun can be described in good approximation as the emission of a black body with a temperature $T = 5800$ K. This spectrum is overlaid by very pronounced absorption lines, namely the Fraunhofer lines, which result from absorptions within the solar atmosphere. These lines have an absorption around 30 % of the intensity of the respective wavelength at typical DOAS spectral resolution. On the other hand the trace gases in the atmosphere which we want to measure using the DOAS technique exhibit optical densities in the order of 10^{-3} and less. Therefore, the Fraunhofer lines have to be removed during the DOAS analysis in order to evaluate the much weaker absorptions of the atmospheric trace gases. For that reason a so-called Fraunhofer reference spectrum (FRS) is used in the analysis process.

In our case we use a fixed daily reference spectrum which is a spectrum that was recorded around noon time at 90° elevation in order to minimise the trace gas absorption. During the analysis process all spectra are divided by this FRS yielding the DSCDs:

$$\frac{I(\lambda)}{I_{FRS}(\lambda)} = \exp\left[-\sum\left(\sigma_i'(\lambda) \cdot (SCD_i - SCD_{FRS,i})\right) + P\right] \tag{2.18}$$

Rearranging yields:

$$\sum DSCD_i = \sum(SCD_i - SCD_{FRS,i}) = \frac{\ln\left(\frac{I_{FRS}(\lambda)}{I(\lambda)}\right) + P}{\sum \sigma_i'(\lambda)} \tag{2.19}$$

P is a polynomial which describes the difference in the broadband effects of $I(\lambda)$ and $I_{FRS}(\lambda)$. Additionally, this polynomial also accounts for the scattering efficiency factor $A(\lambda)$ (Richter and Wagner, 2011).

2.3.2. Ring Effect[6]

For observations of scattered sunlight the Fraunhofer lines described above show usually weaker features at high SZAs than the same lines at smaller SZAs. This "filling in" effect was first described by Grainger and Ring in 1962 and is therefore called Ring effect. This effect is caused by rotational and vibrational Raman scattering and leads to a change in the optical densities of the Fraunhofer lines of a few percent (Lampel et al., 2015). Since the optical densities of the interesting trace gases are quite weak this effect has to be accounted for to obtain good results. This is usually done by including a so-called Ring spectrum during the DOAS analysis. In our case this Ring spectrum was calculated from the FRS by using the known Raman response functions of molecular oxygen and nitrogen. Additionally, a second Ring spectrum with different broad band spectral dependence is included in the fit process.

---

[5]The information in this section is taken from Hönninger et al. (2004).
[6]The information in this section is taken from Hönninger et al. (2004).

3. Atmospheric Trace Gases

This chapter provides an overview on atmospheric trace gases that are important for this thesis. Figure 3.1 summarises the trace gases which can be detected with the spectrometer used in the TubeMAX-DOAS instrument which will be explained in chapter 4. Rather strong absorption bands can be found for most of the trace gases depicted in figure 3.1. However, not all of them exhibit a strong absorption signal as their atmospheric concentration is small at our measurement site. The trace gases we have to account for in order to analyse the measured spectra for formaldehyde (HCHO) are: O_3, NO_2, HCHO, BrO and the oxygen dimer O_4, as they exhibit quite strong absorption features in the used fitting interval (see section 5.1) given their absorption cross-section and their atmospheric concentration. Bromine oxide (BrO) and Ozone (O_3) will not be discussed in more detail in this chapter as their cross-sections are only fitted because of their strong stratospheric signal at high SZAs. This work deals with measurements of the tropospheric formaldehyde column which is in our case closely related to the nitrogen dioxide (NO_2) column. NO_2 itself belongs to the so-called NO_x (= NO_2 + NO) which summarises nitrogen oxides in the atmosphere. Therefore, basic properties of NO_x and HCHO are explained in the following two sections. The last section of this chapter then introduces the oxygen dimer O_4.

3.1. Nitrogen Oxides (NO_x)

The term NO_x summarises nitrogen oxides located in the atmosphere. During this work this term only summarises two nitrogen oxides, namely nitrogen dioxide (NO_2) and nitrogen monoxide (NO). NO_x is mostly emitted by fossil fuel combustion, biomass burning and from soils. Lightning induced NO_x may play an important role, especially in high altitudes, where it is directly emitted into the free troposphere (Seinfeld and Pandis, 2012). At our measurement site traffic and industry emissions dominate the NO_x signal.

For traffic emissions the directly emitted pollutant is mostly NO, while the direct emissions of NO_2 are low (Finlayson-Pitts and Pitts Jr., 1999). However, these two species establish an equilibrium on a time scale of a few minutes during day time (Seinfeld and Pandis, 2012). For that sunlight with wavelengths below 424 nm is needed and the reactions playing an important role are:

$$NO + O_3 \longrightarrow NO_2 + O_2 \tag{3.1}$$

$$NO_2 + h\nu \longrightarrow NO + O \tag{3.2}$$

$$O + O_2 + M \longrightarrow O_3 + M \tag{3.3}$$
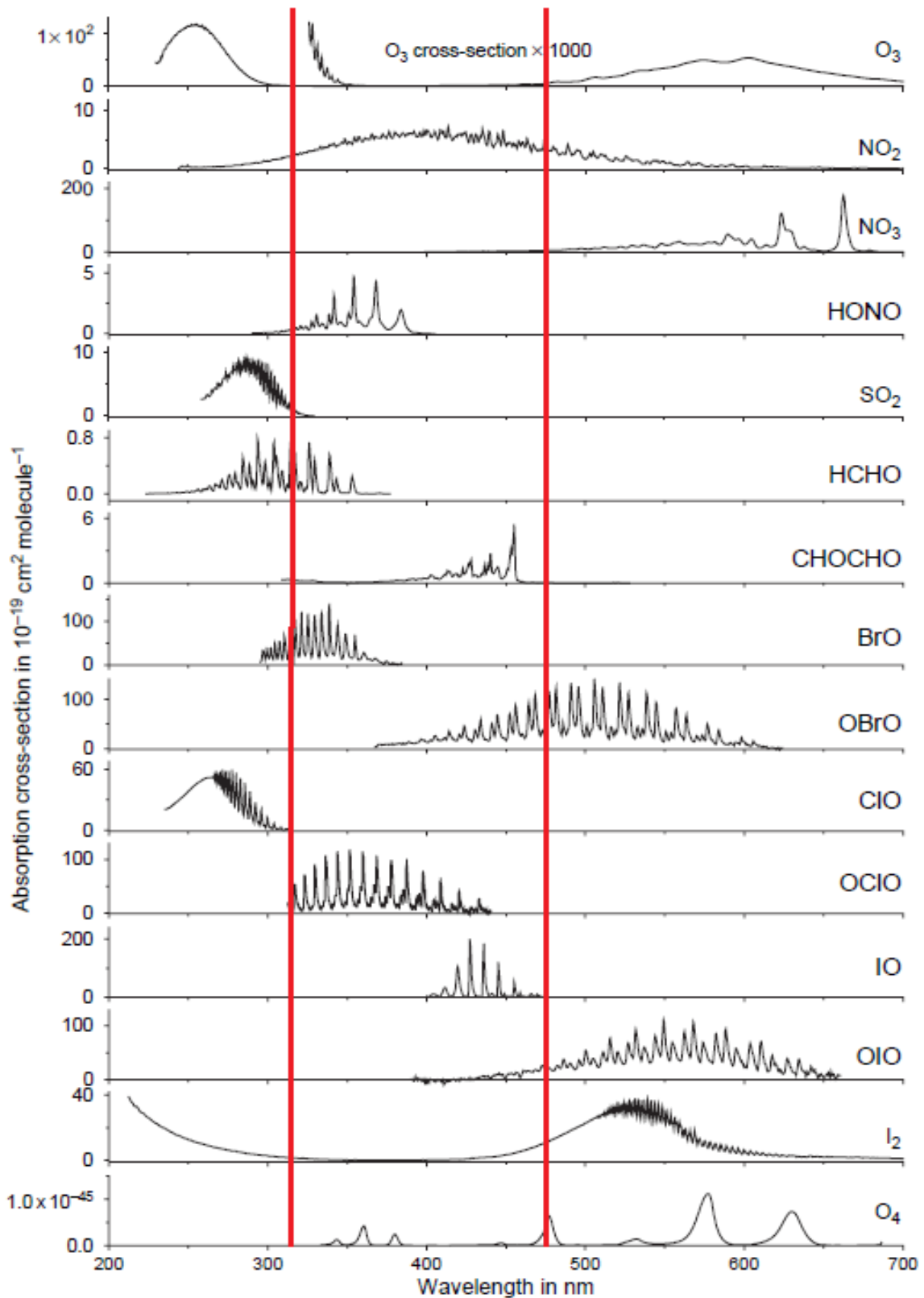
Figure 3.1.: Absorption cross-sections of different atmospheric trace gases. The red lines indicate the spectral range of the used spectrometer, taken from Platt and Stutz (2008).

The first two reactions describe the rapid equilibrium between NO and NO_2, where hv indicates the needed solar radiation. Equation 3.3 describes the only significant ozone source in the troposphere, here M describes a collision partner (mostly N_2 or O_2) which is needed to guarantee the conservation of momentum (Seinfeld and Pandis, 2012).

During night time no solar radiation is present and reaction 3.2 is not possible anymore and most of the NO_x is converted into NO_2. A small fraction of NO_2 is further converted into the nitrate radical NO_3 (Seinfeld and Pandis, 2012).

The major NO_x sink during daytime is oxidation to nitric acid (HNO_3) via

$$NO_2 + OH + M \longrightarrow HNO_3 + M, \tag{3.4}$$

where OH is the hydroxyl radical (Shaiganfar, 2012). HNO_3 is highly water-soluble and is removed from the atmosphere during rain events. At night the major sink of NO_x is a reaction involving NO_3 which reacts with NO_2 itself to form N_2O_5. This reaction then needs liquid water (H_2O) to form again HNO_3 which then removes NO_x from the atmosphere:

$$N_2O_5 + H_2O(s) \longrightarrow 2HNO_3 \tag{3.5}$$
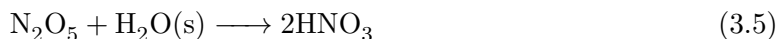
However, the last reaction is quite slow and NO_2 and NO_3 establish an equilibrium during night time and accumulate, especially in urban pollution plumes (Seinfeld and Pandis, 2012).

Besides being highly involved in tropospheric chemistry, NO_x also is harmful for human health. It leads to headache, breathlessness, vertigo and is carcinogenic if the concentration is very high, like e.g. in urban atmospheres. Therefore, controlling and reducing its atmospheric concentration is crucial in order to improve urban air quality.

Coming back to the first three reactions (3.1 to 3.3), it is obvious that these three reactions form a so-called null cycle, as each of the substances is consumed and reproduced again. But if the regeneration of NO_2 (reaction 3.1) is possible over different reaction paths which do not need any ozone, in net one O_3 molecule would be generated. Indeed this happens if hydroxyl radicals and hydrocarbons come into play and this is where also formaldehyde plays an important role (Roedel and Wagner, 2011). The role of HCHO in tropospheric chemistry will be explained in more detail in the next section.

3.2. Formaldehyde (HCHO)

Formaldehyde belongs to the large group of oxygenated volatile organic compounds (OVOCs) which contains a lot of different subgroups, here HCHO belongs to the carbonyls. This group of atmospheric species has very complex primary and secondary sources which are sometimes hardly to distinguish. These substances are directly emitted into the atmosphere from different anthropogenic and natural sources, but they are also products of oxidation pathways of organic compounds in the atmosphere (Koppmann, 2007).

Anthropogenic sources for formaldehyde are car exhausts (especially from diesel cars and trucks), industrial processes (refining, petrochemistry, paint industry...), solvent evaporation and to an uncertain extent also biomass burning. Here direct emissions as well as secondary

production of HCHO might play a role, as incomplete combustion of fossil fuels yields hydro-carbons which then are oxidised to formaldehyde. But also the biosphere plays an important role in emitting OVOCs directly (Koppmann, 2007).

HCHO is one of the most abundant secondary produced OVOCs. Its largest source in the atmosphere is the oxidation of VOCs due to the reaction with OH radicals (Koppmann, 2007). As an example the following equations show the production of formaldehyde from methane (CH_4) oxidation:

$$CH_4 + OH \longrightarrow CH_3 + H_2O \tag{3.6}$$

$$CH_3 + O_2 + M \longrightarrow CH_3O_2 + M \tag{3.7}$$

$$CH_3O_2 + NO \longrightarrow CH_3O + NO_2 \tag{3.8}$$

$$CH_3O + O_2 \longrightarrow HCHO + HO_2 \tag{3.9}$$
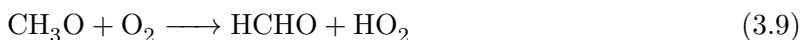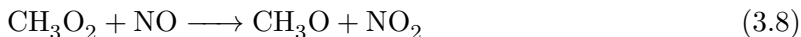
Reactions 3.6 to 3.8 are one possible path which regenerates NO_2 from NO without con-suming an ozone molecule. In principle CH_4 could be replaced by more complex VOCs which leads to a plenty of pathways which can regenerate NO_2 in order to produce O_3. This mech-anism can become very complex, but many of these mechanisms finally yield radicals and HCHO as a stable intermediate product. As CH_3O in reaction 3.8 is a highly reactive radical it reacts quite fast with the atmospheric oxygen and yields an HO_2 radical which also is able to oxidise NO to NO_2 via:

$$NO + HO_2 \longrightarrow NO_2 + OH \tag{3.10}$$

This reaction also shows that the OH and HO_2 radicals are closely related to each other. Additionally, the oxidation of isoprene is one major source of HCHO which leads to a strong signal during summer, as isoprene is mostly emitted by vegetation.

The two major sinks of HCHO are oxidation by the OH radical and photolysis. Also wet deposition is one sink of formaldehyde as it is highly water-soluble. On the one hand the oxidation can be described by the following reactions:

$$HCHO + OH \longrightarrow HCO + H_2O \tag{3.11}$$

$$HCO + O_2 \longrightarrow CO + HO_2 \tag{3.12}$$
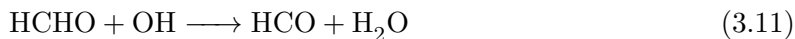
On the other hand photolysis of formaldehyde also produces HO_2 and the reaction pathway depends on the wavelength of the incident photons (hv_1 for $\lambda < 370\,\text{nm}$ and hv_2 for $\lambda < 334\,\text{nm}$):

$$\text{HCHO} + h\nu_1 \longrightarrow \text{CO} + \text{H}_2 \tag{3.13}$$

$$\text{HCHO} + h\nu_2 \longrightarrow \text{HCO} + \text{H} \tag{3.14}$$

$$\text{H} + \text{O}_2 + \text{M} \longrightarrow \text{HO}_2 + \text{M} \tag{3.15}$$
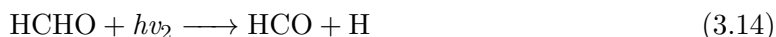
The HCO radical also reacts with oxygen to form HO_2 as indicated by reaction 3.12. As explained above (reaction 3.10) the HO_2 radical then again generates NO_2 from NO without using an ozone molecule.

It can be seen that both the production and destruction of formaldehyde is closely related to tropospheric ozone chemistry via the transformation of NO to NO_2 without consuming an O_3 molecule. This short overview is far from being complete, as there are many much more complex VOCs present in the atmosphere. However, as HCHO is highly involved in all these processes it can be used as an indicator for the overall abundances of all the other involved species. If its concentration is well known, chemical modelling can help to investigate all the other processes and even to identify new (unknown) processes.

The remote HCHO concentration is mainly determined by the CH_4 oxidation and leads to mixing ratios of around 50 ppt to 1 ppb. In urban atmospheres the mixing ratios cover a large range from around 1 ppb up to 40 ppb (Koppmann, 2007).

Formaldehyde has a pronounced annual cycle, as the major sources – biogenic activity as well as methane degradation – are high in summer and rather low in winter. Our measurements took place mainly in winter and spring which suggests that the measured formaldehyde is dominated by anthropogenic emissions. Here both direct emitted and secondary produced formaldehyde might play a role.

3.3. Oxygen Dimer (O_4)

The oxygen dimer O_4 is a collision induced dimer which can in principle be written as $(\text{O}_2)_2$ (Greenblatt et al., 1990). Since its atmospheric concentration varies with the square of the oxygen (O_2) concentration, its concentration profile is well known, mainly dependent on the temperature and pressure profile of the atmosphere and more or less constant in time (Heckel et al., 2005). Therefore, the measured O_4 column densities mainly depend on the length and the altitude distribution of the light path through the atmosphere (see Lambert-Beer's law 2.1). This allows to infer changes in the radiative transfer in the atmosphere, especially in the length of the light path. In addition, also instrumental problems can be identified. We will use this fact in section 6.2 in order to filter our data.

Since also aerosols influence the light path, measurements of the O_4 absorption at different elevation angles can be used to retrieve aerosol profiles.

Furthermore, the absorption cross-section of the oxygen dimer is still not completely well characterised and additional absorption bands are supposed besides the ones which can be found in published absorption cross-sections (Ellis and Kneser, 1933). This effect will be investigated in more detail in section 5.2.2.

4. Setup and Characteristics of the Measuring System

This study deals with mobile MAX-DOAS measurements which were performed with two instruments that were mounted on the roof of a car. One instrument is a self-built MAX-DOAS instrument which consists of different parts which will be explained in more detail in this chapter. First, a general overview on the instrumental setup is given (section 4.1). After that some characteristics of the spectrometer are summarised (section 4.2).

4.1. Instrumental Setup

Most of the measurements presented in this thesis were performed with two MAX-DOAS instruments mounted on the roof of a car. One was a commercial Mini MAX-DOAS instrument built by the Hoffmann Messtechnik GmbH. This instrument was looking forward (in the driving direction) and will not be described in more detail here. The second instrument was a self-built MAX-DOAS instrument which was constructed in collaboration with the electronics workshop of the Max Planck Institute for Chemistry. It was looking backward that means in the opposite driving direction. This instrument is explained and characterised in more detail in this and the following sections.
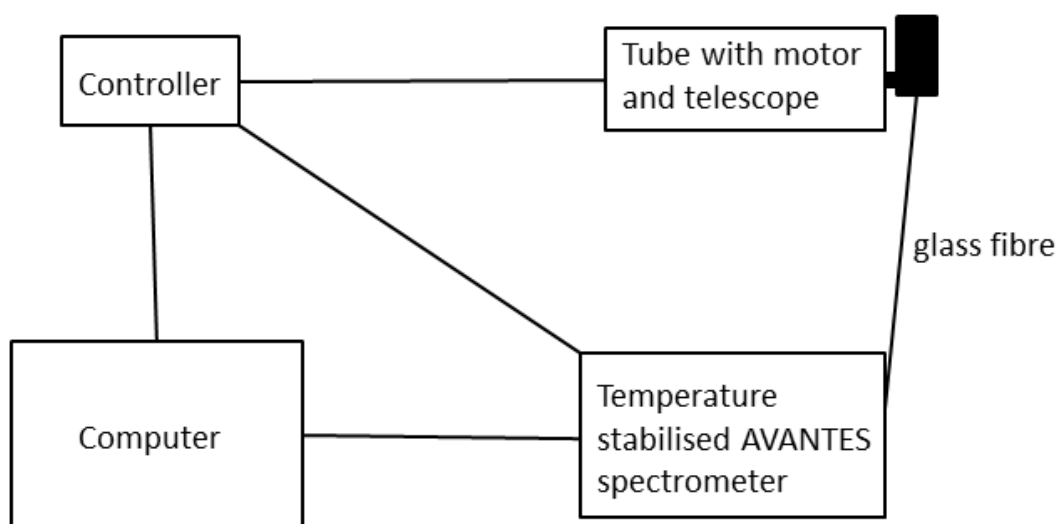
Figure 4.1.: Sketch showing the instrumental setup as it is explained in the text.

The setup is divided in two major parts. One contains the telescope unit and is mounted on the roof of the car. The other is located inside the car and consists of the spectrometer

with a cooling unit, the power supply and a laptop to control the whole instrument. Figure 4.1 shows a schematic sketch of the setup.

The telescope unit contains the telescope which collects the scattered sunlight which is then transmitted via a glass fibre bundle to the spectrometer inside the car. In order to collect light under different elevation angles, the telescope is moved by a motor which is also located on the roof inside a plastic tube. In principle the motor has a precision of $0.01°$, but this is not that important as the measurements are performed on a moving car. The motor is connected to the controlling unit inside the car via electric cables. The on-roof unit is depicted in figure 4.2.

Figure 4.2.: On-roof unit of the TubeMAX-DOAS instrument. The orange tube contains the motor which moves the telescope.

As mentioned above the spectrometer is located inside the car and connected to the telescope via a glass fibre bundle. The spectrometer is the core of the whole setup and is described in more detail below. A cooling unit enables to control the spectrometer temperature. It consists of a Peltier element which is mounted on the spectrometer housing. The Peltier element allows to cool and heat the spectrometer to be stabilised at the required temperature (here a temperature of 10 ℃ was used) with quite low temperature fluctuations of around 0.1 ℃. In order to control the Peltier element and the motor a controlling system developed by the electronics workshop of the Max Planck Institute for Chemistry is used. This system basically sets and reads out the parameters of the different parts and sends them to the laptop which controls the whole setup. The in-car unit is shown in figure 4.3.

Finally, the measurements are performed using the DOASIS software on the laptop. There a measurement script (jscript) is running which sets the parameters and records the spectra of scattered sunlight obtained by the spectrometer.
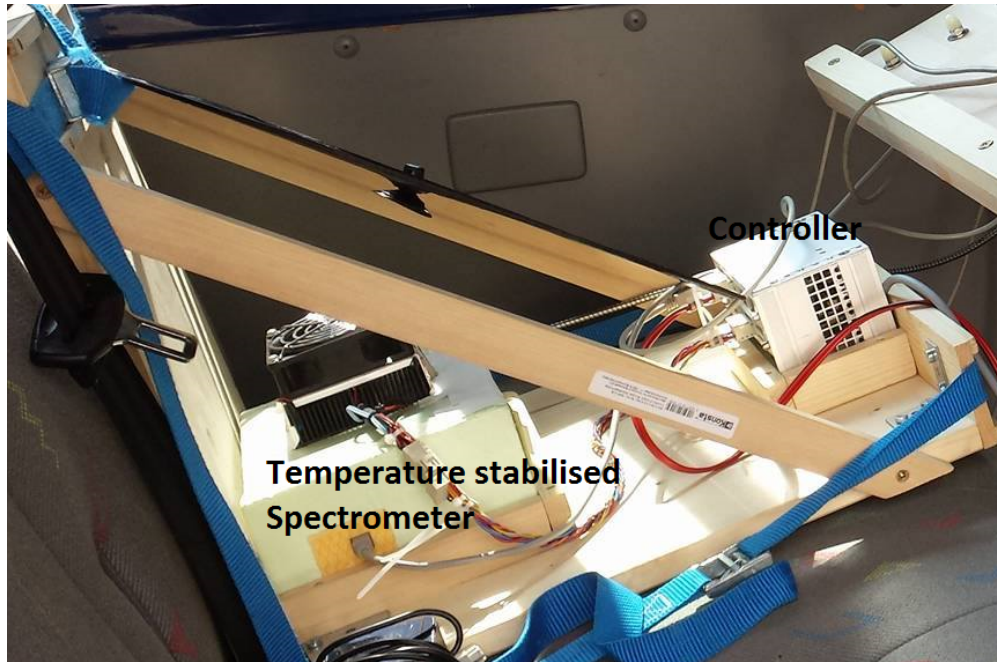
Figure 4.3.: In-car unit of the TubeMAX-DOAS instrument. The wooden frame contains the controller and the temperature stabilised spectrometer.

4.2. Characteristics of the Spectrometer

The core of the whole instrument is the spectrometer which records the spectra of scattered sunlight. It is an AvaSpec-ULS2048x64-USB2 spectrometer with built-in CCD-chip (Charge Coupled Device) which was built by the AVANTES company. Within a metal housing one can find the spectrometer itself and some computer circuit boards which are needed for further processing. The spectrometer is shown in figure 4.4

The spectrometer is built up as a so-called symmetrical Czerny-Turner system. The incident light first passes a slit which is 100 µm wide and around 900 µm high. Then it passes a BG3 filter which filters light of wavelengths higher than around 450 nm[1] and therefore reduces stray light within the spectrometer (Schott AG, 2016). Afterwards a spherical collimation mirror reflects the light on a grating that has a grating constant of 1800 $\frac{1}{mm}$. Here the light is split up into its spectral elements. Finally, a mirror focuses the light on the detector array which registers the photons[2]. The principal wavelength interval is around 315 nm to 474 nm. The given optical setup leads to a spectral resolution in terms of the FWHM (Full Width at Half Maximum) of around 0.65 to 0.69 nm.

The CCD-chip is a Hamamatsu back-thinned detector. It consists of 64 rows and 2048 columns which leads to a total single pixel number of 2048 x 64. A single pixel size of 14 µm x 14 µm yields a detector size of 896 µm in vertical and 28.67 mm in horizontal direction. During the read-out process all counts of a column are added and one obtains 2048 values which lead to a measured spectrum.

---

[1]The filtered wavelength interval is 450 nm to 750 nm. Also wavelengths below 300 nm and above 950 nm are filtered.

[2]Description in this passage taken from MountainPhotonics GmbH (2016).
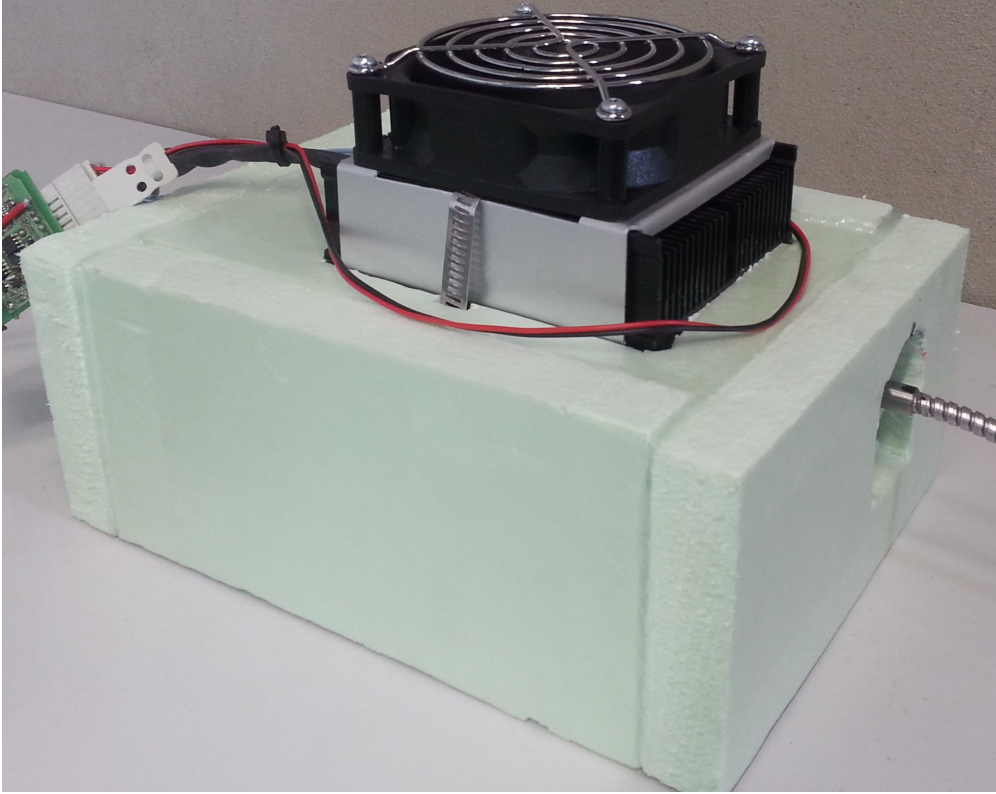
Figure 4.4.: Spectrometer surrounded by insulation material with Peltier cooler mounted on top of it.

A 16-bit analogue-digital converter (A/D converter) transforms the signal induced by the incident light into a digital signal which can be processed by a suitable computer software.

Before the measured spectra can be analysed they have to be corrected for different effects such as the offset, the dark current and the detector non-linearity. These effects are explained in more detail in the following sections. Finally, some information about the detector noise is presented.

4.2.1. Offset

The offset is an artificial signal which is added to the measured values during the read-out process. This is necessary because the A/D converter which was described earlier (see section 4.2) can only deal with positive values. Before a data analysis is possible the offset has to be subtracted from the spectra. Therefore, offset spectra are recorded. This can be done by blocking the light path of the spectrometer and choosing a very low integration time. Here an integration time of 3 ms is chosen and 10000 spectra are added to minimise the influence of statistical fluctuations of the offset. The corrected spectrum is obtained by:

$$I_{corr} = I_{meas} - \frac{N_{meas}}{N_{offset}} \cdot I_{offset} \tag{4.1}$$

Where I_{corr}, I_{meas} and I_{offset} are the corrected, the measured and the offset spectrum, respectively (Shaiganfar, 2012). N_{meas} and N_{offset} are the number of scans of the measured

and the offset spectrum. A typical offset spectrum for the AVANTES spectrometer is shown in figure 4.5.
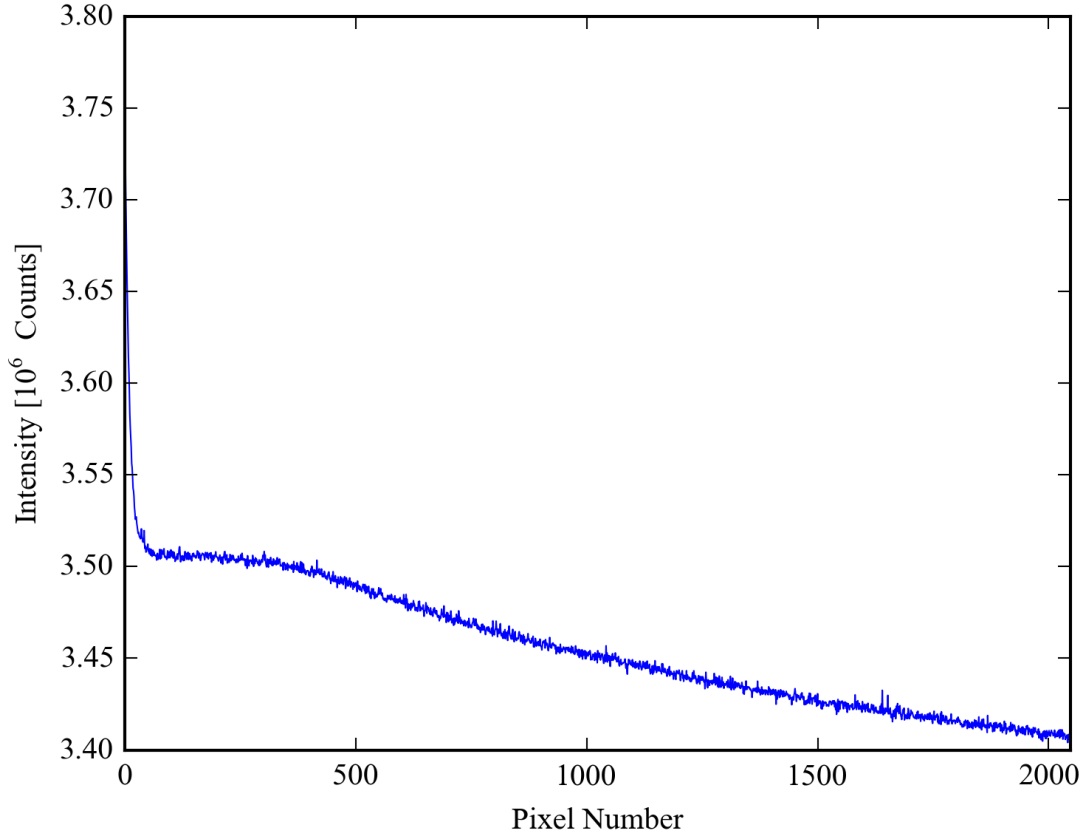
Figure 4.5.: Typical offset spectrum for the used AVANTES spectrometer recorded with 10000 scans at a spectrometer temperature of 10 °C on 25th February 2016.

4.2.2. Dark Current

CCD-chips are made of semiconductors which also produce free electrons due to thermal effects. These electrons are also registered by the CCD without illumination which leads to another signal, namely the dark current (DC), which has to be corrected before the data analysis can be done. Therefore, DC spectra are recorded and subtracted from the measured spectra. DC spectra can be obtained by blocking the light path and choosing a rather long integration time to increase the amount of electrons registered by the CCD. Here an integration time of 20000 ms is chosen, but only one spectrum is taken. Note that the DC also includes the offset and has to be corrected for this. Here the corrected spectrum is obtained by:

$$I_{corr} = I_{meas} - \frac{t_{meas}}{t_{DC}} \cdot I_{DC} \tag{4.2}$$

Here t_{meas} and t_{DC} indicate the integration times of the measured and the DC spectrum (Shaiganfar, 2012). I_{DC} is the DC spectrum taken with a single scan and an integration time

of 20000 ms. A typical DC spectrum for the used spectrometer is shown in figure 4.6. As the DC is caused by thermal effects and its intensity decreases exponentially with decreasing temperature, it can be reduced by cooling the CCD (Platt and Stutz, 2008). Here the whole spectrometer is stabilised at a temperature of 10 ℃.
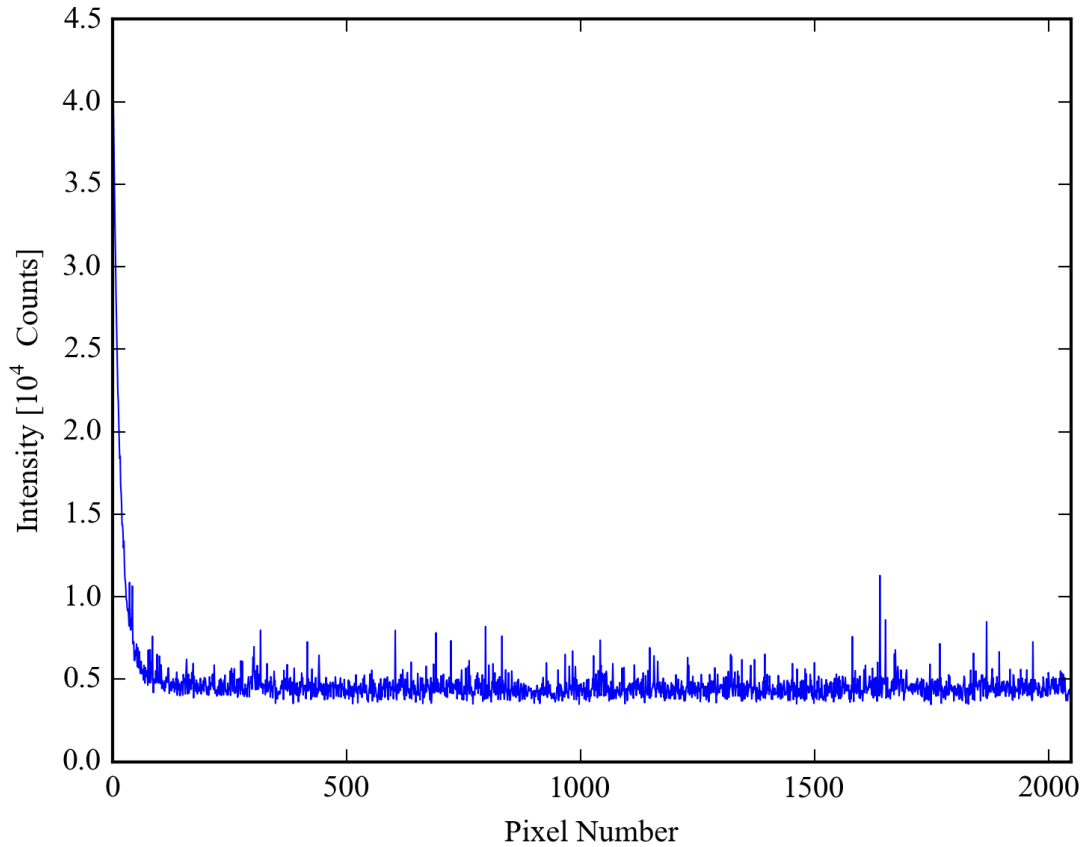
Figure 4.6.: Typical DC spectrum for the used AVANTES spectrometer recorded with an integration time of $20\,000\,\text{ms}$ and at a spectrometer temperature of $10\,°\text{C}$ on 25th February 2016.

4.2.3. Linearity[3]

A further property of the detector electronics is the linearity. To guarantee a high quality of the measurements it is important that the measured signal increases linearly with integration time or intensity. Studies from Horbanski (2015) and a first characterisation of the used detector showed some issues with the linearity. It was found that no perfect linearity was given. This is in principle expected for every instrument if the number of counts registered by the CCD is close to its saturation value. Therefore, normally saturation levels below a certain threshold are chosen for atmospheric measurements. However, the CCD used in this AVANTES spectrometer shows a significant non-linearity even for lower saturation levels. This was also shown by Donner (2014) during the first characterisation of this spectrome-

---

[3]The general information in this section is taken from Horbanski (2015). The procedure of characterising and correcting the non-linearity was done in a collaboration with Johannes Lampel (2015).

ter. Nevertheless, here this effect is investigated in more detail following the studies from Horbanski (2015).

In order to correct for this effect first the non-linearity of the CCD has to be characterised. There are several methods which are summarised in Horbanski (2015). In this work a method by varying the exposure time at a fixed light intensity was applied. In this case spectra of an intensity-stable light source are recorded at different exposure times. Therefore, a temperature stabilised LED which provides a stable spectrum was used. The temperature variations of the used LED are below 0.1 K (Horbanski, 2015).

Now spectra were recorded with a variation of the exposure time in a range from 3 to 50 ms. In order to minimise statistical fluctuations such as photon shot noise, for each spectrum 1000 scans were taken and averaged. In this way three so called "linearity curves" were recorded.

Afterwards the sensitivity in terms of the signal per second was computed by dividing the signal by the respective exposure time t_{exp}. As only the relative change in sensitivity is of interest it is normalised to an arbitrarily chosen reference saturation of 70 %. In order to reduce the influence of measurement noise a polynomial of second order was fitted to the data. The data and the polynomial fit are shown in figure 4.7 which indicates that the effect of non-linearity is around 5 %.
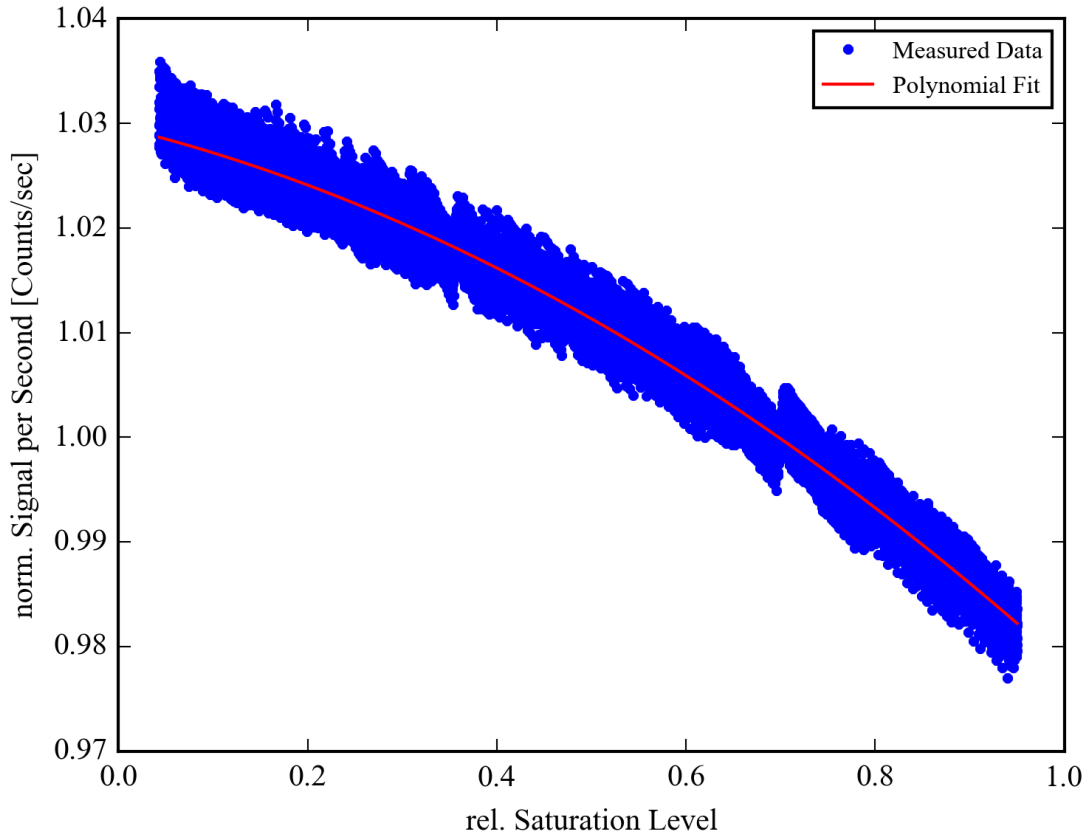
Figure 4.7.: Normalised signal plotted against the relative saturation level (blue dots) and fitted second order polynomial (red curve). The amplitude indicates a non-linearity of around 5 %.

The obtained polynomial describes the non-linearity of the detector and can be directly used to correct for this effect. The described procedure leads to the following polynomial:

$$f_{corr}(S) = -0.0294 \cdot S^2 - 0.0220 \cdot S + 1.0297 \tag{4.3}$$

Here f_{corr} denotes the correction factor and S is the saturation level of the corresponding pixel. The recorded spectra can be corrected for the detector non-linearity by dividing the intensity of each pixel by the respective correction factor f_{corr}. This correction normally is performed after the spectra have been corrected for offset and DC.

As a first test of the method the linearity measurements are corrected in the described way. The result can be seen in figure 4.8. As the values are now spreading around 1, one clearly can see that the effect of non-linearity can be minimised to an acceptable value.
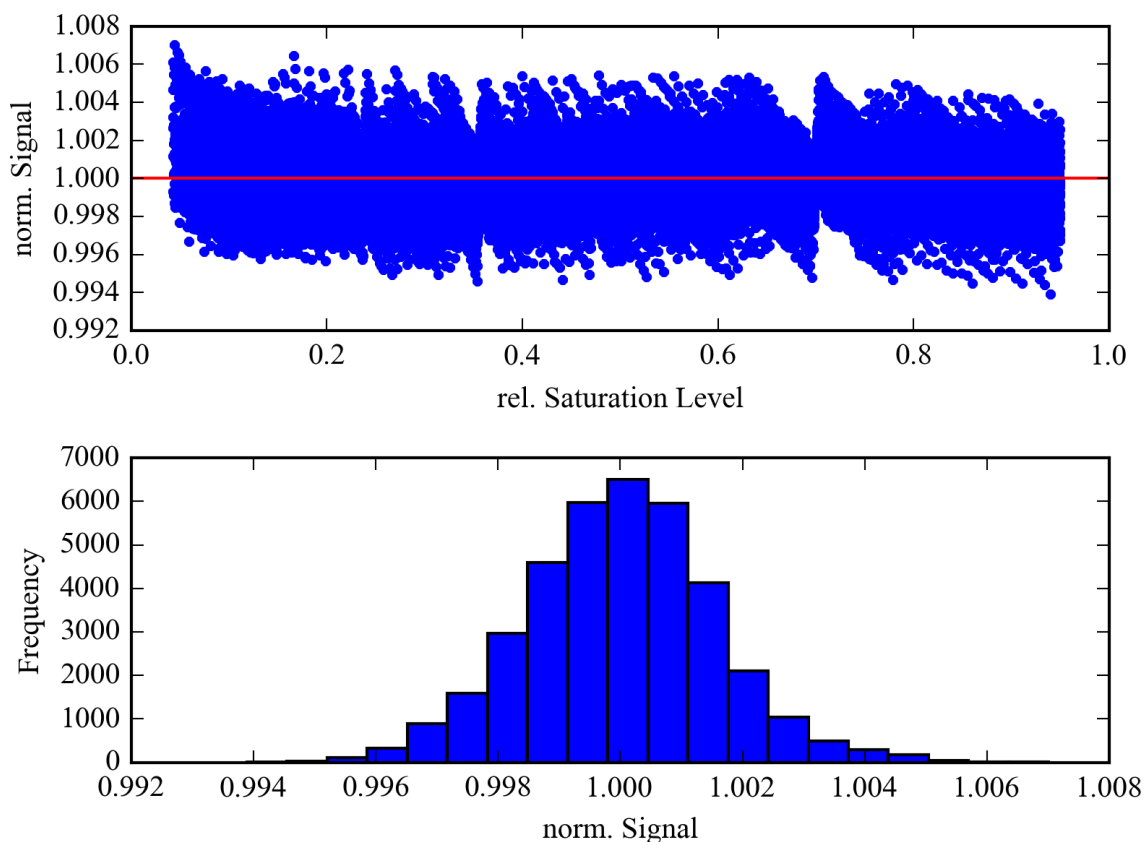
Figure 4.8.: Upper panel: Normalised signal after linearity correction plotted against the relative saturation level (blue dots). The red line indicates the desired value of 1. Lower panel: Frequency distribution of the normalised signal after correction showing a Gaussian shape around 1.

The lower panel of figure 4.8 shows the frequency distribution of the normalised signal after the correction process. As the distribution is more or less Gaussian-shaped and centered at around 1, it can be stated that the fluctuations after the correction are statistical and the effect of non-linearity could be corrected.

4.2.4. Detector Noise

The signal of the detector underlies also statistical fluctuations, namely the detector noise which will be investigated in more detail in this section. The square of the total error that is caused by statistical fluctuations σ_{total} can be written as:

$$\sigma_{total}^2 = \sigma_{offset}^2 + \sigma_{DC}^2 + \sigma_{photons}^2 \tag{4.4}$$

Here σ_{offset}, σ_{DC} and $\sigma_{photons}$ denote the noise caused by the offset, the dark current and the photons, respectively. These three terms are quantified in the following.

According to the datasheet of the used AVANTES spectrometer four photons are needed to generate one count of signal on the 16-bit A/D converter (Avantes BV, 2016). Nevertheless, we want to perform our calculations in units of counts of the detector. Therefore, in order to estimate the photon noise $\sigma_{photons}$, we have to calculate the number of incident photons from the number of counts the detector registers by multiplying the counts with a factor of 4. Then the photon noise in numbers of photons has to be reconverted into counts by dividing by 4:

$$\sigma_{photons} = \frac{\sqrt{4 \cdot N_{counts}}}{4} = \frac{1}{2}\sqrt{N_{counts}}, \tag{4.5}$$

where N_{counts} describes the number of registered counts. As we record spectra of scattered sunlight this value depends on the wavelength of the registered photons and can be calculated based on the measured number of counts.

The offset noise σ_{offset} can be estimated by recording offset spectra with an integration time of 3 ms and a varying number of scans. For each number of scans two spectra were recorded in quick succession and then subtracted. Assuming that the noise is constant over the whole detector array, the standard deviation was calculated and divided by $\sqrt{2}$ because both spectra contain the noise. Now the calculated offset noise which is the calculated standard deviation, can be plotted against the number of scans (see figure 4.9). As we expect a proportionality of the form $\sigma_{offset}(N_{scans}) = \sigma_{offset} \cdot \sqrt{N_{scans}}$, where N_{scans} is the number of scans, a square root function of the same form was fitted to the data points. The fitted curve is also shown in figure 4.9. Following this procedure one yields an offset noise of $\sigma_{offset} = 16.16$ Counts per scan.

At last the DC noise σ_{DC} can be calculated by recording two DC spectra with an integration time of 20 s in quick succession and then following the previously described procedure. Hereby a value of $\sigma_{DC} = 42.09$ Counts is obtained.

From σ_{total} the theoretic optimal value for the root mean square (RMS) can be estimated using

$$RMS_{best} = \frac{\sigma_{total}}{N_{counts}}. \tag{4.6}$$

As explained later in this work the formaldehyde analysis is performed by using a fit interval of 324 nm to 357 nm. For this reason we use the intensity at a wavelength of 340 nm as
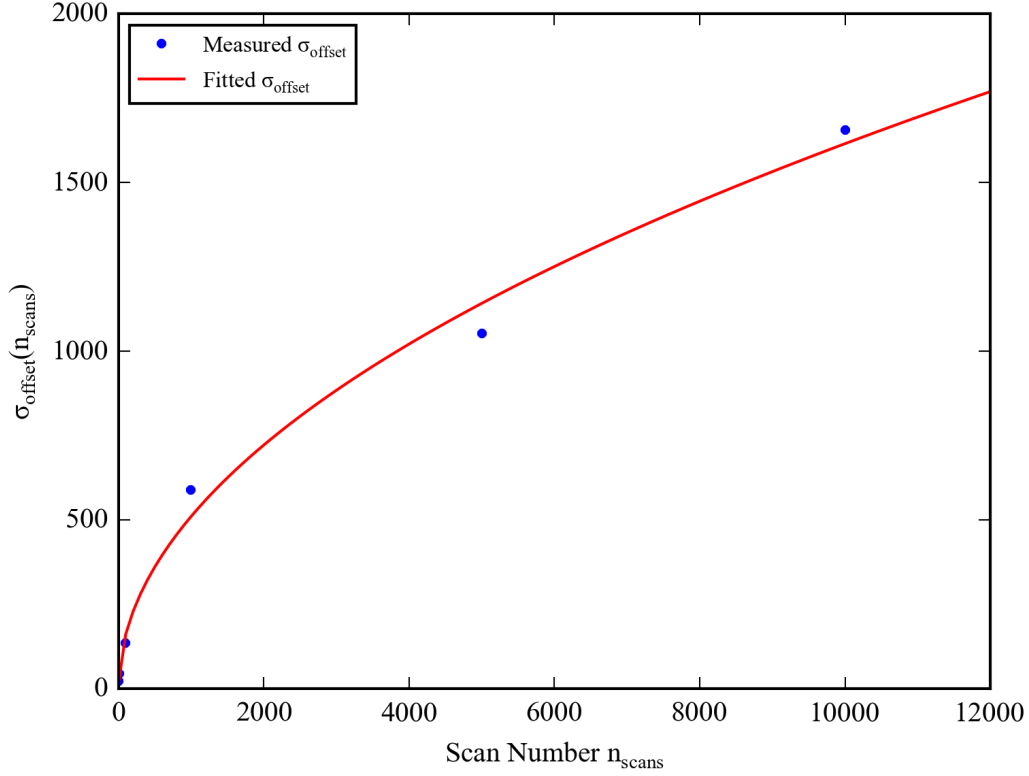
Figure 4.9.: Offset noise σ_{offset} plotted against scan number n_{scans} (blue dots) with fitted square root function (red curve). Following the described procedure a value of 16.16 Counts is obtained.

N_{counts}[4]. Each spectrum contains the offset noise, therefore the value has to be multiplied with $\sqrt{N_{scans}}$. Further, the DC noise has to be scaled with $\sqrt{\frac{t_{meas}}{t_{DC}}}$, where t_{meas} and t_{DC} denote the integration times of the measured spectrum and the DC spectrum, respectively.

Inserting all values from above and typical values for all quantities, namely $t_{meas} = 30\,000\,\text{ms}$, $N_{counts} = 1 \times 10^{7}$ Counts and $N_{scans} = 1000$, yields $RMS_{best} = 1.66 \times 10^{-4}$. This estimation only takes statistical fluctuations into account and excludes systematic errors. Also the number of registered photons and the number of scans depend on the atmospheric conditions. Therefore, this value only can be seen as a rough estimation for the RMS given one specific configuration.

---

[4]In practice N_{counts} depends on the wavelength and varies over the spectral range.

5. Spectral Analysis

This chapter gives an overview on the spectral analysis of the measured spectra. First, the basic analysis settings are introduced (section 5.1), then sensitivity studies are presented (section 5.2). At last a comparison to the second instrument, namely the commercial miniMAX-DOAS instrument, is drawn (section 5.3).

5.1. Analysis Settings

The recorded spectra of scattered sunlight were analysed for formaldehyde using the DOAS method explained above and the WinDOAS software. The analysis settings are summarised in the table below.

Fit-Interval	324-357 nm
HCHO	Meller and Moortgat (2000), 298 K
BrO	Wilmouth et al. (1999), 228 K
NO_2	Vandaele et al. (1998), 294 K, I_0-correction with 10^{17} molec/cm^2
O_3	Bogumil et al. (2003), 243 K, I_0-correction with 10^{20} molec/cm^2
O_3	Bogumil et al. (2003), 223 K, I_0-correction with 10^{20} molec/cm^2 norm. to warm O_3
O_4	Thalman and Volkamer (2013), 293 K
Ring	calculated from daily reference by DOASIS
Second Ring	with different broad band spectral dependence (calculated from first Ring)
Fitted intensity offset	constant
Polynomial	5th order

Table 5.1.: Overview on the used analysis settings and cross-sections.

As Fraunhofer reference spectrum a fixed spectrum which was recorded at 90° elevation and around noon was used for each day. In addition, all spectra were corrected for the detector non-linearity. The influence of the latter is investigated in more detail in section 5.2.

A typical DOAS fit result is depicted in figure 5.1. The single windows show the fit results for the respective absorbers. Each window contains the fit result as a black line, while the measured optical density is represented in red. The headlines of the sub plots indicate the name of the absorber as well as the respective column density in molec/cm^2. Additionally, the first row of figure 5.1 illustrates the spectra (reference and measurement spectrum), the residual, the fitted intensity offset and the polynomial in the same way.

As HCHO is a quite weak absorber a small residual is needed in order to reveal a clear

signal. One clearly can see that this criterion is fulfilled in our case, since the residual shows a value of 3.76×10^{-4} which is also a representative value for other measurement days. In summary clear signals can be found for HCHO, NO_2, O_3 and O_4.
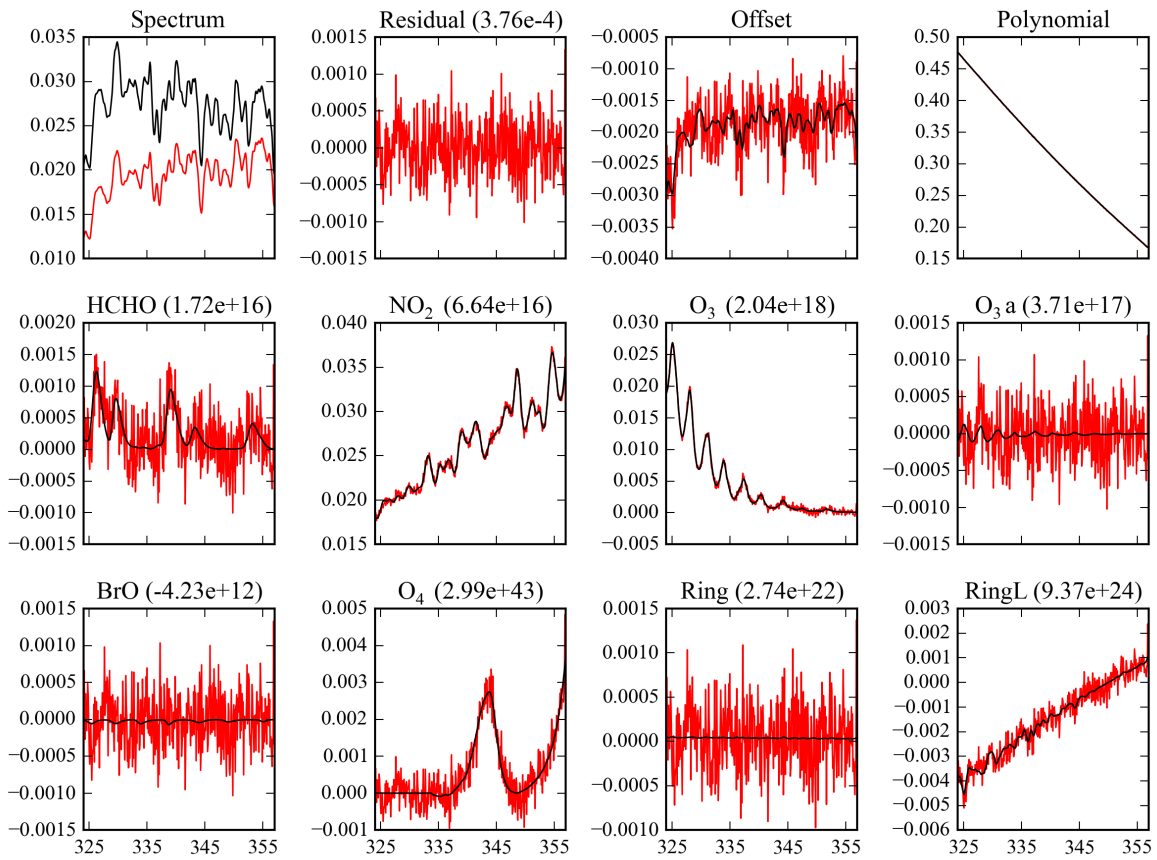
Figure 5.1.: Example for a typical DOAS fit result obtained with the explained analysis settings. The red lines indicate the measured optical densities for the different absorbers, while the fit result is depicted in black. The resulting column densities are indicated by the values which can be found in the titles of the single subplots. The used spectrum was recorded at $15°$ elevation on 5th November 2015 12:10 UTC.

5.2. Sensitivity Studies

Since HCHO is a weak absorber, the fit result might be rather sensitive to the used analysis settings or the cross-sections of the absorbers. Also the effect of non-linearity influences the fit result as it has an influence on the depth of the absorption features. Therefore, sensitivity studies were performed in order to investigate the impact of these effects.

5.2.1. Fit Interval

First, the influence of the chosen fit interval was investigated. In this and the following sections the settings described above act as reference settings and all other settings are compared to these. Also all shown studies were done for the 5th November 2015 (except

section 5.3), as it was a nice and rather good measurement day.

Pinardi et al. (2013) suggest a fit interval from 336.5 to 359 nm, however, figure 5.2 shows that this shorter wavelength interval leads to more noise overlaying the structures in the HCHO-DSCDs (upper panel) caused by a more varying spectral fit result and to higher DSCDs. The shorter wavelength range also leads to slightly higher RMS values during almost the whole day (lower panel), except towards higher SZAs the longer fit interval gets influenced by the strong O_3 absorption at low wavelengths (enhanced light path through the stratosphere, see figure 2.3) and the RMS then yields higher values for the longer fitting interval. For measurements at high SZAs a sequential reference spectrum could help to overcome this issue.
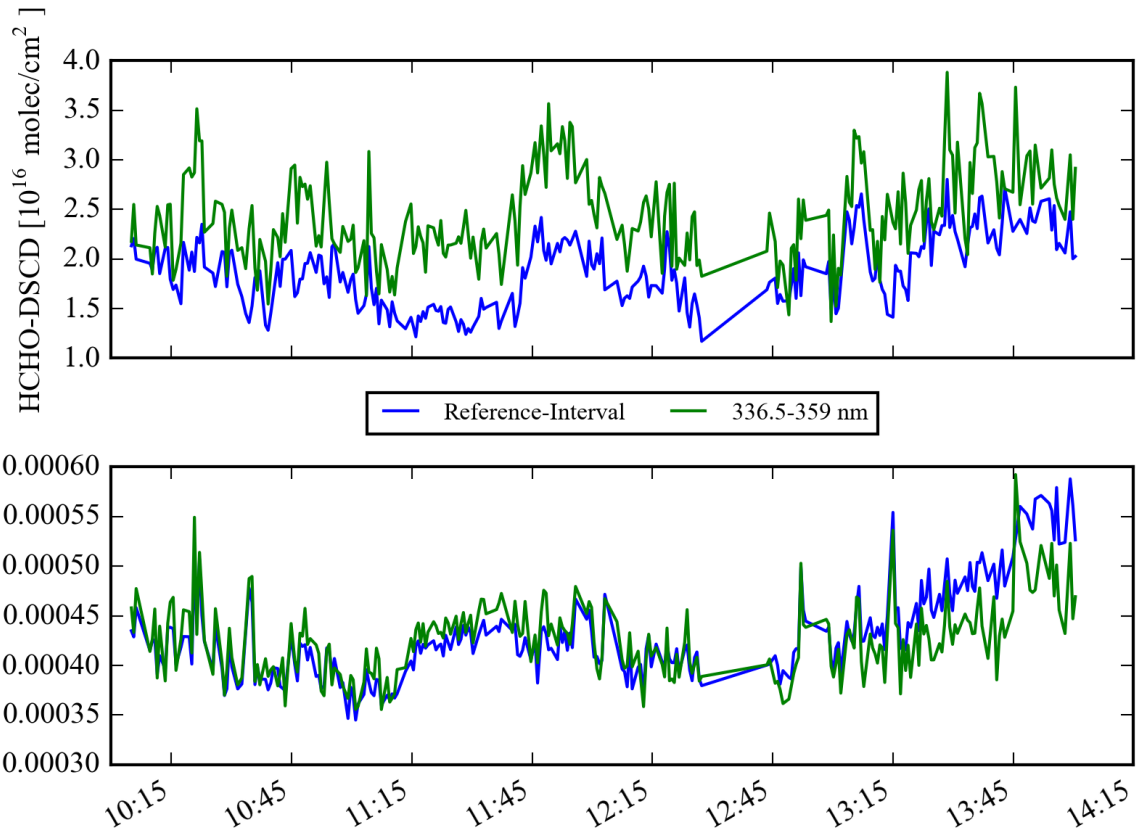
Figure 5.2.: Time series for the HCHO-DSCD at 15° elevation on 5th November 2015 (upper panel). The results for the reference interval are shown in blue, whereas the results for the shorter interval are shown in green. The same colours are valid for the lower panel which depicts the respective RMS values.

In conclusion we choose a longer fit interval, which is described in table 5.1 in order to obtain more stable results, as most of our measurements were not performed at high SZAs. However, the results might also be affected by small changes in the edges of the fit interval. Therefore, four additional analyses with slight modifications in the fitting range were done. First, the lower boundary was decreased and increased to values of 323.5 nm and 324.5 nm, respectively and then two analyses with modified upper boundaries (356.5 nm and 357.5 nm) were performed. The results for the different intervals are depicted in figure 5.3.

The upper panel shows the resulting HCHO-DSCDs, while the lower panel shows the RMS. The different fit intervals yield quite similar results for the DSCDs. The modifications in the upper boundary seem to slightly reduce the DSCDs, while the modified lower boundary seems to slightly enhance them. However, as the obtained DSCDs are nearly the same in all cases and also the RMS values show no large discrepancy, we use the reference fit interval (324 - 357 nm) in the following.
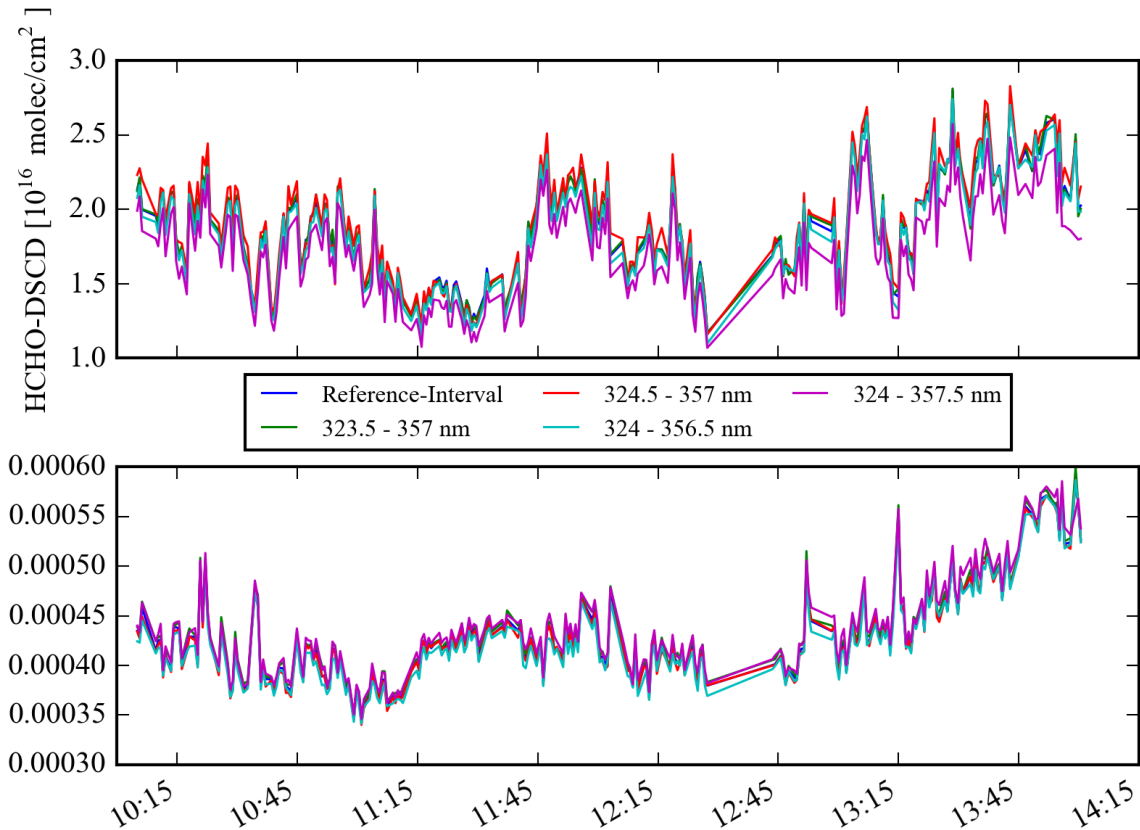
Figure 5.3.: Time series for the HCHO-DSCD at 15° elevation on 5th November 2015 (upper panel) for the different fit intervals (see legend). The same legend is valid for the lower panel which depicts the RMS values for the different intervals.

5.2.2. O$_4$ Absorption

In our standard fitting interval we use the O$_4$ absorption cross-section published by Thalman and Volkamer (2013). Nevertheless, Ellis and Kneser (1933) as well as Salow and Steiner (1936) suggest an additional O$_4$ absorption band at around 328.2 nm, also Lampel (2014) found this absorption in his work. As no cross-section exists which accounts for this absorption band, we simply fit an additional O$_4$ cross-section with one band shifted to 328.2 nm in order to investigate this effect. Figure 5.4 compares the HCHO-DSCDs (upper panel) as well as the RMS (lower panel) for the cases with just one and with two O$_4$ cross-sections.

The additional O$_4$ cross-section leads to a reduction in the obtained HCHO-DSCDs which was also suggested by Lampel (2014), as the supposed O$_4$ absorption band at around 328.2 nm
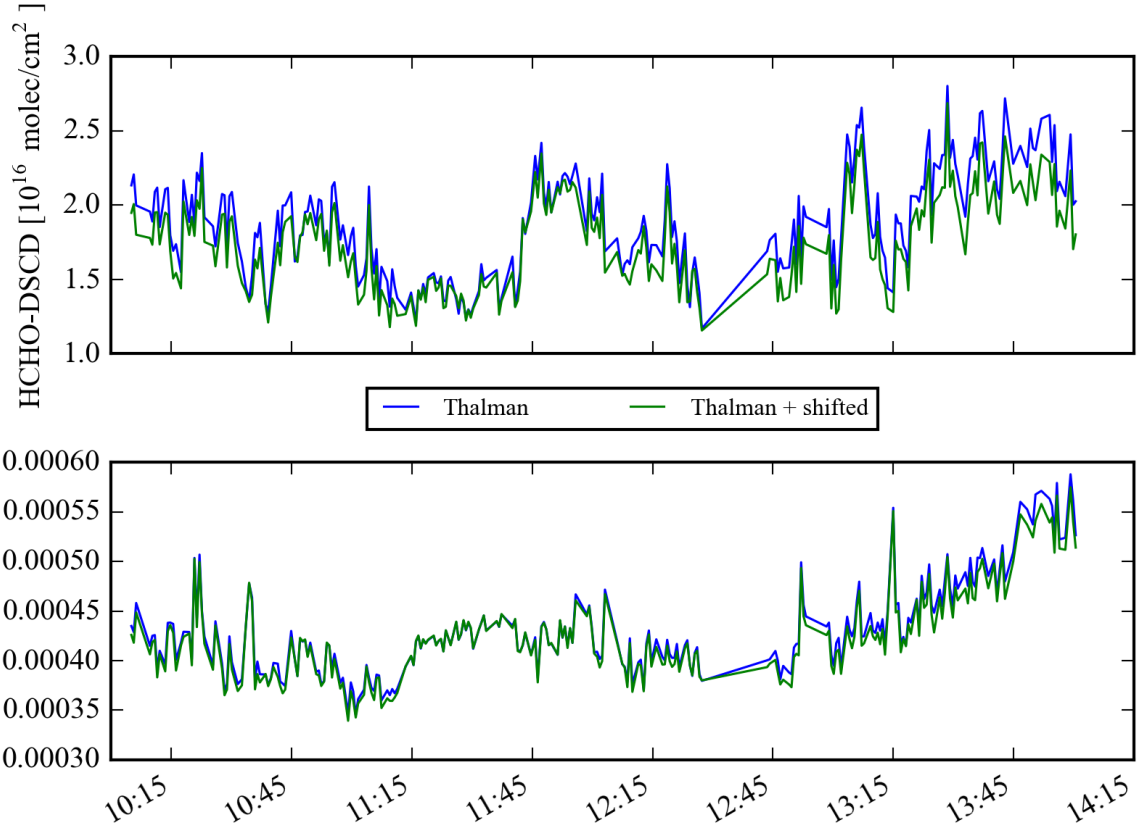
Figure 5.4.: Time series for the HCHO-DSCD at $15°$ elevation on 5th November 2015 (upper panel) for the different settings. The blue line indicates the case with only one O_4 cross-section, while the green line shows the results for the case with an additional O_4 absorption band. The same legend is valid for the lower panel which depicts the RMS values for the different settings.

coincides with the formaldehyde absorption in this region. Also for the RMS a slight reduction can be found.

In our case the absorption strength of the additional absorption band is around 25 % to 33 % of the strength of the absorption band at 343.6 nm. However, Salow and Steiner (1936) found this absorption should be around 15 %. The discrepancy remains unexplained and in the following we will use one O_4 cross-section only (as explained in table 5.1), as there is no existing cross-section that takes account of this absorption band in a proper way.

5.2.3. Effect of the Non-Linearity

As explained in section 4.2.3 the used detector exhibits a non linear response to the incident photons. Thus the depth of the absorptions might be not correctly measured by the instrument. In order to investigate the influence of this effect on the spectral analysis, two different analyses were performed: one with correcting for this effect and one without correcting for this effect. A comparison of the results can be found in figure 5.5. The upper panel again shows the resulting HCHO-DSCDs for both cases, while the lower panel shows the obtained RMS values. One can see that the correction leads to both, lower DSCDs and also lower

(better) RMS values. However, the principal patterns in the DSCDs are quite consistent for both cases.
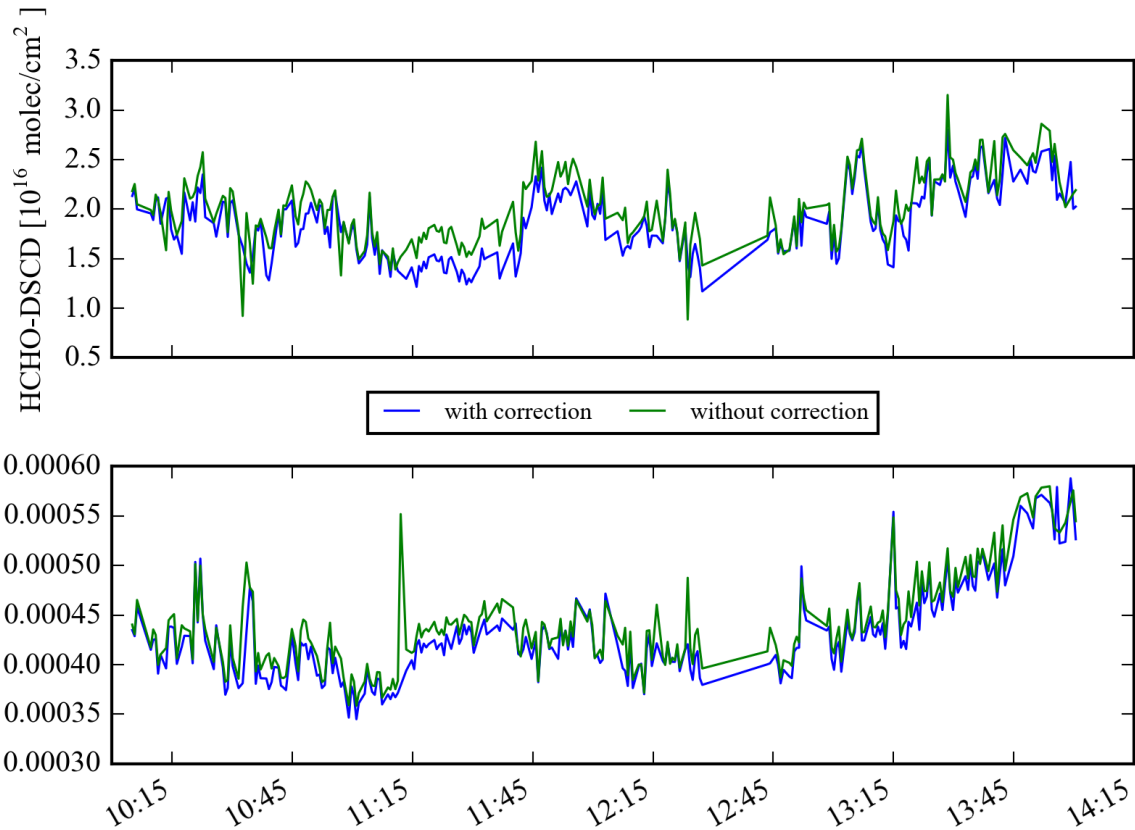
Figure 5.5.: Time series for the HCHO-DSCD at $15°$ elevation on 5th November 2015 (upper panel) for the cases with and without correction for the detector non-linearity. The same legend is valid for the lower panel which depicts the RMS values for the two cases.

Another property to look at is the fitted intensity offset which could compensate for effects caused by the detector non-linearity or spectrometer stray light. Figure 5.6 shows a time series of the fitted intensity offsets for the cases with and without correction. The case with correction (blue line) yields offset values which are closer to zero compared to the case without correction (green line). In the latter case the values spread around -0.005, where the values for the corrected case are around 0.002 which is a clear reduction in the fitted offset value. These results show that the detector non-linearity has a small effect on both the HCHO-DSCDs and the RMS, also the fitted intensity offset is effected. However, most of the effect of the detector non-linearity is accounted for by the fitted intensity offset. Nevertheless, we decided to correct for the effect of detector non-linearity using the procedure explained in section 4.2.3. This gives us more confidence in the results we obtain.
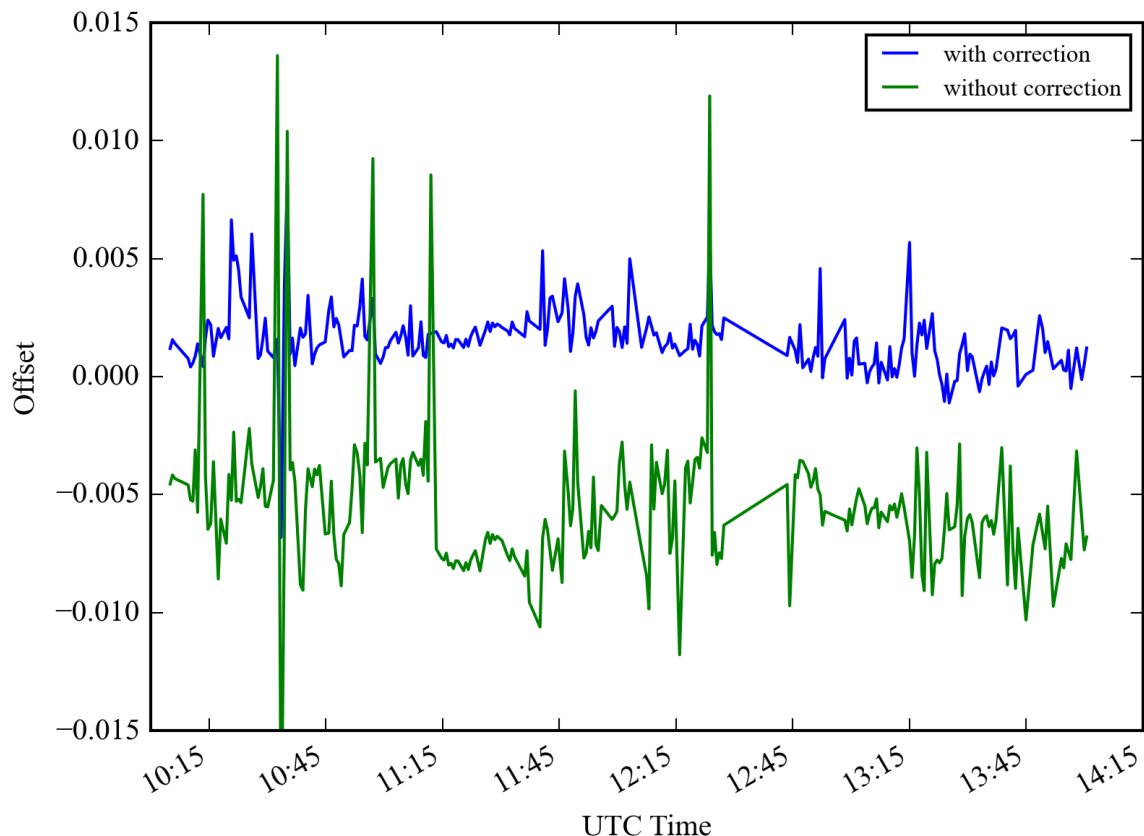
Figure 5.6.: Time series for the fitted intensity offset at 15° elevation on 5th November 2015 for the different settings. The blue line indicates the case with linearity correction, whereas the greens line indicates the case without correction.

5.3. Comparison of the two Instruments

For the measurements which will be discussed in the next chapter, two instruments which were mounted on the roof of a car were used (see section 4.1). They were looking in different directions, but should on average provide similar results for the DSCDs. However, for the measurements in the Rhein-Main area the spectral fit for the miniMAX-DOAS instrument did not work that well. This is most likely due to the worse optical properties of this instrument compared to the TubeMAX-DOAS system. Therefore, the comparison is done for a measurement day (31st August 2015) during the AROMAT2 campaign which took place in Romania in summer 2015. During that campaign significantly higher HCHO absorptions were obtained compared to the measurements in the Rhein-Main area. Also for this reason this study only deals with measurements which were performed with the TubeMAX-DOAS system.

Figure 5.7 shows examples of the spectral fits for both instruments, the left panel depicts the fit example for the TubeMAX-DOAS instrument, while the right panel shows the same for the commercial miniMAX-DOAS instrument. The spectra, which were recorded at similar time, were analysed using quasi simultaneously measured FRS and the same fit settings

which were slightly different from the settings presented above. The obtained HCHO-DSCDs are quite similar for both instruments (note that the instruments are looking in different directions), but the residual yields a huge difference. It is one order of magnitude lower for the AVANTES spectrometer which indicates the much better optical properties of this instrument. Also the noise overlaying the spectral fit (red line in the lower panels) is much smaller for the TubeMAX-DOAS system.
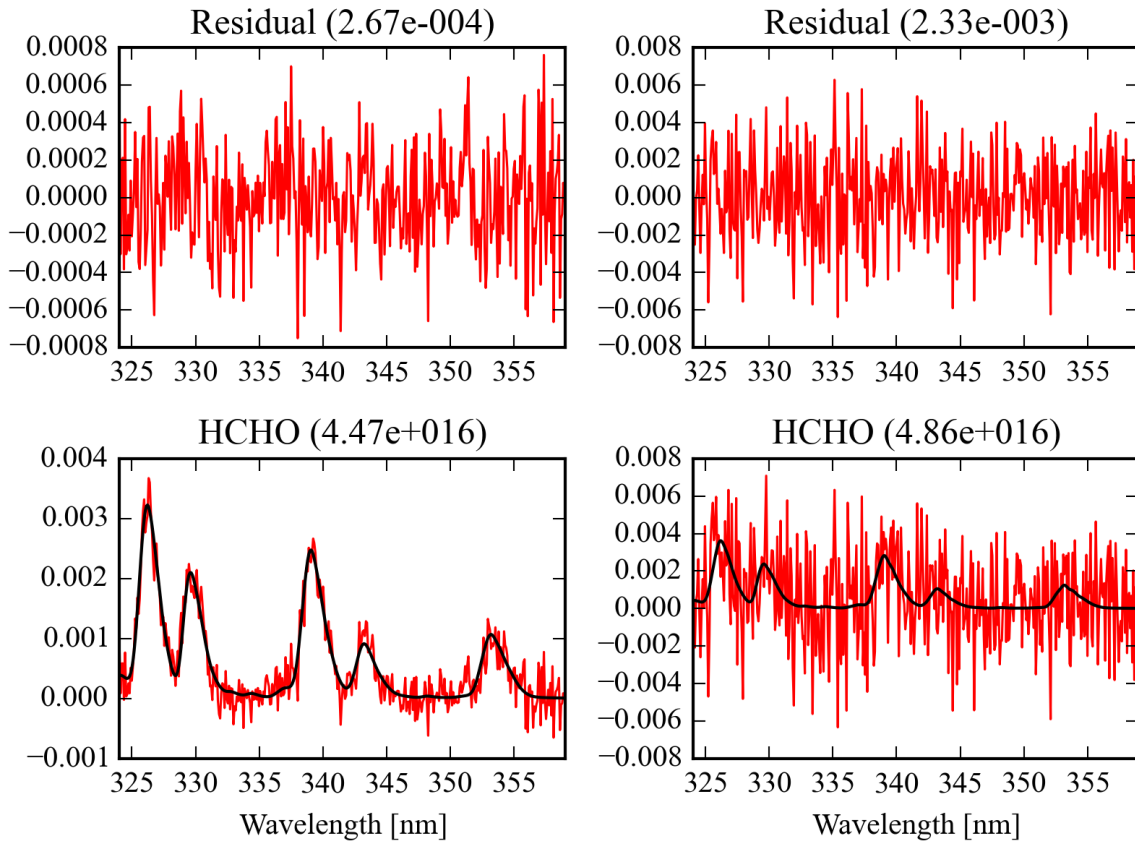
Figure 5.7.: Examples for the HCHO spectral fit for simultaneous measurements with the TubeMAX-DOAS (left panel) and the miniMAX-DOAS instrument (right panel). The red lines indicate the retrieved HCHO absorptions in the measured spectra, whereas the black lines indicate the fitted HCHO cross-section.

A time series for both instruments on this measurement day is shown in figure 5.8. The blue line indicates the results for the TubeMAX-DOAS instrument, whereas the green line indicates the results obtained by the miniMAX-DOAS instrument. On this day two circles around Bucharest were performed, one around noon (note the time is in UTC, local time is +3 hours) and the other in the afternoon. For the first circle the results for both instruments are quite consistent in the principle pattern as well as in the absolute DSCD values. The major difference between the instruments is the fact that for the miniMAX-DOAS instrument the data is more noisy compared to the TubeMAX-DOAS system. Also the difference between the two measuring systems is increasing as the DSCDs are decreasing (e.g. around 10:15 UTC). This effect is even more pronounced in the afternoon where the DSCDs obtained by

the TubeMAX-DOAS instrument are quite low. Here the miniMAX-DOAS instrument is not able to reproduce the low values and yields much higher DSCDs with no clear pattern. This might indicate the much worse optical properties of the miniMAX-DOAS system which could lead to a quite high detection limit for HCHO, which is a rather weak absorber. The time series for the TubeMAX-DOAS instrument still exhibits clear temporal (and therefore spatial) patterns.
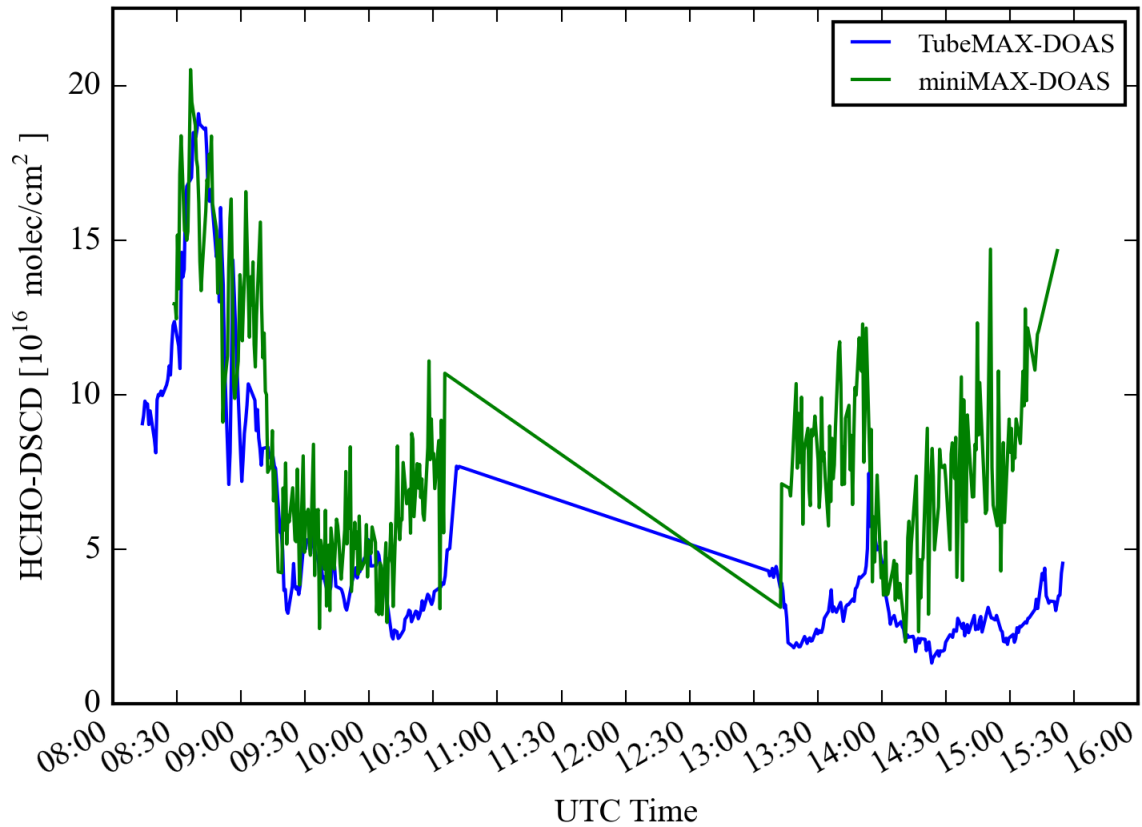
Figure 5.8.: Time series for the HCHO-DSCD at 22° elevation on 31st August 2015 for the two instruments. The blue line indicates DSCDs obtained by the TubeMAX-DOAS instrument, whereas the green line indicates the results from the miniMAX-DOAS system.

Summarising all the findings of this chapter, the self-built TubeMAX-DOAS instrument yields much better results for the HCHO-DSCDs which is most likely due to its better optical and overall properties. Therefore, in the following only results for this measuring system will be investigated.

6. Results

The following part of the work presents and discusses the results of the measurements performed in the Frankfurt/Rhein-Main area. First, some properties of the measurement region are explained (section 6.1). Afterwards the criteria for filtering the data are discussed (section 6.2). Additionally, the wind data is described in section 6.3. Finally, the presentation of the results follows in the remaining part of this section. Most of the results show the spatial distributions of HCHO and NO_2 which are plotted on maps. Here we want to note that all maps throughout this thesis were created using an ArcGIS® web map service by Esri. Therefore the maps are the intellectual property of Esri.

6.1. Measurement Site and Strategy

The measurements presented in this work were performed in the Frankfurt/Rhein-Main area starting from October 2015 and lasting until spring 2016. The Rhein-Main area consists of three major cities, namely Frankfurt/Main, Mainz and Wiesbaden which have 731 095[1], 206 991[2] and 277 729[1] inhabitants, respectively. Additionally, there are several smaller cities which leads to a total population of around 2.5 million people[3] for the whole metropolitan area Frankfurt/Rhein-Main. Furthermore, this region is one of the densest populated areas in Germany. Also many important motorways are crossing the region. Combined with the large population this leads to heavy traffic and therewith to high traffic emissions. Besides this also the largest airport of Germany is located in the south of Frankfurt. In 2015 it had around half a million starts and landings together with around 61 million passengers (FRAPORT AG, 2016). The satellite image below (figure 6.1) shows the measurement region and the red circles indicate the cities of Wiesbaden and Mainz, the Frankfurt airport and the city of Frankfurt (from east to west), respectively. This image also makes clear how dense this region is populated. So the people living in this region are directly exposed to the relatively high pollution caused by the factors summarised above.

The measurements were mainly performed by driving circles around the cities of Frankfurt and Mainz as well as around the airport of Frankfurt using an institute car with the two instruments mounted on the roof of it (see chapter 4). Spectra of scattered sunlight were recorded sequentially at elevation angles of 15°, 22° and 90°. At the beginning of the measurements both instruments were set to sequences consisting of 22° and 90°. Later on the sequences were changed to 15° and 90° to increase the signal for HCHO. All measurement

---

[1]Taken from Hessisches Landesamt für Statistik (2016)
[2]Taken from Statistisches Landesamt Rheinland-Pfalz (2016)
[3]Taken from Eurostat (2016)
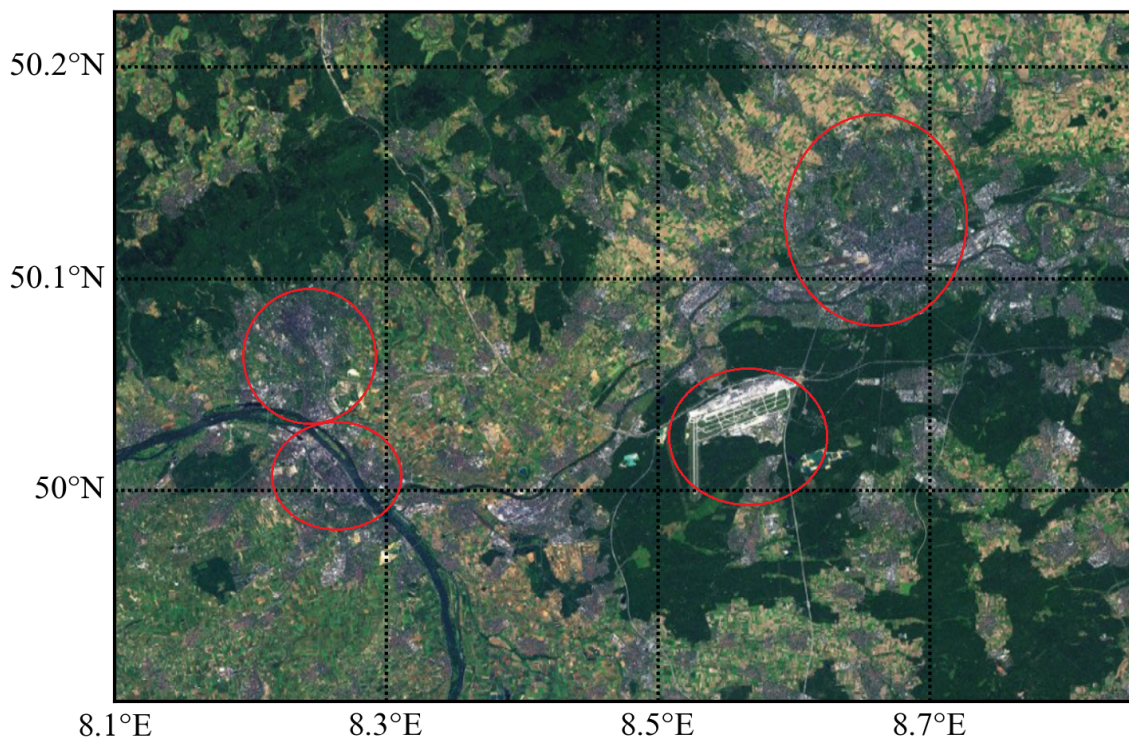
Figure 6.1.: Satellite image showing the measurement region. The red circles mark the cities of Wiesbaden and Mainz, the Frankfurt airport and the city of Frankfurt (from east to west), respectively.

days are summarised in table A.1 in the appendix. This table also shows the used angle series and the respective filter values (see section 6.2) for each measurement day.

Driving circles around the three major measurement sites is quite easy since they are surrounded by well suited motorways. A driving speed of around 80 km/h was chosen on motorways and a lower speed on smaller roads in order to provide a quite good spatial resolution of the data. In the following sections the results will be presented and discussed.

6.2. Data Selection

There are several specialities related to mobile MAX-DOAS measurements. The most important is the fact that MAX-DOAS measurements evaluate solar spectra at quite low elevation angles. For stationary applications very low angles close to the horizon are chosen to get a high sensitivity for tropospheric absorbers, however, for mobile applications this is not possible as one would look at obstacles such as trees and houses. Therefore, higher elevation angles around 20° are typically chosen. Nevertheless, some spectra might still be influenced by obstacles and then obtain strange results, hence the data is filtered before investigating the results. One good measure for the quality of a fit result is the root mean square (RMS). Thus we use the RMS value obtained by the DOAS fit of each spectrum to filter the data.

In the following a RMS threshold of 6×10^{-4} was chosen[4].

For some measurement days in spring we observed some issues which are most likely caused by (almost) direct sunlight reaching the telescope. This leads to a reduction in the light path and therefore to a reduction in the sensitivity. Moreover, for such measurement situations typically also rapid and strong variations of the received intensity are found, which often lead to an over-saturation of a substantial fraction of the scans of individual measurements. As explained in section 3.3 the O_4-DSCD can be used as an indicator for the length of the light path and other instrumental or measurement problems, so for measurements in the direction close to the sun often a rapid drop in the O_4-DSCDs is found. Figure 6.2 shows an example of this effect. The blue line indicates the time series of the obtained HCHO-DSCDs, sudden drops in the DSCDs can be seen around 11:15 and 12:15 UTC. Simultaneous drops can also be seen in the O_4-DSCDs (green line). During these periods unreasonable low values are found for all fitted absorbers (not shown in detail here).
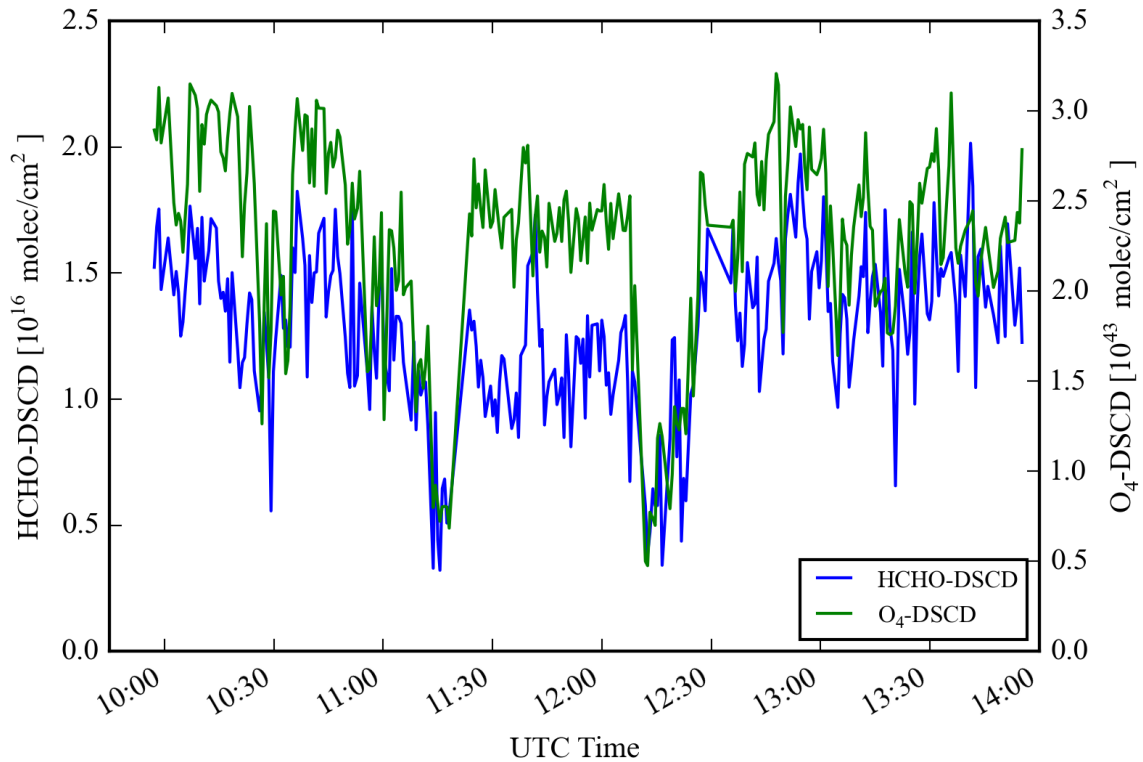
Figure 6.2.: Time series for the HCHO- (blue line) and O_4-DSCD (green line) at 15° elevation on 22nd January 2016. Simultaneous drops can be seen for both absorbers at around 11:15 and 12:15 UTC.

Due to these findings we decided to apply an additional filter to the data, therefore for each day the O_4-DSCDs[5] are evaluated and an individual O_4 filter is defined for the respective day.

---

[4]For 20th December 2015 the RMS threshold is 7×10^{-4} since we would lose a lot of spectra with the stricter filter.

[5]After a comparison of the DSCDs obtained by the HCHO fitting interval and the normally used O_4 fitting interval (350-390 nm), it was decided to simply use the DSCDs obtained by the HCHO interval, as the principle pattern were almost identical.

In that way all spectra which fall below this certain threshold DSCD are filtered out. The respective O_4 threshold for each measurement day is also shown in table A.1 in the appendix.

This additional filter is able to remove the unreasonable DSCDs from the data, however, this leads to unpleasant gaps in the data. Therefore, in the future modifications on the measurement script are planned in order to optimise the saturation level of the individual scans. In addition, also slight modifications on the telescope are planned.

6.3. Wind Data

In the following sections the spatial distribution of HCHO and NO_2 will be presented and discussed. One important factor influencing the spatial distribution of a trace gas species is the prevailing wind. Therefore, the plots in the following section also contain information on the wind speed and the wind direction, both will be indicated by wind barbs. Figure 6.3 acts as legend for the wind barbs. Half increments indicate a wind speed of $0.5\,\mathrm{m\,s^{-1}}$, full ones imply a wind speed of $1\,\mathrm{m\,s^{-1}}$, finally, a flag indicates wind speeds of $5\,\mathrm{m\,s^{-1}}$. In order to depict an arbitrary wind speed one simply has to add the increments, figure 6.3 gives an example for a wind speed of $6.5\,\mathrm{m\,s^{-1}}$ (fourth barb from left).
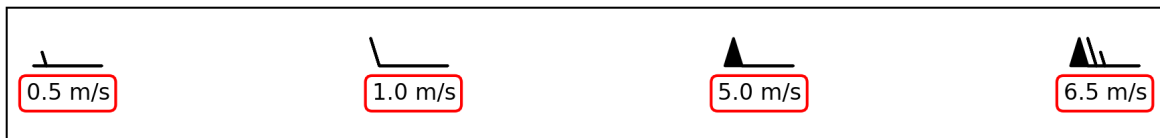
Figure 6.3.: Legend of the wind barbs. The wind barb increments with their respective speed values are shown by the first three barbs (from left to right). The fourth barbs depicts an example for a wind speed of $6.5\,\mathrm{m\,s^{-1}}$. This legend is valid for all plots of this thesis containing wind information.

The wind direction is indicated by the orientation of the wind barbs. Here we use the standard meteorological convention which means that the fictive wind in figure 6.3 is coming from the left and blowing to the right. This kind of wind barbs is valid for all plots of this thesis containing wind information.

In the following wind re-analysis data from the European Centre for Medium-Range Weather Forecasts (ECMWF) is used. We also compared this dataset to in-situ wind measurements from different weather stations (e.g. Mainz-Mombach, Wiesbaden-Süd, etc.) in the measurement region. In most of the cases a good agreement was found between both datasets. Therefore, in the following only the ECMWF data is used since a more comprehensive discussion of different wind datasets would exceed the timespan of this thesis.

The model calculating the ECMWF wind dataset consists of 137 height levels reaching from around $10\,\mathrm{m}$ to $8\,\mathrm{km}$ above ground. In the following we use a mean wind which was calculated by averaging over the lowest 100 meters of the model grid[6]. The dataset provides wind data at four different times for each day (00, 06, 12, 18 UTC), in the following section

---

[6]This equals an average over the lowest five height levels.

mostly the 12 UTC wind data is used as this time is closest to the measurements[7]. In the following maps the wind barbs are simply plotted on their model grid which might lead to strange locations on the respective map.

6.4. Spatial Distribution of Formaldehyde

This chapter provides an overview on the spatial distribution of HCHO for selected cases and for each of the three major measurement sites Mainz, Frankfurt and the Frankfurt airport. The maps were selected in a way that we first present cases which exhibit clear spatial patterns and structures. These cases are more or less representative for all the other measurement days. Nevertheless, since there are also days where the structures and patterns are not so clear, we also show some examples for these less clear cases. An overview on the spatial distribution for all measurements can be found in the appendix (section A.2).

In the following the distribution of HCHO is represented by maps which show the DSCDs (coloured circles) and the respective wind information (black wind barbs). If not indicated differently the 12 UTC wind data was used. Please not that the colour bar indicating the HCHO-DSCDs was chosen constant for each measurement. Here we only show the spatial distribution of the DSCDs since the procedure of calculating VCDs is rather effortful and it was not possible to fully investigate the spatial distribution of the VCDs during this thesis project. Nevertheless, as we will see in section 6.6 HCHO-VCDs were already calculated and a first look on them showed that the spatial distributions are very similar to the distributions of the DSCDs.

In the first three subsections the spatial distribution is presented and explained for each of the three major measurement sites. A short summary and further interpretation of the results follows in the fourth part.

6.4.1. Mainz

First, the results for the HCHO distribution around Mainz are presented. Here we start with the 5th November 2015 which was one of the best measurement days with quite high HCHO-DSCDs and rather clear spatial patterns. Also the weather was very sunny on this day. Figure 6.4 shows the respective HCHO distributions for that day during the different measurement periods.

During the first measurement period (10:00 to 11:10 UTC) the DSCDs are still quite low, but slightly enhanced values around 2.0×10^{16} molec/cm^2 can be found in the outflow (north east of the city) and in the center of the city. Here the observed DSCDs are even slightly higher as in the outflow region. During the second period we tried to drive through the outflow of Mainz which was supposed to be located in the north of Mainz (namely in Wiesbaden) on this day. However, no clear enhancement of the DSCDs can be found in the city of Wiesbaden, the highest values again are located in the city center of Mainz, where

---

[7]For the Frankfurt/Rhein-Main area local time is UTC plus one (winter period) and two hours (summer period), respectively. In 2015 the time change was on 25th October.

(a) 10:00 to 11:10 UTC

(b) 11:10 to 13:00 UTC

(c) 13:00 to 14:00 UTC

(d) 13:00 to 14:00 UTC; 18 UTC wind
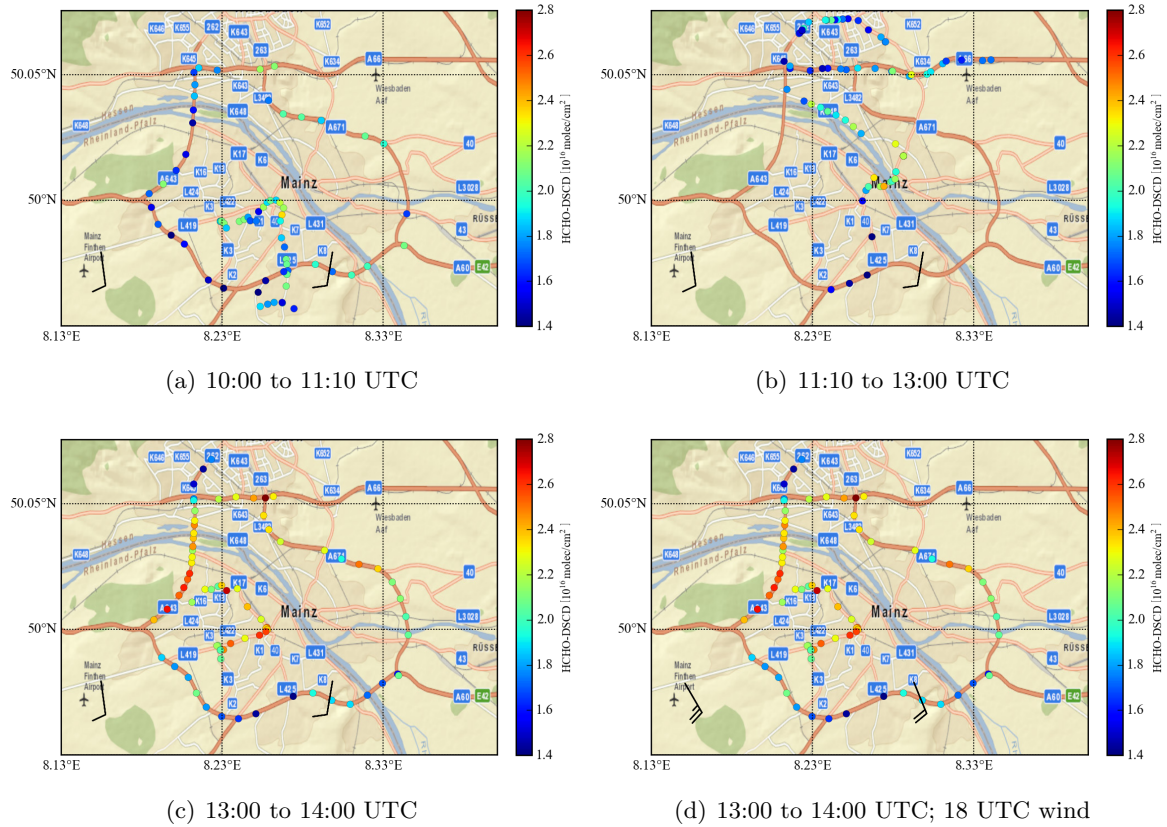
Figure 6.4.: Spatial distribution of the HCHO-DSCDs around Mainz on 5th November 2015 for different time intervals.

the traffic during weekdays is always very dense. Further enhancements can be found close to the Rhein river in north of the industrial area of Mainz-Mombach. This pattern seems to be reasonable as the wind speed was quite low on that day (values around $1\,\text{m}\,\text{s}^{-1}$) and the pollution might be located close to the sources. For the last measurement period on that day the formaldehyde DSCDs reach values up to $2.7 \times 10^{16}\,\text{molec/cm}^2$. High values again can be observed in the center of the city, where the busy roads are located. However, the highest values are now found in the west of the city which does not fit the wind pattern anymore. Therefore, figure 6.4(d) shows the same distribution but now the wind for 18 UTC is plotted. The wind now has an easterly component and the intensity is slightly increased. Taking this wind into consideration, the spatial distribution fits the wind pattern quite well. The increased HCHO-DSCDs might be related to both the photochemistry and the increased traffic on the roads within the city, but also on the motorways.

The second example for the HCHO distribution is given for the 21st January 2016 (see figure 6.5). The wind speed on this day was twice as high as on the 5th November 2015 and a clear outflow region of the city can be identified already in the early measurements. It is located in the west of the city as expected due to the wind pattern. Therefore, measurements in the outflow region were performed and enhanced formaldehyde columns could be observed also a few kilometers west of the city (see figure 6.5(b)). In the city center again increased

DSCDs are found, however, on this day these are only very slightly enhanced. Finally, a full circle around the city was performed on that day, now the outflow seems to be more shifted towards the north, anyhow, the 18 UTC wind shows the same pattern as the 12 UTC wind and the shifted pattern remains unexplained[8]. Also now higher DSCDs can be found within the city center which seems to be a consistent finding throughout all measurements in Mainz. This is most likely related to increased traffic on the roads. All in all the observed DSCDs on this day are significantly lower as the values observed on the 5th November but still reach values around 2.0×10^{16} molec/cm^2.

(a) 10:26 to 11:50 UTC

(b) 11:50 to 12:49 UTC

(c) 12:49 to 13:40 UTC
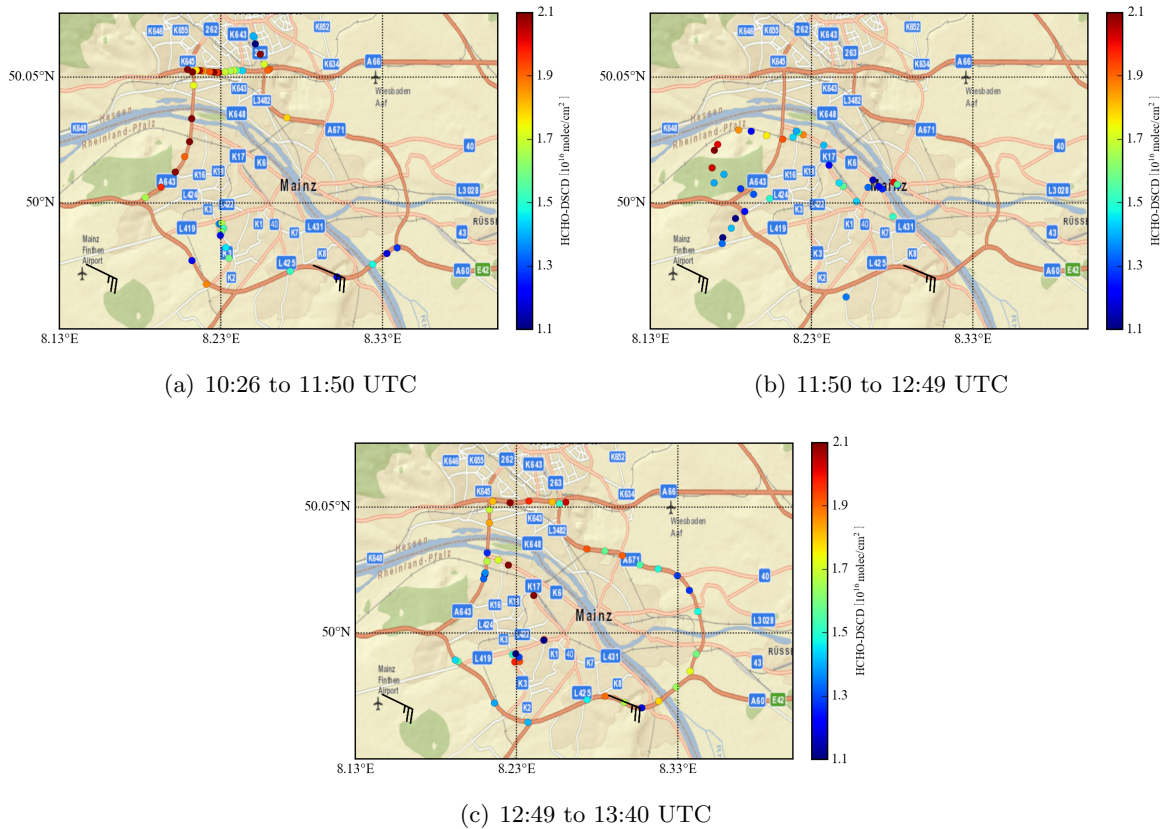
Figure 6.5.: Spatial distribution of the HCHO-DSCDs around Mainz on 21st January 2016 for different time intervals.

As a last example the distribution of HCHO around Mainz for the 25st February 2016 is depicted in figure 6.6.

On that day there was a stable wind coming from north west and the outflow of the city was expected to be a few kilometers south east of the city, since the wind was rather strong with wind speeds around $3.5\,\text{m}\,\text{s}^{-1}$. First, a circle around the city was performed. The highest DSCDs (around 1.6×10^{16} molec/cm^2) are again located within the city center and slightly enhanced values can be found in the south, but also in the north west of the city. The latter might be influenced by the emissions of Wiesbaden. After some measurements in Frankfurt a

---

[8]Note that the wind is averaged over around 100 meters which might influence the resulting direction dramatically.

(a) 09:12 to 10:04 UTC

(b) 11:47 to 12:48 UTC

(c) 12:48 to 13:58 UTC
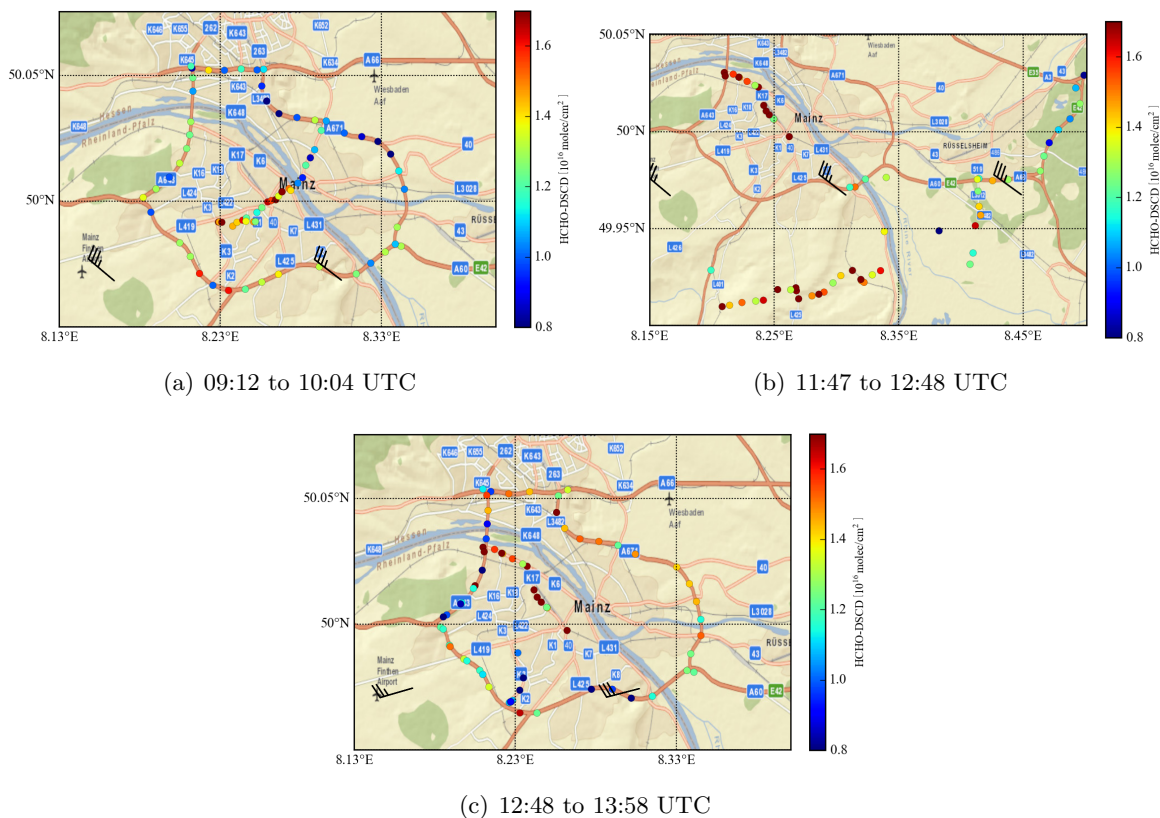
Figure 6.6.: Spatial distribution of the HCHO-DSCDs around Mainz on 25$^{\text{st}}$ February 2016 for different time intervals.

route back to Mainz crossing the supposed outflow region of the city was chosen. Here a clear enhancement of the formaldehyde DSCDs with values around 1.7×10^{16} molec/cm^2 can be observed which were the highest DSCDs we measured on that specific day. Note that there are almost two hours time difference between the first circle around the city and the route through the outflow. So there might be differences in both the chemistry and the emission conditions in Mainz. Finally, another circle around the city was performed, however, the highest values of HCHO-DSCDs can be found within the city and in the east of the city. This pattern does not fit the prevailing wind conditions anymore. Since the in-situ wind data from the Mainz-Mombach station showed a nearly identical wind direction this finding remains unexplained.

Altogether more or less consistent patterns in the spatial distribution of HCHO-DSCDs could be identified for the presented examples. On the other measurement days in Mainz similar patterns were observed (see also section A.2 in the appendix). Some of these days also reveal patterns that are pretty clear as in the example cases, however, there are also days which exhibit very weak or almost no patterns. This could be related to the different chemical and emission conditions that were present on these days. But despite the fact that it is rather complex to separate the sources of formaldehyde (as explained in section 3.2), the distribution around Mainz is most likely heavily influenced by traffic emissions since the NO$_2$ distribution shows similar patterns as we will see in more detail later on.

6.4.2. Frankfurt/Main

Next examples for the spatial formaldehyde distribution around the city of Frankfurt/Main are presented. The first speciality about the measurements around Frankfurt is the fact that we only performed circles around the city and did not cross through the city[9]. Secondly, large parts of the routes are northward which means that the telescope of the TubeMAX-DOAS instrument was often looking towards the sun for large parts of the circle. Therefore, rather much data is filtered out due to the previously explained O_4 filter. At last the city of Frankfurt is largely influenced by the emissions of the airport and the respective trace gas distributions might overlap. Also many motorways which exhibit very dense traffic are located around the city of Frankfurt. Therefore, only few circles around Frankfurt reveal patterns in the HCHO distribution which can be clearly related to distinct sources taking the prevailing wind into account.

First, the formaldehyde distribution for 20th December 2015 is shown in figure 6.7 for the two circles which were performed around Frankfurt on that day.

(a) 10:22 to 11:10 UTC   (b) 11:45 to 12:43 UTC
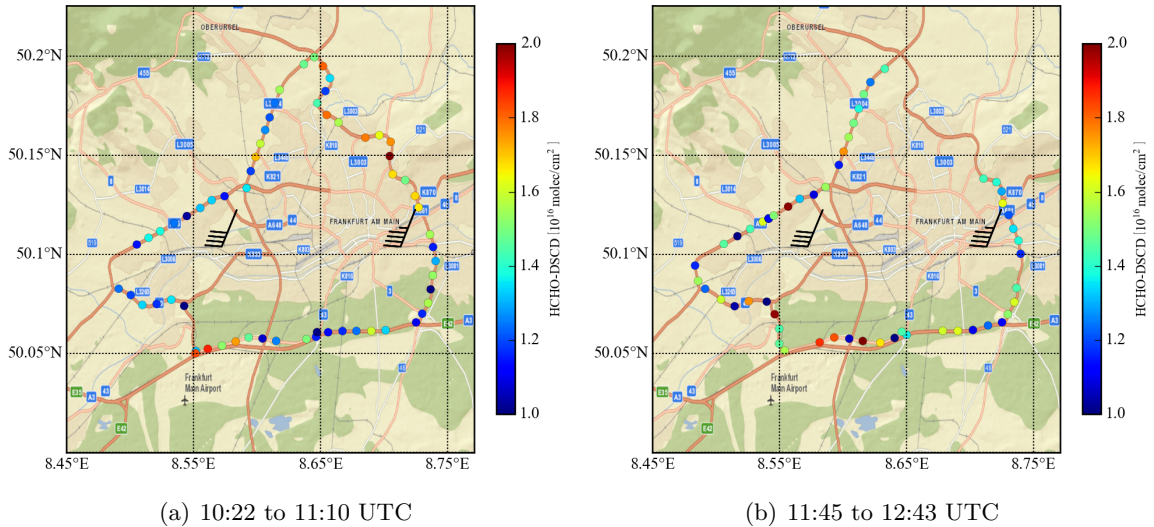
Figure 6.7.: Spatial distribution of the HCHO-DSCDs around Frankfurt/Main on 20th December 2015 for different time intervals.

Sub figure (a) exhibits clear enhanced DSCDs around 1.6×10^{16} to 1.8×10^{16} molec/cm^2 in the north and north east of the city which corresponds to the outflow region on that day. Additionally, increased DSCDs can be found in the south west of the city, where the DSCDs have values around 1.9×10^{16} molec/cm^2. The latter region is most likely influenced by the airport of Frankfurt which will be investigated in more detail in the next section. Sub figure 6.7(b) depicts the second circle that was performed on that day. Unluckily there have been instrumental issues right in the outflow region. But nevertheless slightly enhanced DSCDs can still be found in the north and the east of the city. Also the second (stronger) maximum is still present in the south west of the city. These findings indicate that there could be consistent patterns in the distribution of HCHO if the right conditions are present.

---

[9]This was because my colleague investigates NO_2 emission caused by the city of Frankfurt in her work.

The two sub figures 6.8(a) and (b) show further examples for circles which exhibit clear spatial structures in the HCHO distribution.

(a) 3rd February 10:08 to 10:55 UTC   (b) 25th February 10:04 to 11:07 UTC
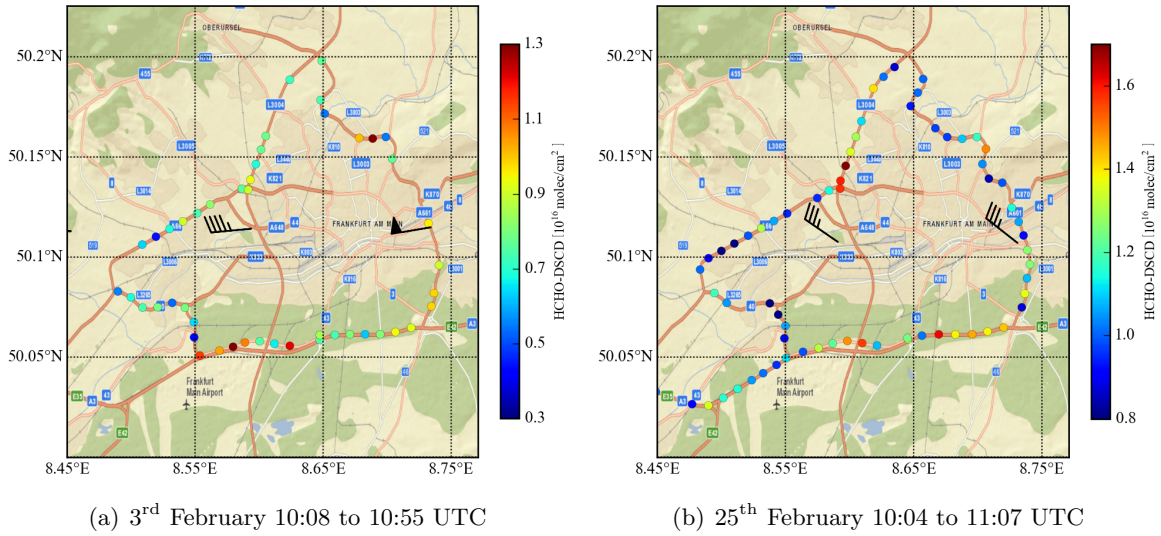
Figure 6.8.: Spatial distribution of the HCHO-DSCDs around Frankfurt/Main on 3rd (a) and 25th (b) February 2016.

On the 3rd February 2016 there was a rather strong westerly wind with wind speeds around $5.0\,\mathrm{m\,s^{-1}}$ present. Enhanced DSCDs can be found in the east and south west of the city. The latter values again might be influenced by the airport and perhaps also by the city of Mainz which is located in the south west of Frankfurt. The increased HCHO-DSCDs in the west of the city seem to be surprising. Nevertheless, they are quite consistent, as they can also be observed on 25th February, where the wind also had a pronounced westerly component. Also other measurement days around Frankfurt exhibit these enhanced columns in the west of the city. Additionally, in section 6.5 we will see that also the NO$_2$ columns are enhanced in this region.

Lastly, we present two maps of cases which show no clear pattern in the spatial distribution of HCHO. Sub figure 6.9(a) exhibits rather high DSCDs all around the city without any obvious structure. The same finding is valid for sub figure 6.9(b) where also no clear patterns can be found.

Overall the situation for the HCHO distribution around Frankfurt seems to be more complex than around Mainz, since there are several additional aspects that have to be taken into account (the airport, the motorways, etc.). Nevertheless, the slight enhancements in formaldehyde are well correlated to the NO$_2$-DSCDs and therefore they seem to be caused by traffic, similar as it was the case in Mainz. This will be more investigated in section 6.5.

6.4.3. Frankfurt Airport

As we have seen in the previous subsection the spatial distribution of formaldehyde around Frankfurt might be strongly influenced by the emissions of the Frankfurt airport. Therefore,

(a) 29th October 10:40 to 11:49 UTC   (b) 23th November 11:50 to 12:47 UTC
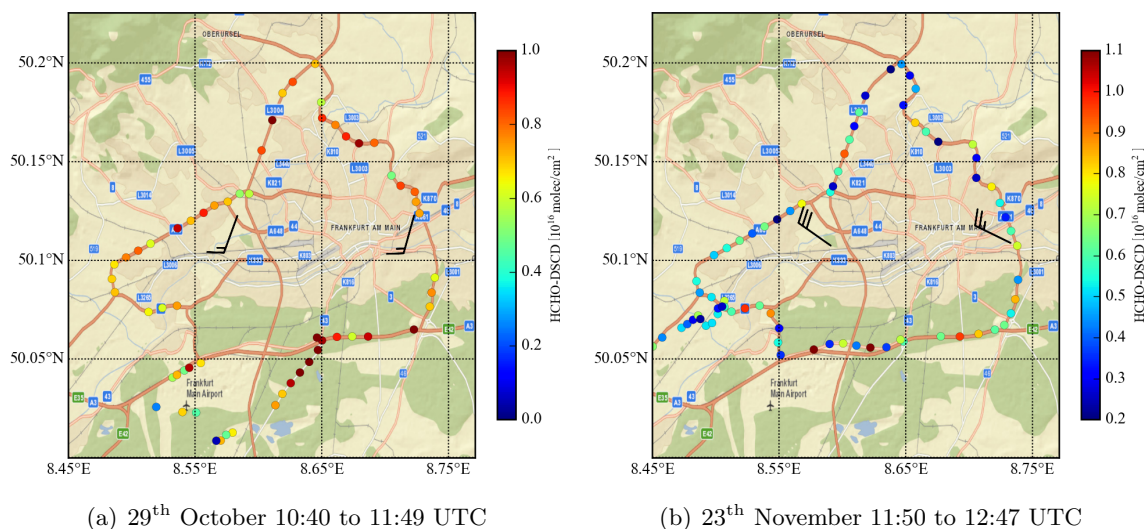
Figure 6.9.: Spatial distribution of the HCHO-DSCDs around Frankfurt/Main on 29th October 2015 (a) and 23th (b) November 2015.

we discus the distribution of the HCHO-DSCDs around the airport in more detail in this section.

Figure 6.10 shows the formaldehyde distribution around the Frankfurt Airport for three selected cases. The respective day and time is indicated by the subtitles of the sub plots. For all three days the wind is coming from different directions.

For the 23th November 2015 the HCHO distribution around the city of Frankfurt showed no clear pattern (see figure 6.9(a)). However, the outflow region of the airport shows a clear enhancement in the formaldehyde DSCDs. Also on 20th December 2015 enhanced DSCDs can be observed in the downwind region of the airport. On both mentioned days the wind is coming from direction which we suppose to bring in clean air as no major city is located in these direction. These two cases indicate the influence of the airport on the formaldehyde distribution around Frankfurt.

On the 17th February 2016 the wind was coming from a north-easterly direction and some pollution might influence the outflow of the airport. However, the outflow again exhibits enhanced HCHO values compared to the inflow region. Similar patterns for the formaldehyde distribution around the airport are found for most of the measurement days. As we will see in the following also here the HCHO-DSCDs are quite well correlated to the NO_2-DSCDs.

6.4.4. Summary

In the previous three subsections examples for the HCHO distribution around Mainz, Frankfurt/Main and the Frankfurt Airport have been presented. For Mainz and the airport clear patterns in the distribution of the HCHO-DSCDs could be identified.

For the measurements in the outflow region of Mainz these patterns fit the wind patterns quite well. Also in the city center, where the most busy roads are located enhanced formaldehyde values can be observed. This fact indicates that there might be a close relation to the

traffic and its emissions, hence most of the measured HCHO might originate from traffic emissions. Therefore, the next section connects both HCHO- and NO_2-DSCDs in order to identify the origin of the formaldehyde in a more proper way.

(a) 23th November 12:47 to 13:31 UTC

(b) 20th December 11:10 to 11:40 UTC

(c) 17th February 12:08 to 12:43 UTC
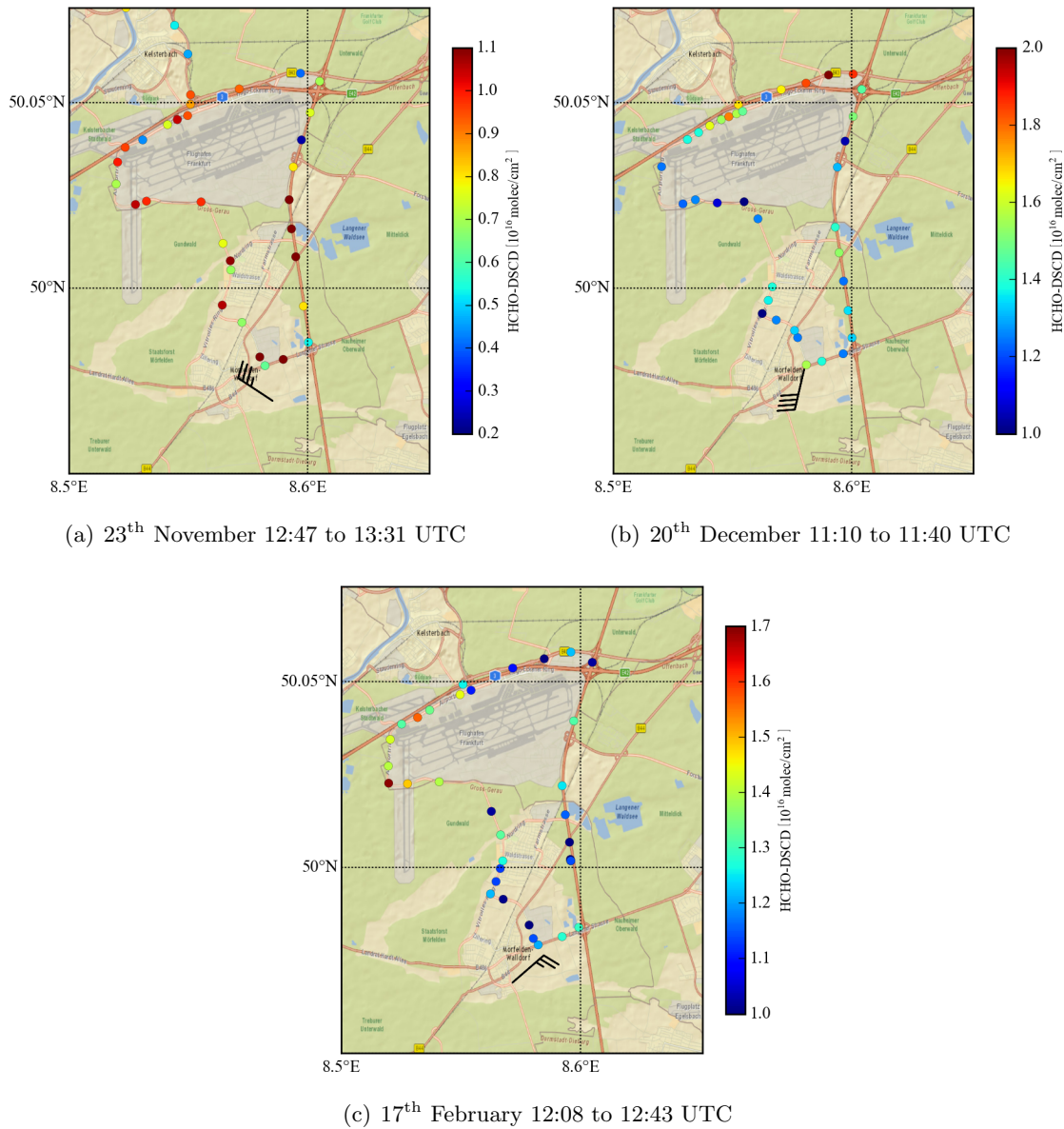
Figure 6.10.: Spatial distribution of the HCHO-DSCDs around the Frankfurt Airport on 23th November (a), 20th December 2015 (b) and 17th February 2016 (c).

The measurements around the city of Frankfurt exhibited clear spatial patterns only for few measurement days. Here the situation might be more complex as the distribution could be influenced by the motorways surrounding the city and the airport which is located in the south of the city. Nevertheless, some measurement days revealed rather clear and consistent patterns of the HCHO-DSCDs. Despite the fact that no measurements were performed within the city we expect that most of the HCHO might also originate from traffic emissions.

Lastly, the HCHO distribution around the airport was presented since it was supposed

to influence the spatial distribution around the city of Frankfurt. Clear patterns could be identified in the outflow region of the airport also on days where the wind was blowing from quite pristine directions. This indicates the importance of the airport for the HCHO distribution around Frankfurt. At the airport the origin of the measured HCHO is supposed to be more complex as the traffic, the engines of the planes and the refueling of the planes might play a role.

In the following the connection between the HCHO- and the NO_2-DSCDs will be investigated in order to learn more about the origin of the measured formaldehyde.

6.5. Correlation to NO_2

In order to better understand the origin of the measured formaldehyde, we investigate the relation between the HCHO- and the NO_2-DSCDs. Therefore, we show maps which depict the spatial distribution of HCHO (upper panels) and also the distribution of the simultaneously measured NO_2 (lower panels). Again first some examples for the three major measurement sites are given for the same selected cases as in the previous section. The maps of all measurement days are also shown together with the HCHO distribution in the appendix (section A.2) of this thesis.

6.5.1. Mainz

We again start with the 5th November 2015 which was the day that exhibits the highest HCHO-DSCDs compared to all other measurement days. The respective trace gas distributions for the different time intervals are depicted in figure 6.11.

Already the first sub figure which shows the distribution for the time period from 10:00 to 11:10 UTC indicates that enhanced values in the NO_2 distribution in general coincide well with enhanced values of formaldehyde, especially inside the city center, where the most traffic is located. However, no clear outflow pattern can be found for the NO_2-DSCDs, as one can observe increased values in the north east and south west of the city.

During the second measurement period the enhancements for both trace gases coincide very well. Rather clear enhancements of NO_2 can be found in the city center of Mainz and in the outflow region of the industrial area of Mainz-Mombach. While the strengths of the enhancements is similar in the city center, the enhancements in the outflow of the industrial area are higher for NO_2 which indicates that there might be different sources for both absorbers. This sounds reasonable as we expect NO_2 emissions from both the traffic and the industry, while the direct emissions of formaldehyde might be dominated by traffic emissions. Only slightly increased values for both trace gases can be observed in the outflow region of the city. Here the intensity of the enhancement is quite similar for both gases.

Finally, the last measurement period on this day exhibits really high DSCDs for both trace gases. For NO_2 this also might be related to the increased stratospheric signal in the afternoon, nevertheless, the spatial patterns fit quite well for both, the HCHO and the NO_2 distribution. This might again indicate that the distribution is dominated by traffic emissions

as the traffic in Mainz usually increases during the afternoon.

(a) 10:00 to 11:10 UTC

(b) 11:10 to 13:00 UTC

(c) 13:00 to 14:00 UTC; 18 UTC wind
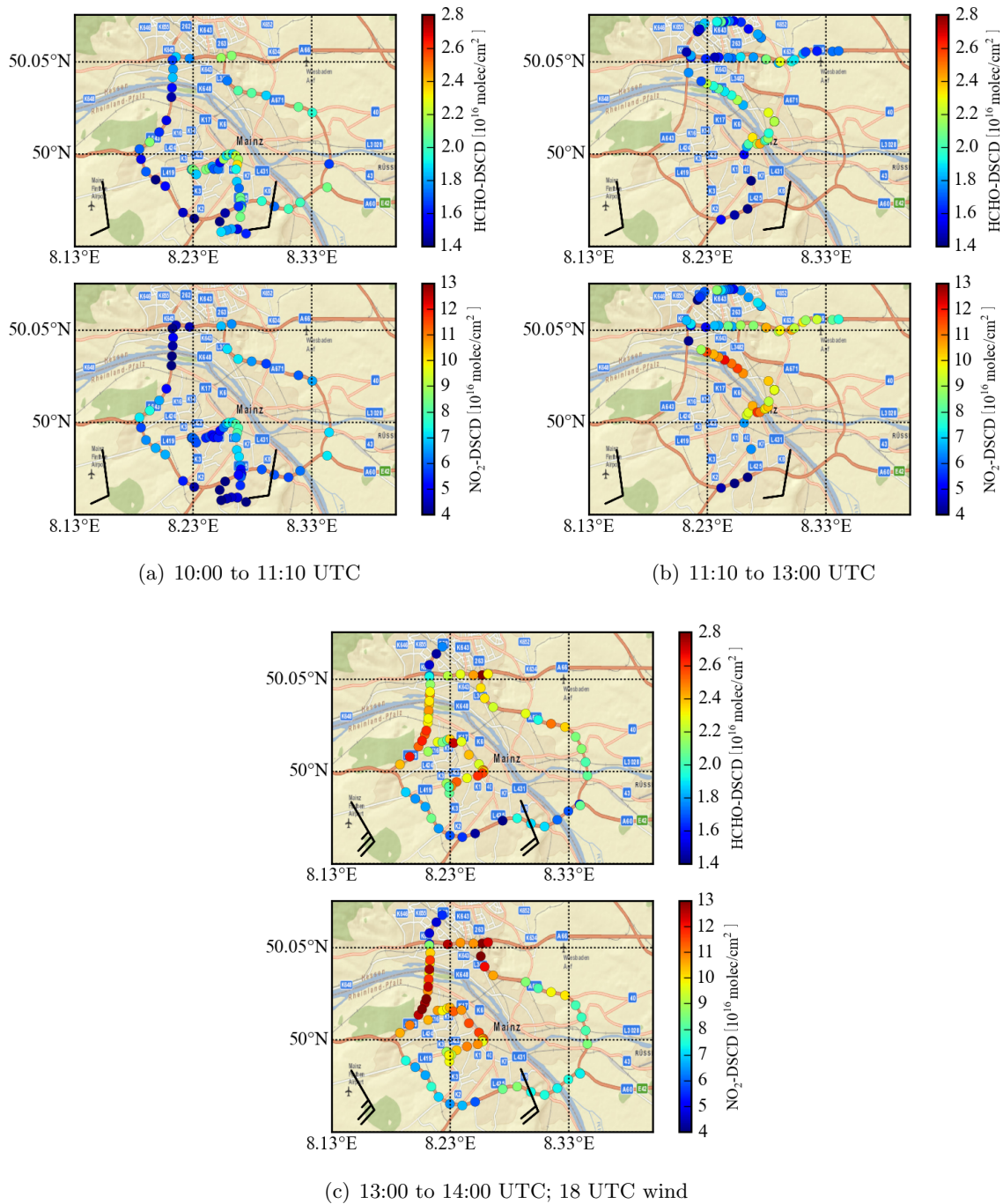
Figure 6.11.: Spatial distribution of the HCHO- (upper panel) and NO_2-DSCDs (lower panel) around Mainz on 5th November 2015 for different time intervals.

On 21st January 2016 similar results can be observed. The respective trace gas distributions are depicted in figure 6.12 for all measurements which were performed on that day. For this day the close relationship between HCHO and NO_2 seems to be more obvious, as for all three measurement periods the spatial distributions of the two trace gases are very similar. Two additional findings are rather interesting. First, also the outflow pattern is clear for both

species for the whole day. This was not the case on 5th November 2015, where the outflow pattern of NO$_2$ did not fit the wind pattern for the morning measurements. Secondly, the unexplained northward shift of the enhanced formaldehyde values can also be observed in the NO$_2$ pattern. This finding indicates that this northward shift is no measurement artefact and the wind data is not accurate enough to capture this correctly.

(a) 10:26 to 11:50 UTC   (b) 11:50 to 12:49 UTC

(c) 12:49 to 13:40 UTC
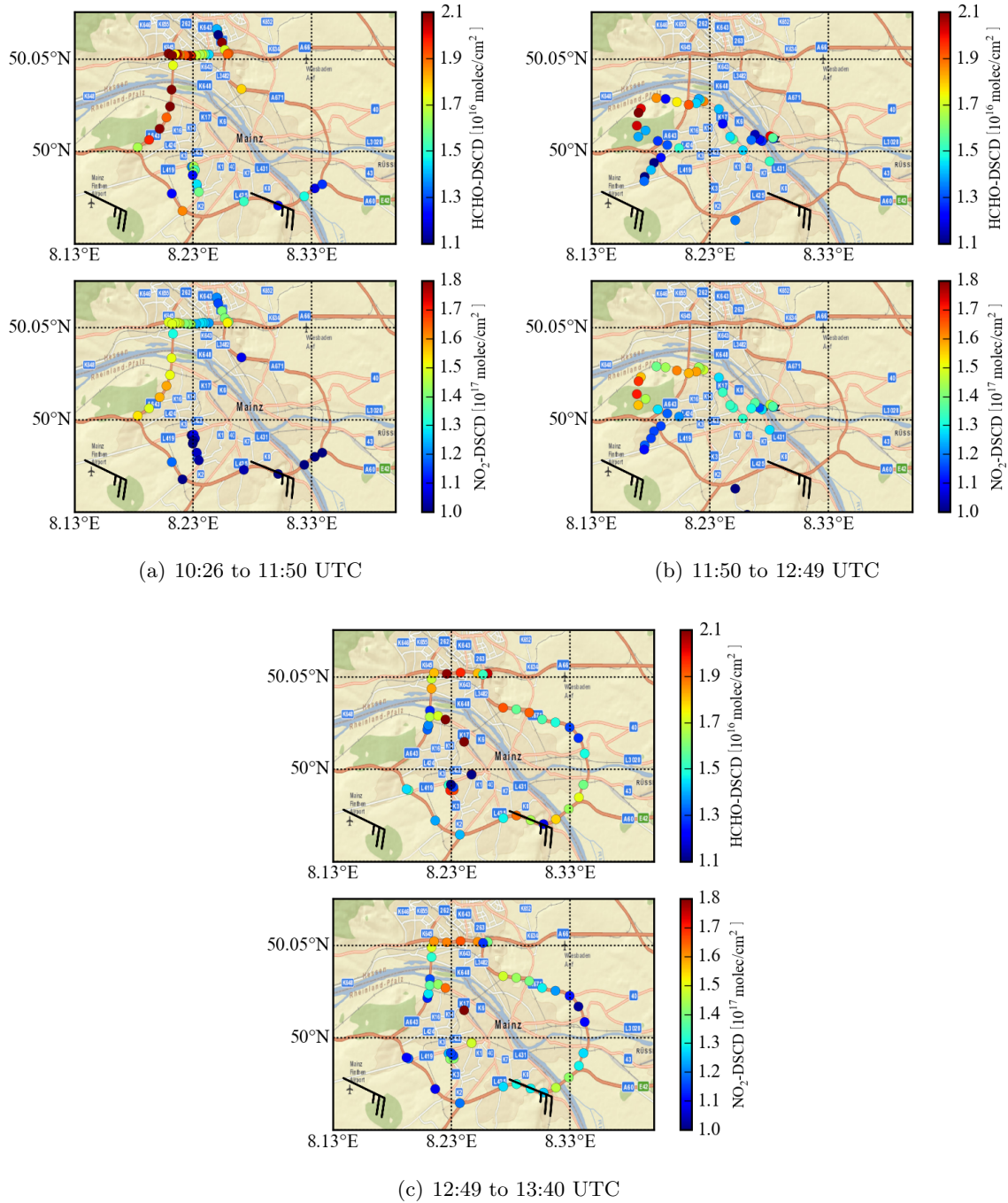
Figure 6.12.: Spatial distribution of the HCHO- (upper panel) and NO$_2$-DSCDs (lower panel) around Mainz on 21st January 2016 for different time intervals.

Another interesting finding for that day is the fact that the highest NO$_2$-DSCDs are almost

one order of magnitude lower than the ones on the measurement day in November. This could be related to the wind speed which was higher on the day in January. So the NO_2 did accumulate less around the city of Mainz but was rather transported away from the city. However, this could not be observed for HCHO, where the DSCDs are only slightly lower compared to the 5th November 2015. This might be caused by the vertical wind profile which in general exhibits higher wind speeds at higher altitudes and the in general different vertical profiles of HCHO and NO_2.

(a) 09:12 to 10:04 UTC

(b) 11:47 to 13:05 UTC

(c) 12:48 to 13:58 UTC
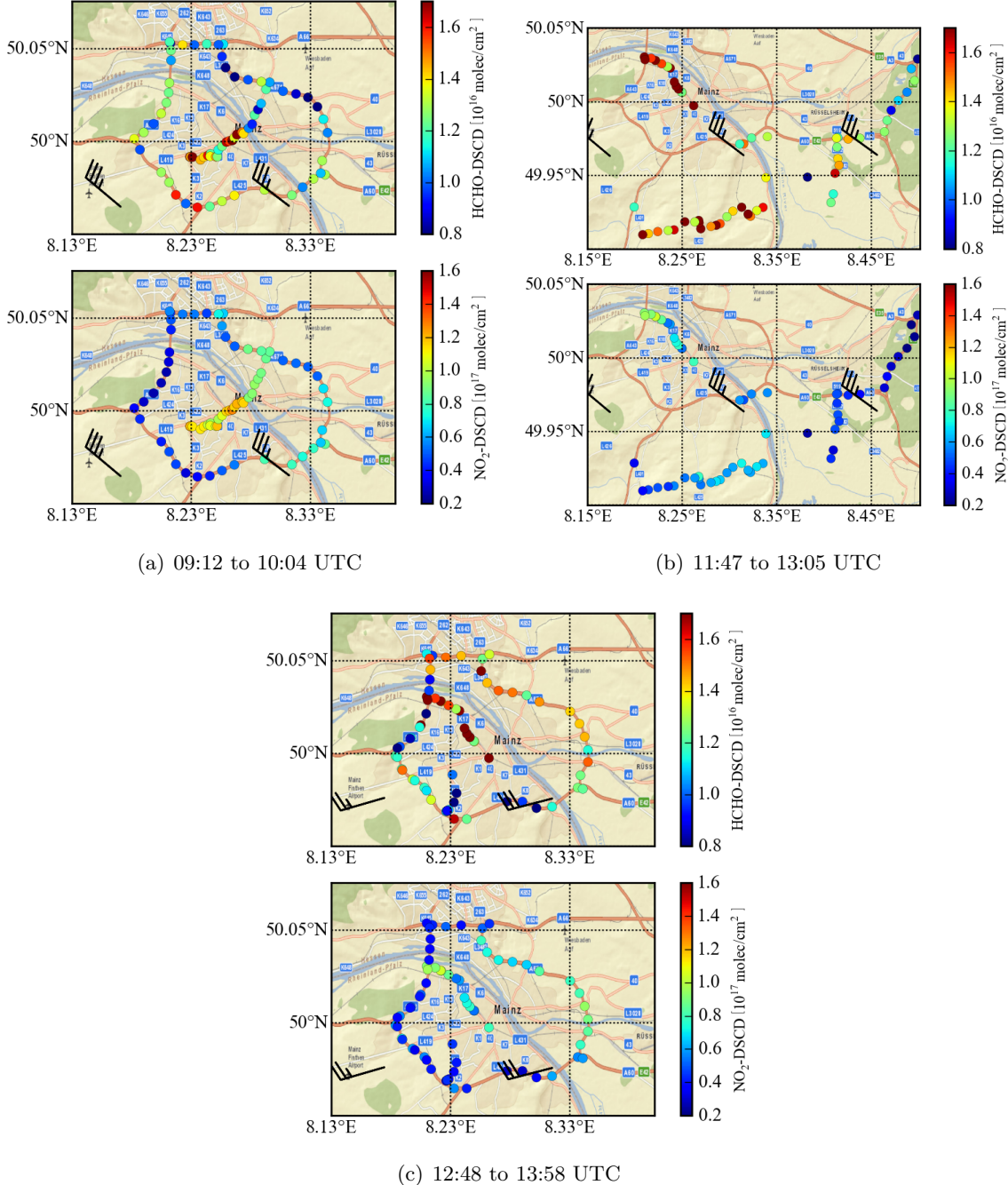
Figure 6.13.: Spatial distribution of the HCHO- (upper panel) and NO_2-DSCDs (lower panel) around Mainz on 25th February 2016 for different time intervals.

Finally, we compare the spatial distribution of HCHO and NO_2 around Mainz for the 25th February 2016 (see figure 6.13). As mentioned already in the previous discussion for that day the outflow of the city was supposed to be somewhere in the south east of the city due to the clear prevailing wind pattern. Slight enhancements of HCHO can be found in the north west and the south east of the city. The NO_2 distribution exhibits enhanced values in the expected outflow region and within the city of Mainz. Therefore, the enhancements of formaldehyde DSCDs in the north west of the city can not be found in the NO_2 data. Nevertheless, a clear correlation between HCHO and NO_2 can be observed inside the city which is most likely due to traffic emissions. Afterwards a route south of Mainz was chosen. Here clear enhancements for formaldehyde can be observed. However, the NO_2-DSCDs only show a slight increase which is somehow surprising and might be related to different lifetimes of the both trace gases. Finally, also the enhancement in NO_2 is not that high as compared to the increase in the formaldehyde values for the last circle which was performed on this day (see sub figure 6.13(c)). Here clear enhanced values can be found inside the city of Mainz for HCHO, while the NO_2 concentrations show only a weak increase.

In summary the consistent patterns in the spatial distribution of formaldehyde which where investigated in the previous section are in general well correlated to the spatial patterns of NO_2 for the measurements in Mainz. However, not all spatial patterns which can be observed for either HCHO or NO_2 can be found in the distribution of the other trace gas. This might indicate that most of the HCHO and NO_2 originates from traffic emissions but there might be additional sources for both gases. Here we only presented results for three selected days of measurements, similar results can also be found for other days. An overview of all days is given in the appendix of this work.

6.5.2. Frankfurt/Main

As it was explained in the previous section the trace gas and especially the HCHO distribution is more complex around Frankfurt since it is influenced by other emissions such as from the airport. Therefore, we hope to learn more about the spatial distribution of formaldehyde by investigating its correlation to NO_2.

Again we start with an representative example from the 20th December 2015, the respective trace gas distributions are presented in figure 6.14.

On that day enhanced formaldehyde DSCDs could be identified in the north and north east of the city. The NO_2 distribution also exhibits enhanced values in the supposed outflow region. A second HCHO maximum can be found in the south west of the city which is most likely due to the influence of the airport. Also there an enhancement of the NO_2 can be observed. However, the enhancement of the NO_2 is more pronounced in the north and north east of the city, while the enhancement of HCHO is stronger close to the airport. This again indicates the influence of the airport emissions. As explained above there were instrumental problems during the second circle on that day which leads to a large gap in the outflow region. Nevertheless, the maximum which might be related to the airport is still present and even more pronounced. A second maximum in the NO_2-DSCDs can be identified in the west of
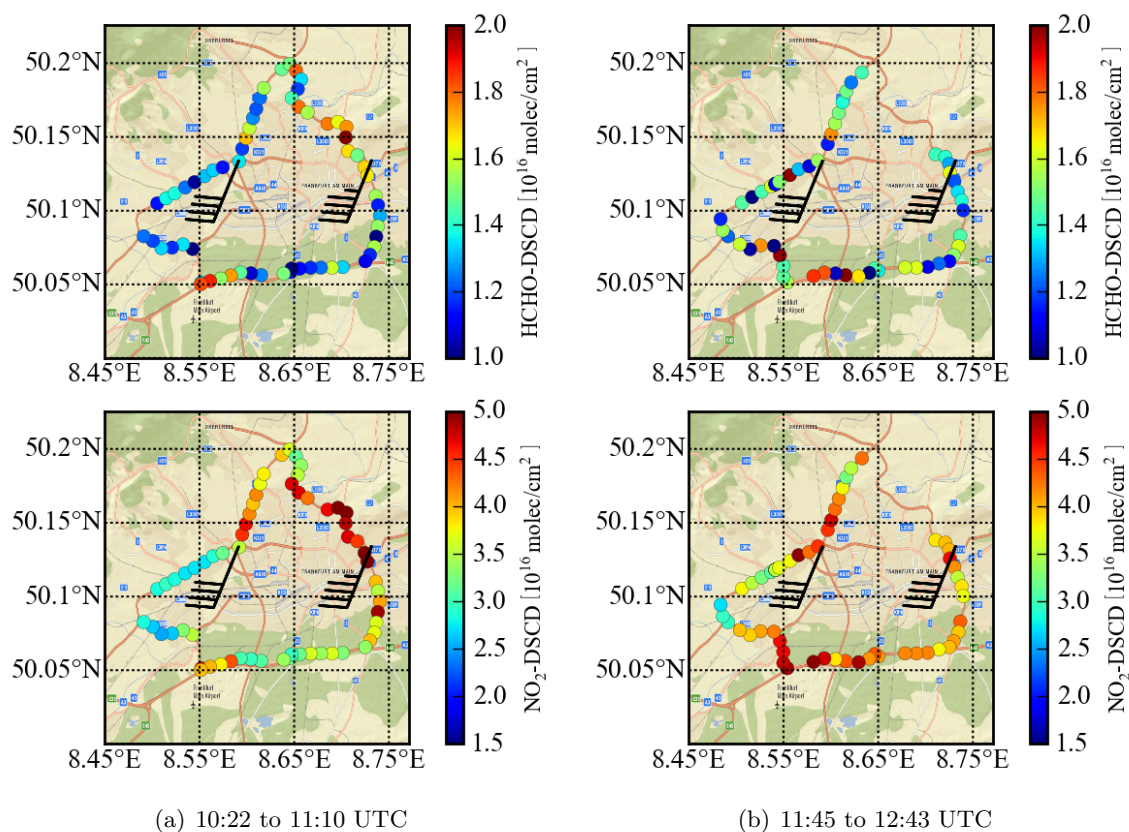
Figure 6.14.: Spatial distribution of the HCHO- (upper panel) and NO_2-DSCDs (lower panel) around Frankfurt/Main on 20th December 2015 for different time intervals.

the city. This second maximum can not be found in the HCHO distribution and does not fit the prevailing wind pattern on that day. Therefore, it remains unexplained for the moment but we will come back to this point later. A first conclusion is that also the NO_2 distribution indicates the more complex distribution of the trace gases around Frankfurt.

Part (a) of figure 6.15 shows the trace gas distributions for one circle around Frankfurt which was performed on 25th February 2016. On this day a north-westerly wind was present and clear outflow patterns in the south and south east of the city can be identified. But as explained already in the previous section, where the HCHO distribution for this day was discussed, a second clear formaldehyde maximum can be observed in the west of the city which does not fit the wind pattern. However, enhanced values for HCHO can be found on several measurement days in the west of the city (e.g. on the 3rd February 2016, compare figure 6.8(a)). As one can see in figure 6.15(a) also the NO_2 columns are enhanced in this region which might indicate an additional pollution source which is located outside of Frankfurt.

Lastly, the spatial distributions of HCHO and NO_2 are compared for the 23th November 2015 (see figure 6.15(b)). On that day no clear pattern which would fit the prevailing wind conditions could be identified for the HCHO values. Despite this finding the NO_2-DSCDs show clear enhancements in the south and south east of the city which seems to be reasonable, when considering the given wind direction. Additionally, the NO_2 columns reach rather high

(a) 25th February 10:04 to 11:07 UTC

(b) 23th November 11:50 to 12:47 UTC
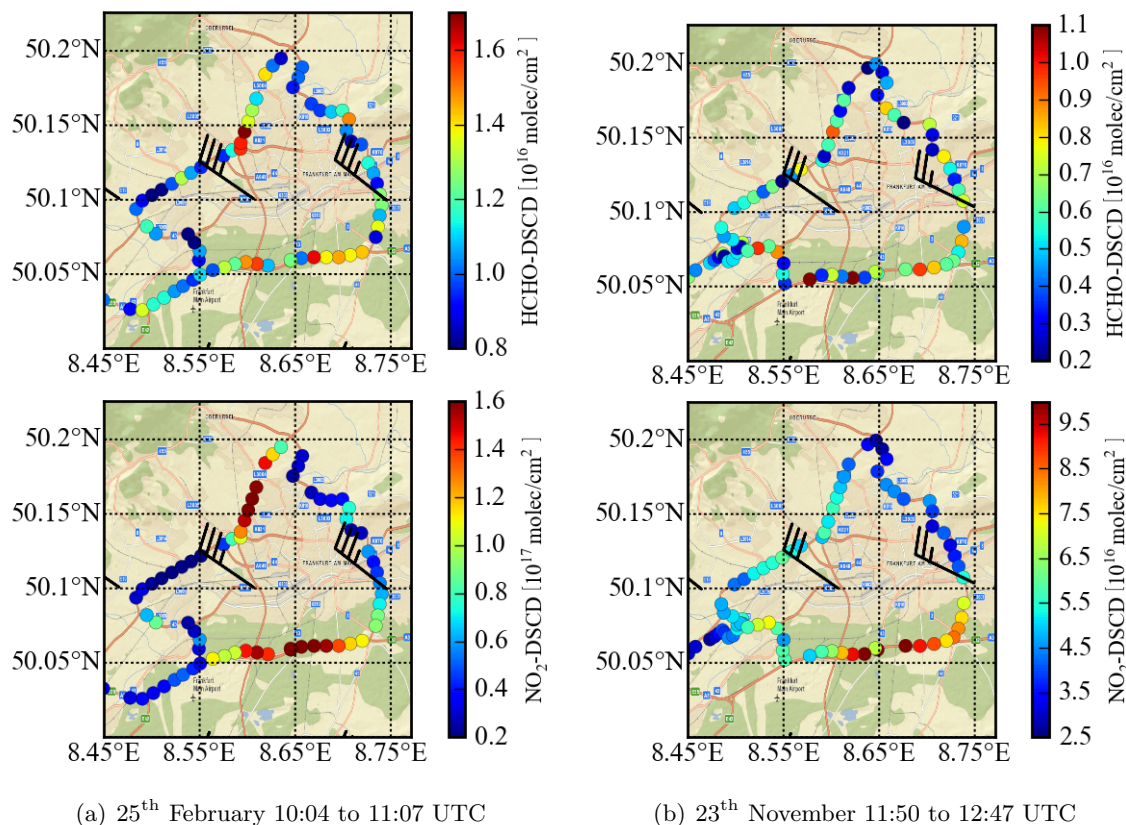
Figure 6.15.: Spatial distribution of the HCHO- (upper panel) and NO_2-DSCDs around Frankfurt/Main on 25th February 2016 (a) and 23th November 2015 (b).

values up to 9.5×10^{16} molec/cm^2. Therefore, it seems to be quite surprising that no pattern could be identified for formaldehyde on that day. As we have seen in the discussions above the HCHO distribution around the Frankfurt airport still exhibits a pronounced pattern on this day.

In conclusion an obvious but variable relationship between the HCHO- and NO_2-DSCDs could be observed also around Frankfurt. However, the situation is more complex around Frankfurt and a higher variability was found.

6.5.3. Frankfurt Airport

Finally, a short comparison of the HCHO and NO_2 distribution around the Frankfurt airport will be presented in this section.

In contrast to NO_2 on 23th November 2015 the formaldehyde distribution around the city of Frankfurt showed no clear spatial pattern. However, around the airport the situation is rather different, a clear outflow pattern can be identified in the east of the airport. The respective HCHO and NO_2 distribution for these measurements is illustrated in figure 6.16(a). It is obvious that also the NO_2-DSCDs are enhanced in the east of the airport, but the increased NO_2 values are shifted more to the south. In addition, the NO_2 columns are not only enhanced in the eastern part of the airport but in the whole southern part of the airport. In the north

(a) 23th November 12:47 to 13:31 UTC   (b) 20th December 11:10 to 11:40 UTC
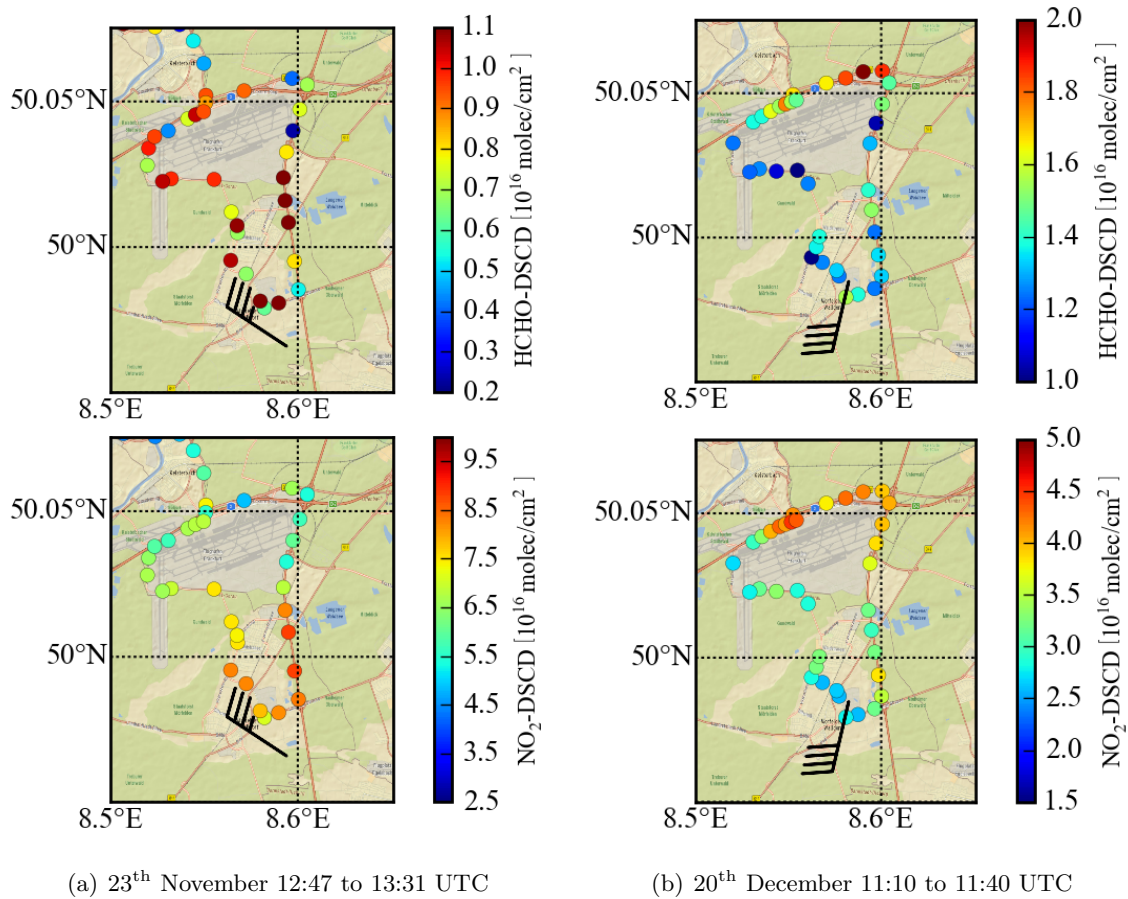
Figure 6.16.: Spatial distribution of the HCHO-DSCDs around the Frankfurt Airport on 23th November (a) and 20th December 2015 (b).

of the airport also a very busy motorway is located and as the wind is coming from north-westerly directions the NO_2 distribution might be influenced from both, the traffic emissions from the motorway and the emissions caused by the airport. Since the highest NO_2-DSCDs still can be found in the south east of the airport there the both different sources might overlap. For HCHO the airport seems to be the more important source since its distributions shows a sharper maximum in the east of the airport, nevertheless, also some enhancements can be found in the south of the airport.

Figure 6.16(b) shows the trace gas distributions for the 20th December 2015. Also this day shows enhanced formaldehyde colums in the outflow region of the airport. Again these enhancements coincide with increased NO_2 values, however, again the patterns for HCHO and NO_2 are somehow shifted against each other. This once more reveals the more complex situation around Frankfurt and especially close to the airport.

Similar results can be found for the spatial distribution of the trace gases around the airport also for several other measurement days. Again an overview on all measurements can be found in the appendix of this thesis.

6.5.4. Summary

The last three subsections provided a comparison of the HCHO and NO_2 distributions round our three major measurement sites.

For Mainz a clear correlation between the two trace gases could be identified for most of the measurement days. This indicates that most of the HCHO might originate from traffic emissions (especially in the city center) as NO_2 is one of the major pollutants originating from car emissions. However, on some measurement days some modifications in the relation between the two trace gases have been observed. Therefore, also other sources such as industries in the Mainz-Mombach region might be important for the NO_2 distribution.

Around the city of Frankfurt clear patterns for the HCHO distribution could be identified only in a few cases. In contrast the NO_2 distribution exhibits clear spatial patterns for almost all measurement days. So a lot of NO_2 seems to be emitted within the city center. The patterns of both trace gases are more or less consistent, however, the situation might be more complex compared to Mainz.

The Frankfurt airport heavily influences the trace gas distribution in the Frankfurt area, especially when the wind is coming from south-westerly directions which is the main wind direction in this region. Also here the spatial patterns of both trace gases fit quite well. Nevertheless, there seems to be a slight shift between both gases. This might indicate that there are different sources for both trace gases which may overlap somehow.

In conclusion all results we obtained so far indicate that traffic emissions are the main source of formaldehyde in the measurement region. This is quite reasonable as the measurements were performed in the winter/spring period of the year. At this time the biogenic activity is rather low and also photochemical processes are less important since the incident radiation is low.

In the following section so-called emission ratios are calculated in order to learn more about the origin of the measured HCHO.

6.6. Emission Ratios

In the following emission ratios ($HCHO/NO_x$) are calculated following the procedure from Klemp et al. (2002). Therefore, first the HCHO data is plotted against the NO_x data. As we are only able to measure NO_2 with our measuring system, we use a conversion factor to convert the NO_2- to NO_x-DSCDs and VCDs, respectively. This conversion factor depends on the radiation that is available for reaction 3.2 which was explained in section 3.1. Therefore, in general in winter the fraction of NO_2 which is contained in the total NO_x is larger than in summer. Additionally, the amount of available radiation depends on the atmospheric conditions. Thus the conversion factor might cover a range from 1.1 to 1.8 (Steffen Beirle, 2016), but since our measurements took place mainly in winter we choose a fixed conversion factor of 1.4.

After that a linear regression is performed and one derives a straight line of the form $y = b + m \cdot x$, where y and x indicate the formaldehyde and the NO_x data, respectively.

The quantity m represents the emission ratio HCHO/NO$_x$, while the y value at a low NO$_x$ concentration can be interpreted as HCHO background.

As regression method two different approaches were used. The first is a simple polynomial fit of first order which will be indicated by "PolyFit" in the following. The second approach is an orthogonal total least square fit which also takes measurement errors into account and weights the different data points according to their respective error values. For the representation of the errors we use the fit error which is also an output quantity of the WinDOAS fit result. However, as it is explained later on this choice of the error representation is not perfect. This second approach will be indicated by "TLS" in the following figures.

Below we present the daily emission ratios for both DSCDs and VCDs. In the last part of this section mean ratios are calculated and compared to the values Klemp et al. (2002) obtained.

6.6.1. Daily Emission Ratios

These two approaches were used for all measurement days. In this way we obtain daily emission ratios for all days of measurements. First, we present the results obtained by the DSCDs.

Therefore, figure 6.17(a) shows an example for a daily result which exhibits a quite good correlation ($R^2 = 0.27$) between the both trace gases. The regression results for the two approaches are indicated by the green and red lines, respectively. Also the respective colour was used to display the emissions ratios as well as the resulting R^2. On that day the PolyFit method yields a ratio of 0.058, while the TLS approach results in a slightly higher value of 0.061. So both approaches lead to quite similar results on that day.

(a) 29th January 2016   (b) 17th March 2016
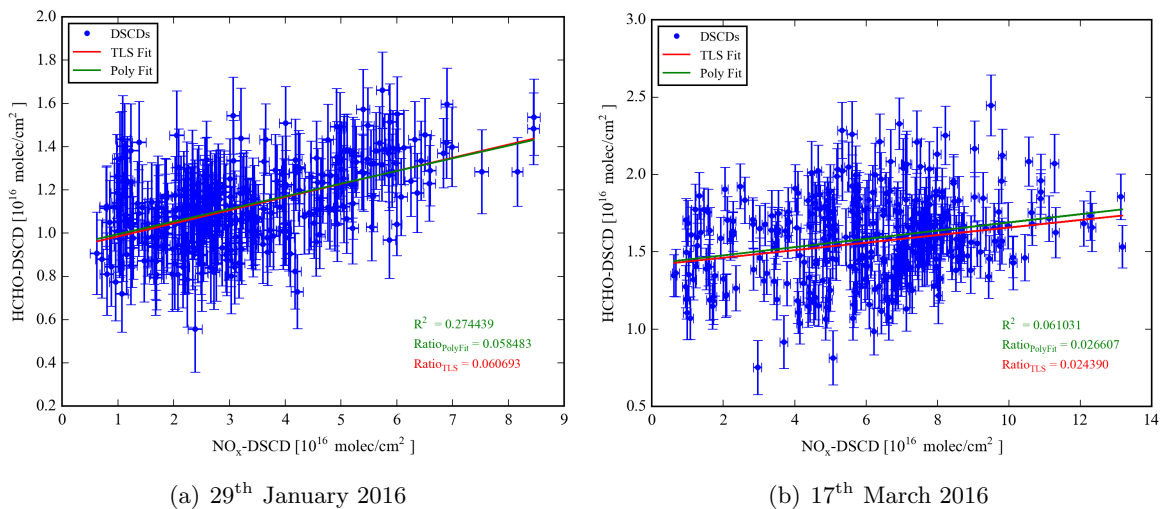
Figure 6.17.: HCHO-DSCDs plotted against NO$_x$-DSCDs for (a) 29th January 2016 and (b) 17th March 2016. The regression results are represented by the green and red line, respectively. The emission ratios for the two approaches are indicated by the respective colour.

Figure 6.17(b) depicts the same correlation plot for a day with a low R^2 of only 0.06. The both regression methods yield ratios of 0.027 and 0.024, respectively, for that day. Again both

methods obtain consistent results which is valid for all measurement days for the DSCDs. An overview on all daily correlation plots is provided in section A.3 in the appendix of this thesis. Further, table 6.1 gives an overview on all daily emission ratios.

(a) 29th January 2016 (b) 17th March 2016
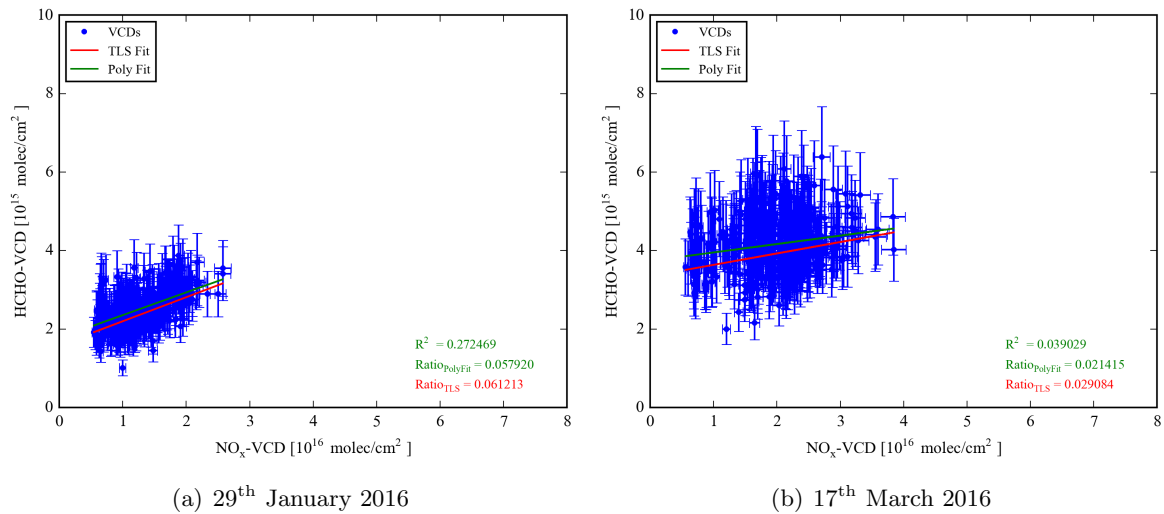
Figure 6.18.: HCHO-VCDs plotted against NO_x-VCDs for (a) 29th January 2016 and (b) 17th March 2016. The regression results are represented by the green and red line, respectively. The emission ratios for the two approaches are indicated by the respective colour.

Next two examples for the results obtained for the VCDs are presented. Here a fixed relative measurement error was assumed for all VCDs (5 % for the NO_x-VCDs and 20 % for the HCHO-VCDs), however, as we will see later this procedure brings up some issues. For comparison reasons the same days as for the DSCD approach were selected. Figure 6.18(a) again shows the correlation plot for 29th January 2016. The VCD approach yields a R^2 of 0.27 which is nearly the same value as for the DSCD case. Also the respective ratios yield values (0.058 for the PolyFit and 0.061 for the TLS approach) that are comparable to the ratios obtained by the DSCD method.

Finally, figure 6.18(b) shows the correlation plot for 17th March 2016 here the respective R^2 exhibits a low value of only 0.04. Nevertheless, the obtained emission ratios (0.021 for the PolyFit and 0.029 for the TLS approach) are in good agreement to each other and also to the respective ratios resulting from the DSCD method for that day.

These four figures only act as examples for selected cases. An overview on all correlation plots is given in the appendix. However, these selected cases are representative for days with good and days with bad R^2. Despite this the obtained daily emission ratios vary within a range of around 0.03 to 0.1, if we neglect the ratios for days, where the R^2 was 0.10 and smaller. One possible explanation for this is the fact that our daily correlation plots contain all the data which was recorded on that day. Also we performed measurements at different measurement sites on each day. Therefore, our measurements might be influenced by different emission sources which could be anthropogenic or biogenic. Klemp et al. (2002), however, only measured in the outflow of one city and filtered and averaged the data. Another reason for the large range of obtained emission ratios might be that also the meteorological and

environmental properties could vary a lot between the different measurement days. In order to minimise some of these effects mean emission ratios are calculated in the next section.

Date	R^2_{DSCD}	$Ratio_{PolyFit}^{DSCD}$	$Ratio_{TLS}^{DSCD}$	R^2_{VCD}	$Ratio_{PolyFit}^{VCD}$	$Ratio_{TLS}^{VCD}$
12.10.2015	0.16	0.040	0.042	0.14	0.039	0.040
13.10.2015	0.12	0.050	0.042	0.10	0.046	0.020
27.10.2015	0.19	0.047	0.058	0.24	0.065	0.068
29.10.2015	0.16	0.047	0.053	0.16	0.047	0.094
30.10.2015	0.02	0.010	0.008	0.02	0.010	0.084
05.11.2015	0.56	0.067	0.064	0.56	0.067	0.066
11.11.2015	0.01	0.010	0.014	0.01	0.010	0.174
23.11.2015	0.16	0.041	0.039	0.11	0.032	0.039
20.12.2015	0.31	0.138	0.135	0.24	0.125	0.126
08.01.2016	0.13	0.035	0.037	0.15	0.039	0.104
21.01.2016	0.43	0.074	0.072	0.43	0.074	0.076
22.01.2016	0.22	0.038	0.043	0.22	0.038	0.041
29.01.2016	0.27	0.058	0.061	0.27	0.058	0.061
03.02.2016	0.14	0.035	0.037	0.14	0.035	0.048
17.02.2016	0.15	0.019	0.019	0.14	0.019	0.018
25.02.2016	0.15	0.027	0.027	0.15	0.027	0.081
14.03.2016	0.01	0.022	0.021	0.01	0.013	-0.021
17.03.2016	0.06	0.027	0.024	0.04	0.021	0.029

Table 6.1.: Overview on the obtained daily emission ratios for all four approaches.

6.6.2. Mean Emission Ratios

Next mean emission ratios were calculated for all of the four approaches. As it was shown in the previous section for some days the R^2 is quite low, therefore only the emission ratios of those days were averaged which exhibit R^2 values of 0.1 and larger. The mean ratios were calculated by weighting the different daily emission ratios with respect to their respective R^2 values.

Figure 6.19 shows an overview on both the daily emission ratios for all four approaches and the mean ratios which where obtained by the averaging procedure. The daily ratios are represented by coloured circles (see legend for more information), while the mean ratios are depicted as horizontal lines with their respective colour. Though not all daily ratios were used to calculate the mean ratios, all of them are displayed in figure 6.19 (ratios which were not used to calculate the mean ratios are represented by crosses with the respective colour). Finally, the horizontal black line indicates the emission ratio obtained by Klemp et al. (2002).

Our measurements yield mean emission ratios of 0.060, 0.060, 0.059 and 0.069 for the four different approaches. The results for the two PolyFit approaches are nearly identical and also the TLS approach results in a consistent ratio for the DSCDs. Nevertheless, for the VCDs the TLS method obtains a mean emission ratio of 0.069 which is higher as the other three values. This finding is most likely caused by the used error assumption for the VCDs. As it was explained above we simply assumed a relative error and since the TLS fit weights the fit
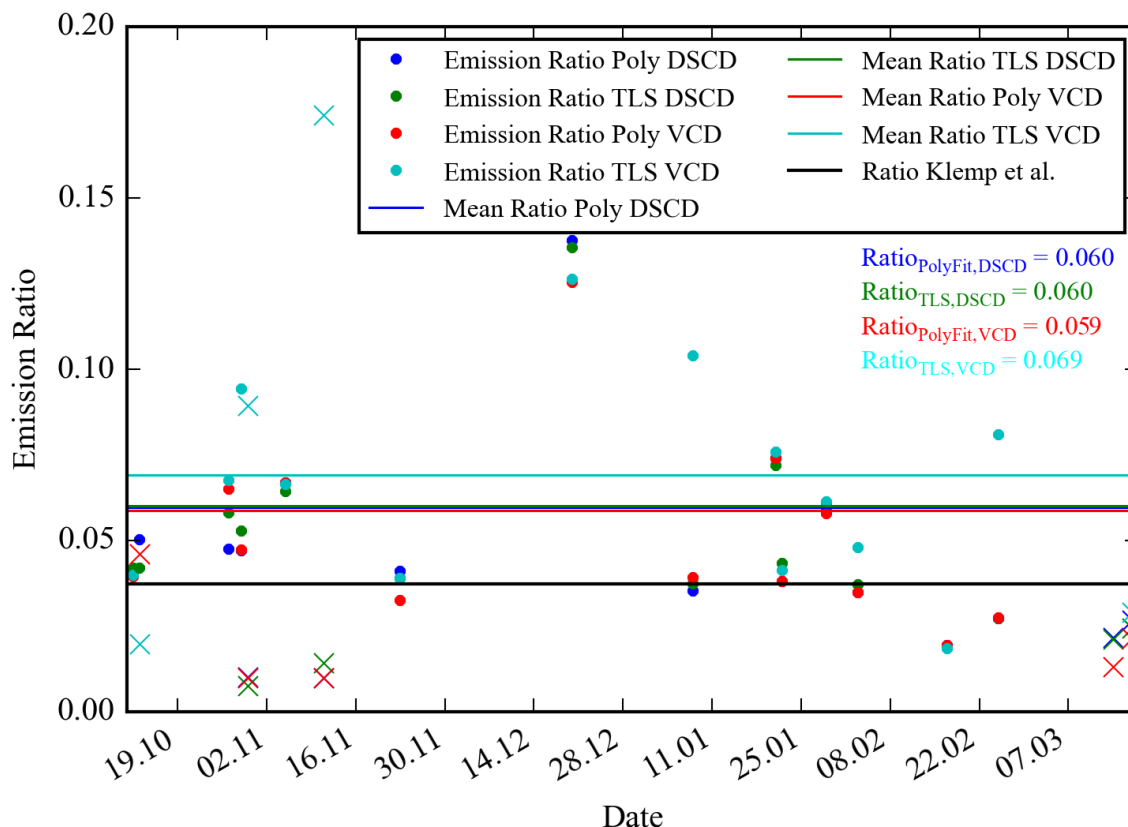
Figure 6.19.: Overview on the obtained emission ratios. Daily ratios are denoted with coloured dots. Daily ratios which were not used for the averaging are denoted by crosses with the respective colour. Mean ratios are represented by coloured horizontal lines. The respective values for the emission ratios are shown with the respective colour.

with respect to the absolute error, the lower VCDs have more weight within the TLS fitting process. This leads to a tilt of the fitted line which results in a higher slope and therefore in a higher emission ratio. For this reason not too much attention should be paid to the TLS result for the VCDs. However, in future it is planned to use a more sophisticated assumption for the errors of the VCDs. In addition to the weighted mean also the weighted standard deviation was calculated for each of the four approaches and values of 0.036, 0.035, 0.031 and 0.034 were obtained. This quantity can be used as a measure for the spread of the daily emission ratios which were averaged. If we use these standard deviations as a first rough error of the mean emission ratios our relative errors are around 60 % and all four obtained mean ratios are consistent within their respective uncertainties.

As a last and slightly different method the HCHO- and NO_x-DSCDs of all measurements were plotted against each other (see figure 6.20) and a polynomial fit as well as a TLS fit is applied to the whole dataset. All DSCDs of one measurement day are displayed in the same colour, the green and red lines indicate the regression results for the polynomial fit and the TLS fit, respectively. Using this method, lower emission ratios of 0.041 and 0.042 are obtained for the two fitting procedures. The respective R^2 exhibits a value of 0.18. The results of this method are only shown for the DSCDs, nevertheless, the VCDs yield similar

results. Table 6.2 provides an overview on all obtained mean emission ratios.
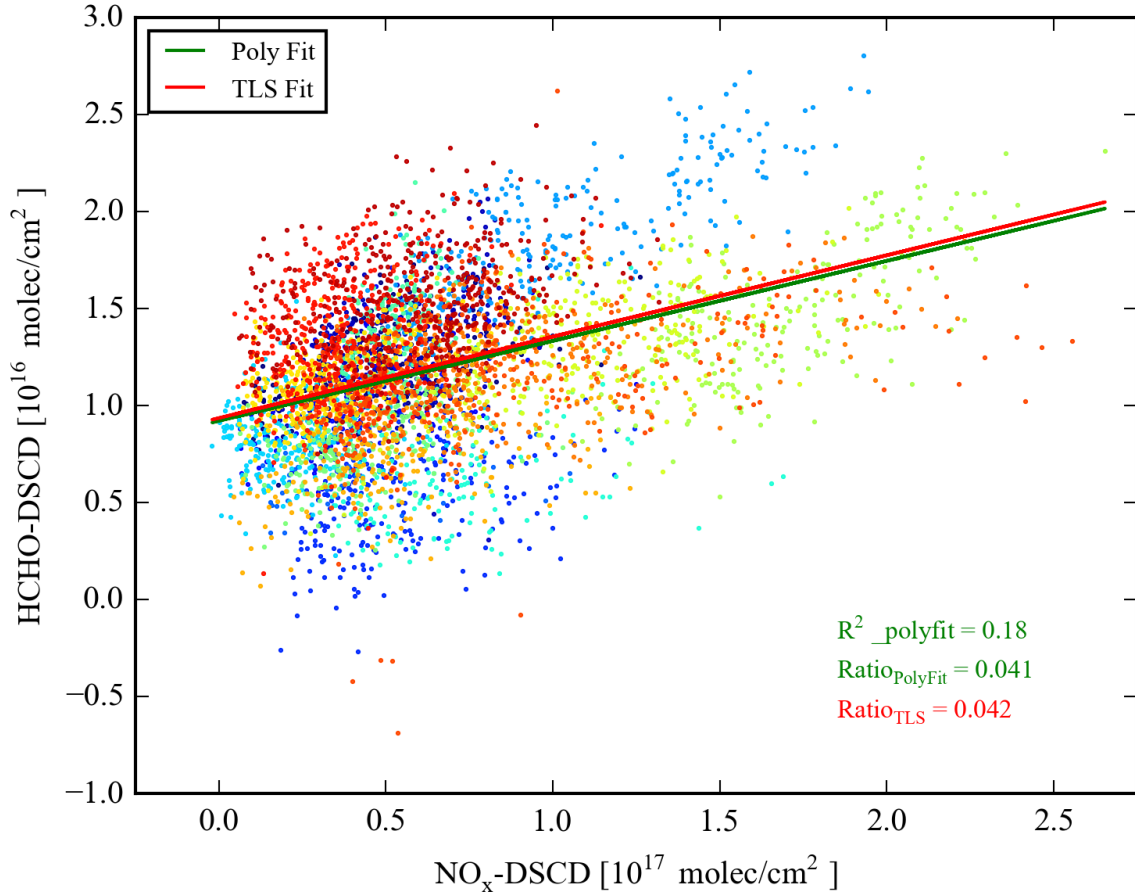
Figure 6.20.: All HCHO-DSCDs plotted against all NO_x-DSCDs. The different colours of the dots indicate the different measurements days. The regression results for the polynomial fit and the TLS fit are depicted in green and red, respectively. The values for the emission ratios are shown with the respective colour.

Approach	HCHO/NO_x	Uncertainty[10]
PolyFit, DSCD	0.060	0.036
TLS, DSCD	0.060	0.035
PolyFit, VCD	0.059	0.031
TLS, VCD	0.069	0.034
All Data, PolyFit	0.041	–
All Data, TLS Fit	0.042	–
Klemp et al. (2002)	0.029 - 0.037	0.005

Table 6.2.: Overview on the obtained mean emission ratios for the different approaches. In addition, the Klemp et al. (2002) value is displayed. The uncertainty is only displayed, where a reliable values was calculated.

---

[10]For our measurements the uncertainty is the weighted standard deviation.

Klemp et al. (2002) obtained emission ratios in the range of 0.029 to 0.037 for their measurements which were performed in March and October in the outflow of Augsburg. We find ratios which are higher than these values. There might be different reasons for this. The first is the fact that Klemp et al. (2002) use a Hantzsch instrument to measure HCHO mixing ratios which is an in-situ measuring system. We on the contrary used DOAS measurements which is a remote sensing system and averages the concentrations of the different trace gases along the respective light path. Therefore, not only trace gases which are located close to the ground are measured but also elevated trace gas layers. These layers might be older and the trace gas ratios could already be changed by different chemical processes. Also the different vertical distributions of both trace gases will influence the obtained ratios as the NO_x is in general expected to be located close to the ground, while the formaldehyde typically reaches higher altitudes. Thus we expect in general higher ratios for the MAX-DOAS measurements compared to the in-situ measurements and the observed systematic discrepancy between our and the Klemp et al. (2002) measurements seems to be reasonable. A second effect was already mentioned above and is related to our measurement strategy which was meant to map the distribution of formaldehyde and to estimate emissions of NO_x (work of my colleague). Therefore, not only measurements in the outflow region were performed and the respective trace gas concentrations are most likely influenced by other sources outside the outflow. In addition, also Slemr et al. (1996) obtained larger emission ratios of 0.050 in the plume of Freiburg.

Nevertheless, if we take the uncertainties of our mean emission ratios into account, overall a quite reasonable agreement is found between our emission ratios and those obtained by Klemp et al. (2002) and Slemr et al. (1996). Also our rough approach and the different measuring principle should be noted.

6.7. Comparison to Bucharest Data

In this section the results which were obtained by the measurements in the Frankfurt/Rhein-Main area are compared to data which was acquired during the AROMAT2 campaign. This campaign took place in Romania in summer 2015. It was a large intercomparison campaign with a lot of participants and two major measurement sites. One was Turceni which is a town located in the Jiu Valley in the south west of Romania. This valley contains several coal power plants and exhibits very high pollution. The second measurement site was Bucharest which is the capital of Romania and has a total population of around 2 million people. It also exhibits a lot of traffic, especially during the rush hours. As the trace gas distribution in the Jiu Valley is heavily influenced by the different power plants, in the following the Rhein-Main data is only compared to the measurements which were performed in and around Bucharest. Since the weather was quite bad at the beginning of the campaign only three days of reasonable measurements remain for Bucharest.

Additionally, it has to be noted that slightly different DOAS analysis settings were used for the Romania measurements. The largest difference is the fact that an additional absorber, namely SO_2 was fitted to the spectra, since the SO_2 concentrations are sometimes very high

in Romania. Also a slightly different fitting interval (324 to 359 nm) was used.

6.7.1. Spatial Distribution

First, the spatial distributions of formaldehyde and NO_2 are compared for the both measurement regions. Figure 6.21 shows the spatial distributions of HCHO and NO_2 around Bucharest for 18th and 31st August 2015. An overview which shows the spatial distribution for all three measurement days is attached in the appendix (see section A.4).

On both presented days the formaldehyde DSCDs around Bucharest are significantly higher than those in the Rhein-Main area. This finding is reasonable since the measurements in Bucharest were performed in summer, where we expect higher HCHO columns.

For formaldehyde on both days a clear outflow pattern fitting the wind patterns can be observed. Nevertheless, on 31st August (see sub figure (c) of figure 6.21) very high DSCDs up to 20×10^{16} molec/cm^2 were found within the city of Bucharest. These high values are most likely influenced by direct traffic emissions as the roads were very busy on that day. But also a pronounced outflow pattern can be found for this measurement day. Here the DSCDs are smaller which is probably related to the relatively short atmospheric lifetime during summer due to high photochemical activity. During the second circle that was performed on that day the highest DSCDs are found in the outflow region of the city which indicates changed emission patterns as well as changed photochemical properties of the atmosphere.

The DSCDs on the 18th August are smaller compared to those on 31st August. This effect might be related to the different meteorological properties since it was cloud-free and hot weather on the second day, while the temperatures where much lower on the first day, where also some clouds were present.

Also for NO_2 in most of the cases clear outflow patterns can be observed. However, in the morning of 31st August, where very high formaldehyde DSCDs could be found in the city the NO_2 distributions did not fit to this pattern. In this case also the highest NO_2 values are found within the city but the spatial patterns seems to be shifted compared to the HCHO-DSCDs. The outflow region which is obvious for formaldehyde and located in the east of the city can not be found for NO_2. On the contrary, a NO_2 maximum can be identified in the north of the city. Here only slightly enhanced HCHO columns can be observed. Also on the other measurement days the spatial patterns of HCHO and NO_2 differ more than the respective patterns for the measurements in the Rhein-Main area.

This finding as well as the significantly higher DSCDs around Bucharest indicate the different measurement conditions since the measurements where performed at different sites and at different seasons. Furthermore, this outcome is an indicator for different chemical properties of the atmosphere and in particular for an important (maybe dominant) contribution of secondary produced formaldehyde from both anthropogenic and biogenic sources.

6.7.2. Emission Ratios

In the second part of the comparison the emission ratios obtained around Bucharest during the AROMAT2 campaign are compared to those ratios which were obtained in the
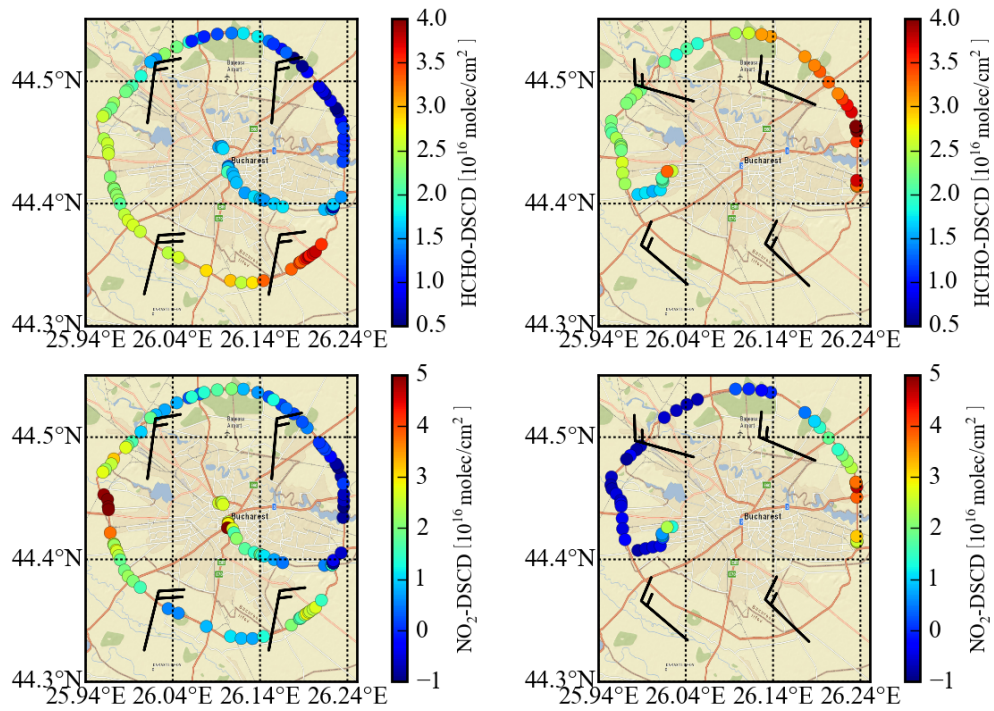
(a) 06:45 to 09:30 UTC

(b) 10:19 to 12:00 UTC
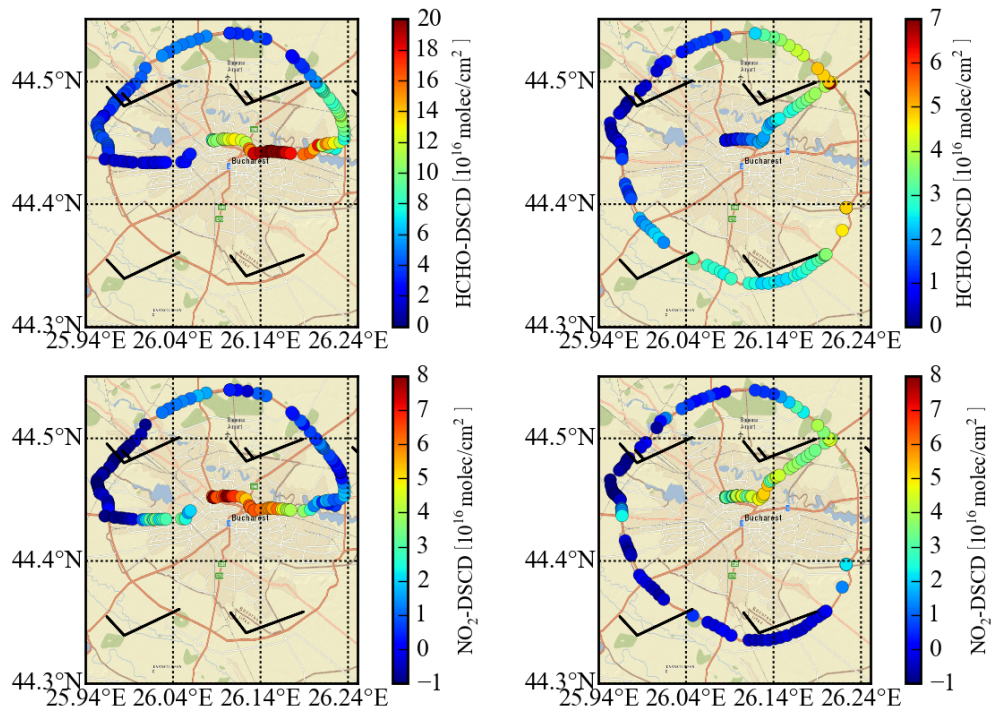
(c) 08:45 to 10:30 UTC

(d) 13:00 to 16:00 UTC

Figure 6.21.: Spatial distribution of the HCHO- (upper panel) and NO$_2$-DSCDs (lower panel) around Bucharest on 18th August 2015 are represented by sub figures (a) and (b). The respective distributions for 31st August 2015 are depicted in the sub figures (c) and (d).

Frankfurt/Rhein-Main area. The ratios were calculated only for the DSCDs since the results for DSCDs and VCDs are consistent. Figure 6.22 depicts the correlation plots for the three measurement days around Bucharest.

For 18th and 31st August quite good R^2 values of 0.32 and 0.13, respectively, can be observed. The R^2 for the 30th August yields a value of only 0.02 and no clear correlation can be found on that day. The obtained emission ratios cover a range of around 0.04 to 1.00 and show very different values for all of the three measurement days. Also the two different approaches (PolyFit and TLS) yield large discrepancies for the emission ratios of one day. This larger overall variability in the ratios again indicates the influence of secondary produced formaldehyde which might dominate the emissions during summer time. Also the effect of biogenic HCHO is larger during summer. Since the method used by Klemp et al. (2002) is meant to determine anthropogenic emission ratios, it might fail during summertime due to the mentioned influence of both secondary and biogenic produced HCHO.

(a) 18th August

(b) 30th August
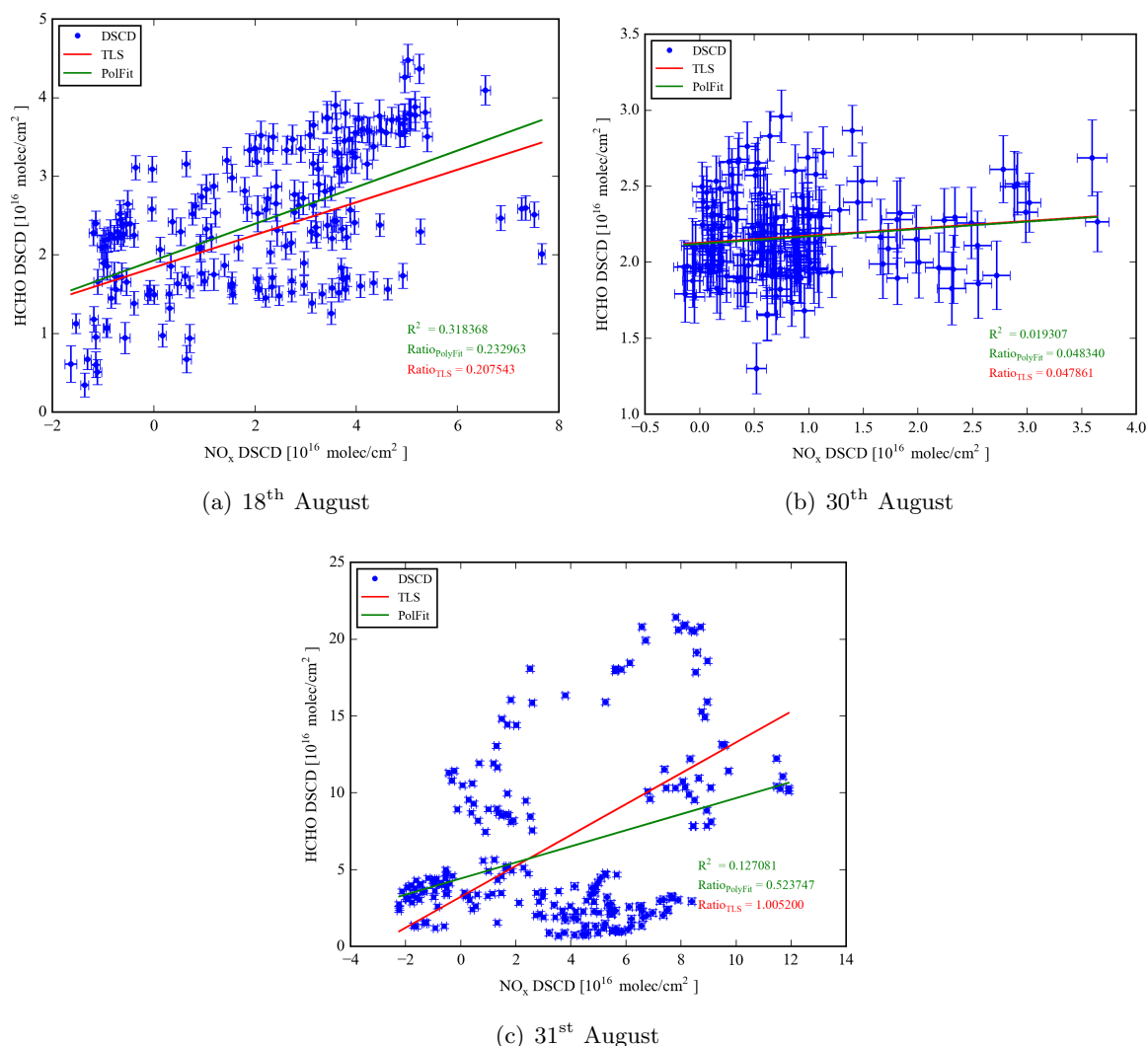
(c) 31st August

Figure 6.22.: HCHO-DSCDs plotted against NO_x-DSCDs for (a) 18th August, (b) 30th August and (c) 31st August 2015 . The regression results are represented by the green and red line, respectively. The emission ratios for the two approaches are indicated by the respective colour.

7. Conclusion

During this Master-Thesis project mobile MAX-DOAS measurements were performed in the Frankfurt/Rhein-Main area in winter 2015/spring 2016 and in Romania in summer 2015. The focus of this thesis was on the tropospheric formaldehyde column.

Two instruments were used for the measurements but we concentrate on the new and better TubeMAX-DOAS instrument. First, the instrumental setup was explained and some basic properties of the measuring system were characterised, namely the offset, the dark current, the detector linearity and the detector noise. Here the most important finding was that the detector exhibits a non linear response to the incident photons. This effect was found to be in the order of 5% which can systematically influence the spectral analysis of the recorded spectra of scattered sun light. Therefore, a correction method based on the findings of Horbanski (2015) was developed and applied.

Then the settings for the spectral analysis were presented and some sensitivity tests were performed. Here it was found that for our observations the used fit interval provides more stable results as the fit interval suggested from Pinardi et al. (2013). However, for other applications the latter interval might be more suited. Small changes in the edges of the fitting interval had only a small effect on the obtained DSCDs as well as on the RMS of the fit. The influence of an supposed additional O_4 absorption band at around $328.2\,\mathrm{nm}$ was also investigated. If such an band is included in the DOAS fit slightly lower DSCDs and RMS values are obtained. However, currently no appropriate literature O_4 cross-sections are available to take this absorption band into account in a proper way. Therefore, in the remaining part of the work this absorption was not accounted for. Finally, the fit results for both used instruments were compared. It was found that the residual of the new TubeMAX-DOAS instrument is one order of magnitude lower than the one for the commercial MiniMAX-DOAS system. Also the noise overlaying the spectral fit is much smaller for the new instrument.

In the main part of the work the results for the measurements in the Frankfurt/Rhein-Main area were investigated in detail. Here first the spatial distribution of HCHO around the three major measurement sites (Mainz, Frankfurt/Main and the Frankfurt Airport) was presented. For Mainz clear spatial patterns could be identified for most of the measurement days. Those patterns mostly show a pronounced outflow region, while also elevated HCHO-DSCDs could be observed in the city centre, where most of the traffic is located. Around Frankfurt more complex patterns were found. Here the spatial distributions of the airport and the city of Frankfurt might overlap. However, for selected cases also clear outflow patterns could be observed for both the airport and the city. These findings indicate that the HCHO distribution is highly influenced by traffic emissions.

Next the spatial HCHO distribution was correlated to the NO_2 distribution. For Mainz a

tight relation between both trace gases could be observed. Here high HCHO-DSCDs coincided with high NO$_2$-DSCDs. This finding is also very pronounced in the city centre. For the measurements around Frankfurt on nearly all days clear outflow patterns could be observed for NO$_2$, while the HCHO patterns showed more variations. Nevertheless, the spatial distributions of both trace gases still showed many similarities. Also around the Frankfurt airport both distributions are quite consistent and correspond to the prevailing wind pattern. However, both patterns seem to be slightly shifted against each other. This might indicate contributions from different sources for both trace gases.

Overall this close relationship between HCHO and NO$_2$ suggests that the measured HCHO mostly originates from traffic emissions. This finding is quite reasonable as the measurements were performed in the winter period of the year where both biogenic and photochemical activity is low. However, in future better wind data is needed in order to further investigate the influence of the airport.

From the retrieved HCHO and NO$_2$ data emission ratios (HCHO/NO$_x$) were calculated following the procedure from Klemp et al. (2002). After a presentation of daily ratios, mean emission ratios were calculated for four different approaches. Here values of 0.060, 0.060, 0.059 and 0.069 were obtained. Within the given uncertainties (0.036, 0.035, 0.031 and 0.034) all four ratios are consistent. Nevertheless, latter approach exhibits a larger discrepancy which is most likely related to the error assumption. Klemp et al. (2002) obtained emission ratios in a range from 0.029 to 0.037 which are lower. However, this systematic difference seems to be reasonable as we used MAX-DOAS measurements which average the trace gas concentrations over a certain altitude range and the different trace gases exhibit different vertical profiles. We also took all measurements into account, while Klemp et al. (2002) used an in-situ instrument only in the outflow of Augsburg and applied a more sophisticated data selection. Accounting for all these differences we find quite reasonable results compared with Klemp et al. (2002) and Slemr et al. (1996) who obtained an emission ratio of 0.050 which is also higher than the value of Klemp et al. (2002).

Finally, the results from the Rhein-Main measurements were compared to the Bucharest data. Also here the spatial patterns of both trace gases exhibit more or less clear outflow patterns. However, the spatial distributions of HCHO and NO$_2$ seem to be more shifted against each other. In addition, higher DSCDs were found for Bucharest which is reasonable as these measurements were performed during summer where the HCHO signal is expected to be higher. Also emission ratios were calculated for the three measurement days around Bucharest. However, no consistent values could be identified. These findings indicate the influence of secondary produced formaldehyde from both anthropogenic and biogenic sources.

For the future modifications on the instrumental setup and the measurement script are planned in order to improve the quality of the measurements and the stability of the instrument. Also further measurements during summer are planned in the Frankfurt/Rhein-Main area to capture the yearly cycle of the HCHO-DSCDs (and NO$_2$-DSCDs) and to have data which is more suited to be compared to the Bucharest data. In addition, also improvements on the data analysis have to be done. Higher resolved wind data is needed in order to investigate the special influence of the Frankfurt airport on the trace gas distribution. Additionally, a

more sophisticated error assessment is needed in order to improve the quality of the obtained emission ratios. Finally, the measurements also should be compared to model simulations in future.

A. Overview on all Measurement Days

A.1. Angles and Filter Settings for all Measurement Days

The following table provides an overview on the used elevation angles and O_4 filters for the different measurement days in the Frankfurt/Rhein-Main area:

Date	Elevation Angle [°]	O_4 filter [molec/cm^2]
12.10.2015	22	$1.65 \cdot 10^{43}$
13.10.2015	22	$1.20 \cdot 10^{43}$
27.10.2015	22	$1.10 \cdot 10^{43}$
29.10.2015	22	$1.00 \cdot 10^{43}$
30.10.2015	22	$1.50 \cdot 10^{43}$
05.11.2015	15	$2.10 \cdot 10^{43}$
11.11.2015	22	$1.60 \cdot 10^{43}$
23.11.2015	15	$2.10 \cdot 10^{43}$
20.12.2015	15	$2.25 \cdot 10^{43}$
08.01.2016	15	$3.10 \cdot 10^{43}$
21.01.2016	15	$1.70 \cdot 10^{43}$
22.01.2016	15	$1.80 \cdot 10^{43}$
29.01.2016	15	$2.50 \cdot 10^{43}$
03.02.2016	15	$2.30 \cdot 10^{43}$
17.02.2016	15	$2.20 \cdot 10^{43}$
25.02.2016	15	$2.50 \cdot 10^{43}$
14.03.2016	15	$2.25 \cdot 10^{43}$
17.03.2016	15	$2.25 \cdot 10^{43}$

Table A.1.: Table summarising the measurement settings for the respective measurement days. The column "Elevation Angle" simply indicates the low elevation angle, as 90° spectra were recorded on all days.

A.2. Distribution of HCHO and NO$_2$ for all Measurement Days

The following pages show the distribution of HCHO (upper panel) and NO$_2$ (lower panel) for all measurements which were performed in the Frankfurt/Rhein-Main area during this work. In addition, the wind barbs indicate the prevailing wind direction in terms of the ECMWF 12 UTC wind re-analysis data (see section 6.3).

A.2.1. Mainz

(a) 09:00 to 10:20 UTC

(b) 12:57 to 14:30 UTC
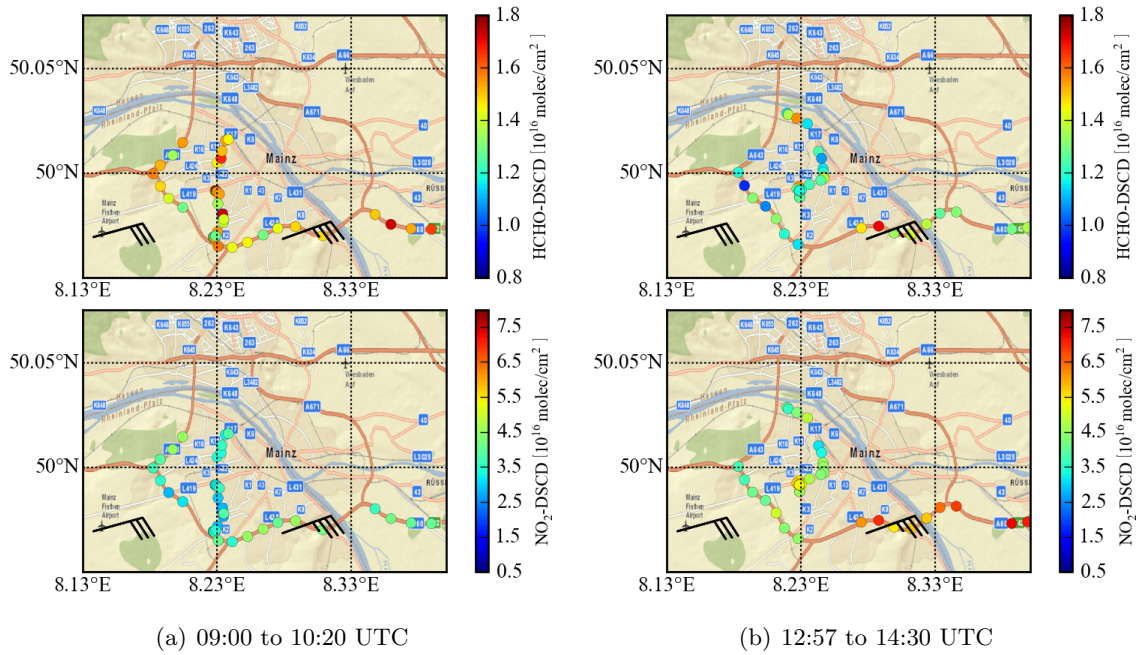
Figure A.1.: Spatial distribution of the HCHO (upper panel) and NO$_2$ (lower panel) DSCDs around Mainz on 12th October 2015.

(a) 08:00 to 08:54 UTC

(b) 11:03 to 12:30 UTC
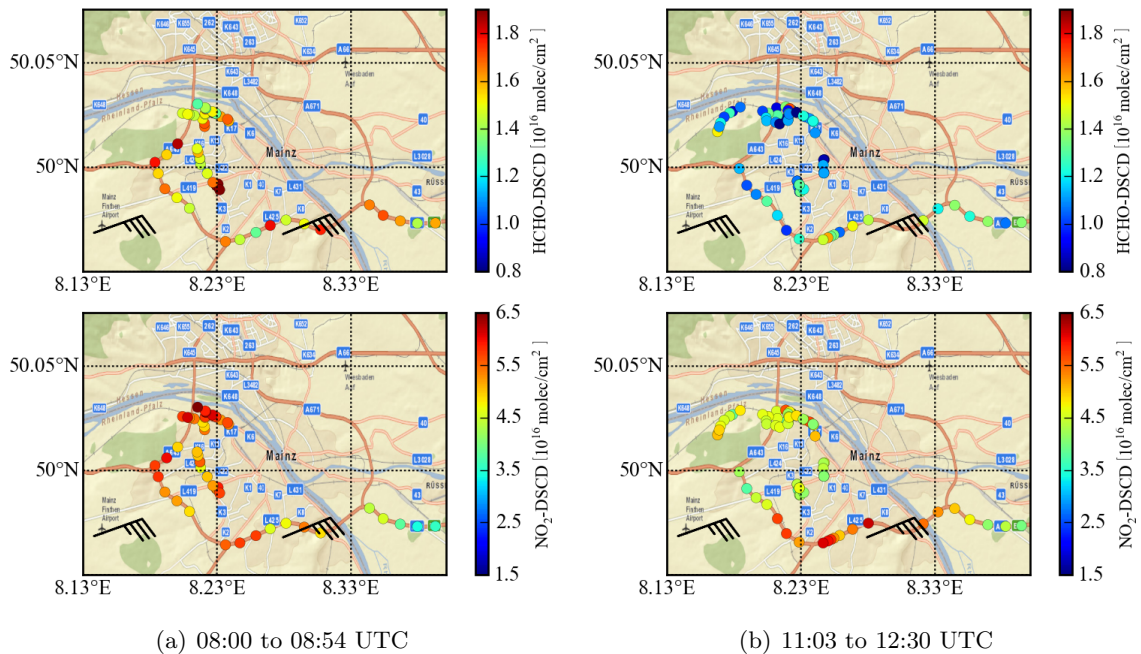
Figure A.2.: Spatial distribution of the HCHO (upper panel) and NO$_2$ (lower panel) DSCDs around Mainz on 13th October 2015.
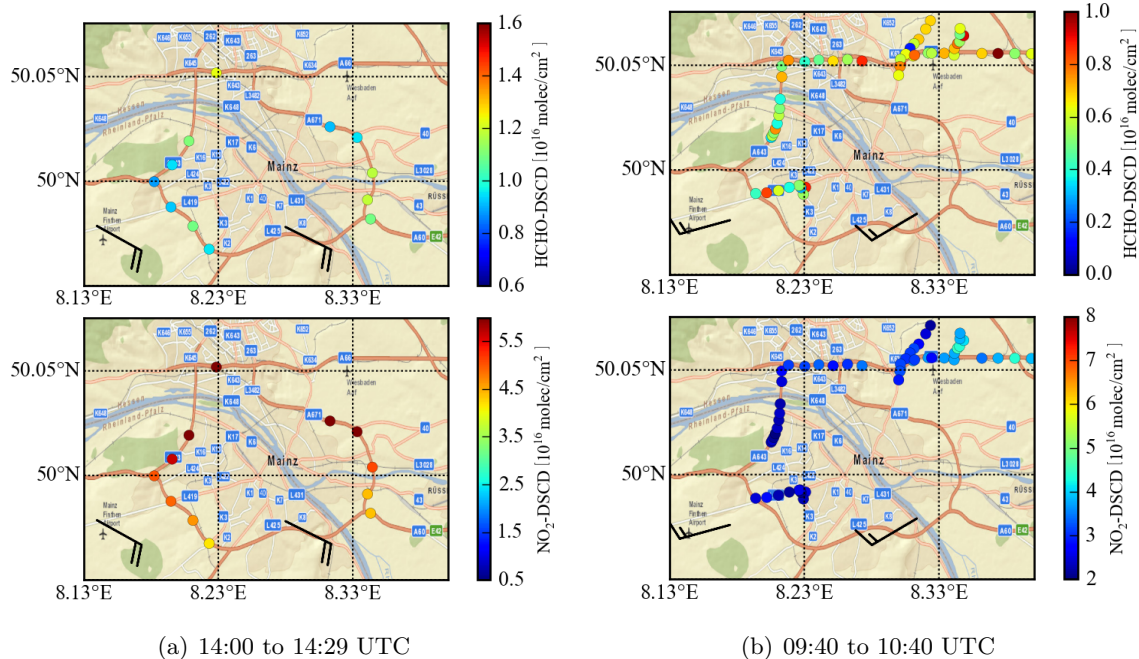
Figure A.3.: Spatial distribution of the HCHO (upper panel) and NO$_2$ (lower panel) DSCDs around Mainz on 27th (a) and 29th (b) October 2015.
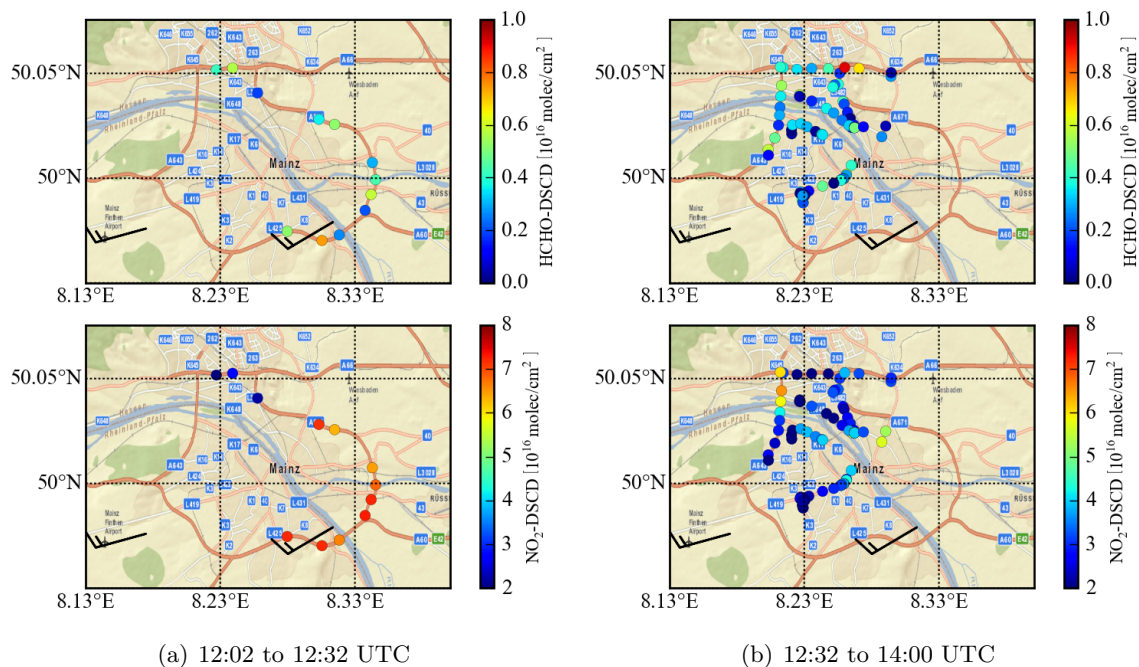
Figure A.4.: Spatial distribution of the HCHO (upper panel) and NO$_2$ (lower panel) DSCDs around Mainz on 29th October 2015.

(a) 09:45 to 10:23 UTC

(b) 10:23 to 11:24 UTC
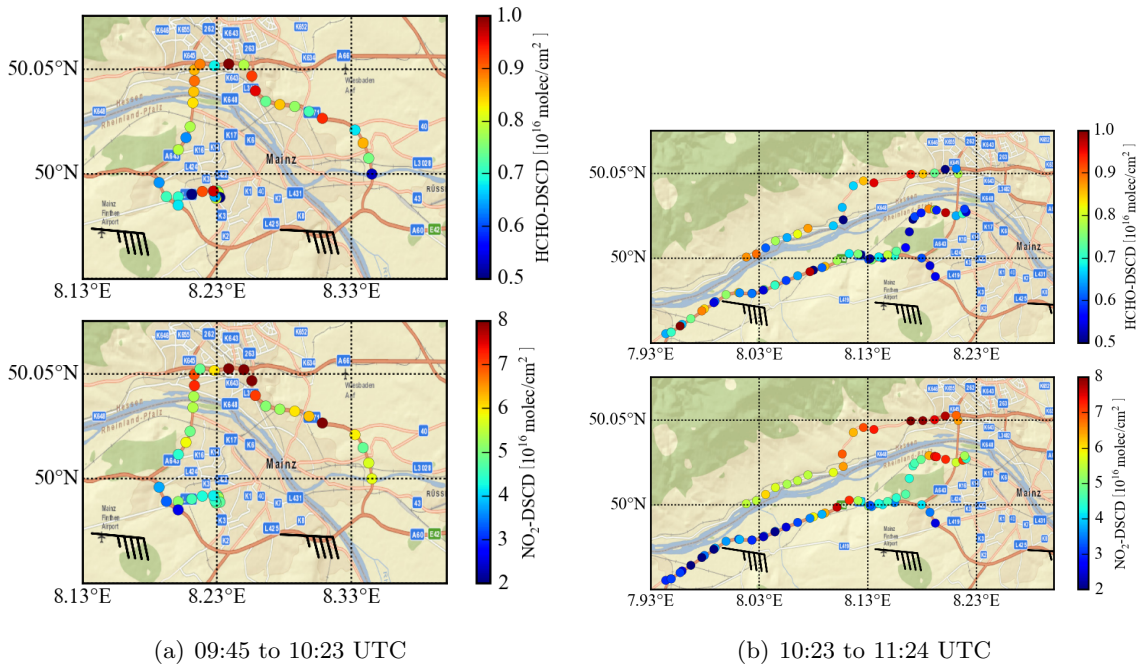
Figure A.5.: Spatial distribution of the HCHO (upper panel) and NO$_2$ (lower panel) DSCDs around Mainz on 30$^{\text{th}}$ October 2015.

(a) 11:24 to 13:00 UTC

(b) 10:00 to 11:10 UTC
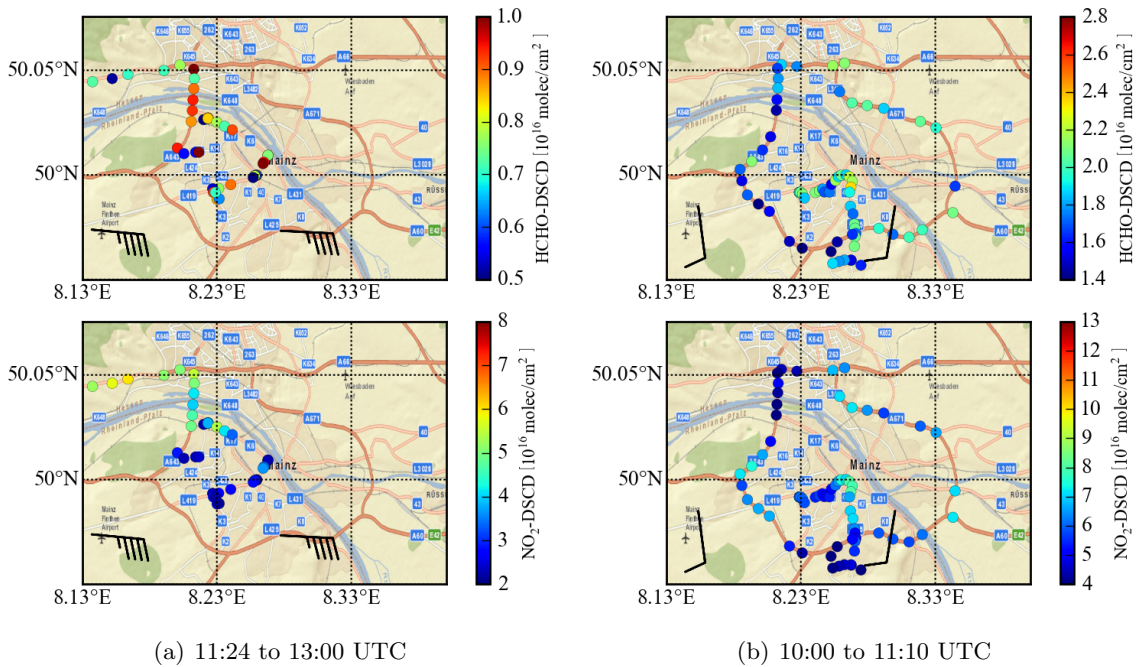
Figure A.6.: Spatial distribution of the HCHO (upper panel) and NO$_2$ (lower panel) DSCDs around Mainz on 30$^{\text{th}}$ October (a) and 05$^{\text{th}}$ November 2015 (b).

(a) 11:10 to 13:00 UTC

(b) 13:00 to 14:00 UTC
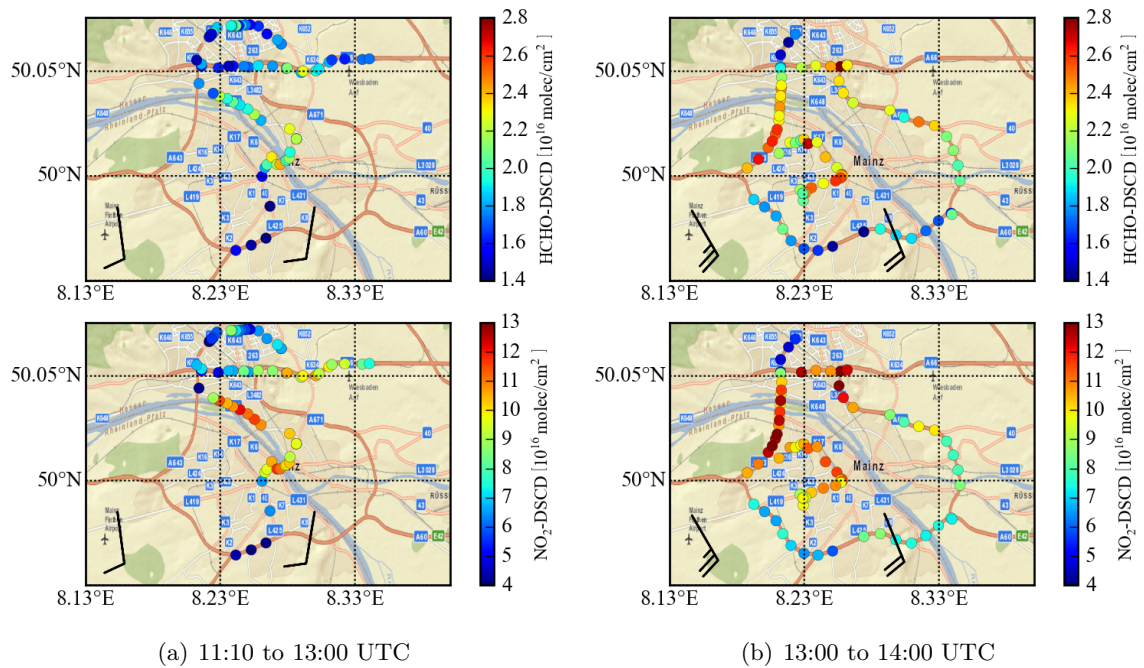
Figure A.7.: Spatial distribution of the HCHO (upper panel) and NO$_2$ (lower panel) DSCDs around Mainz on 05th November 2015.

(a) 09:43 to 10:12 UTC

(b) 13:02 to 14:30 UTC
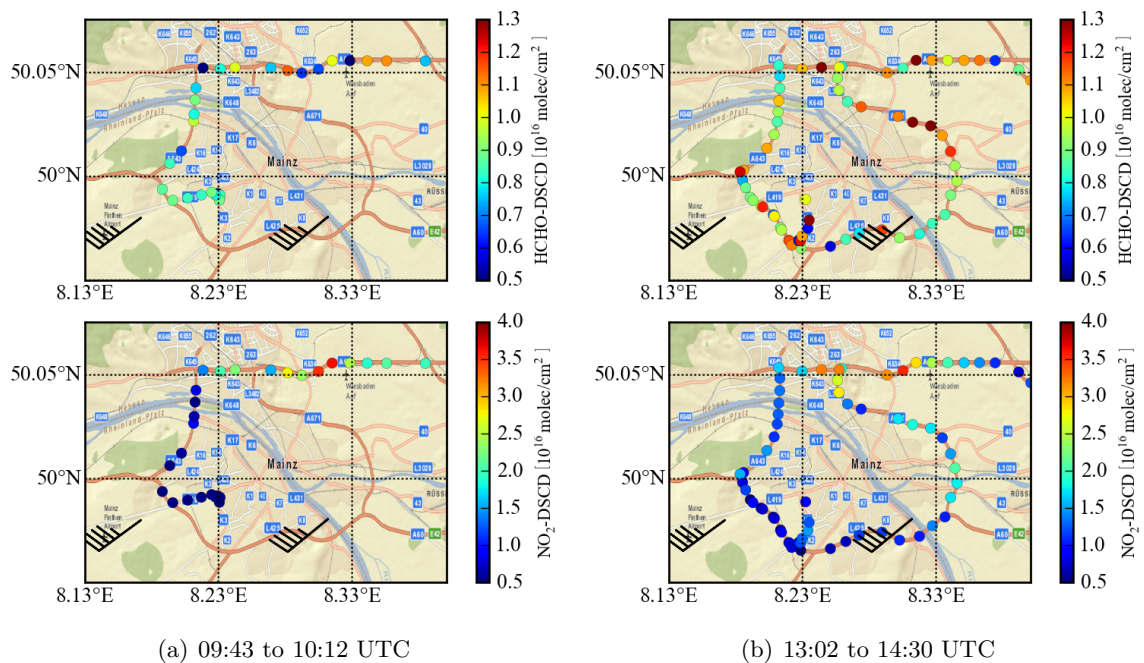
Figure A.8.: Spatial distribution of the HCHO (upper panel) and NO$_2$ (lower panel) DSCDs around Mainz on 11th November 2015.

(a) 11:00 to 12:00 UTC (b) 09:50 to 10:22 UTC
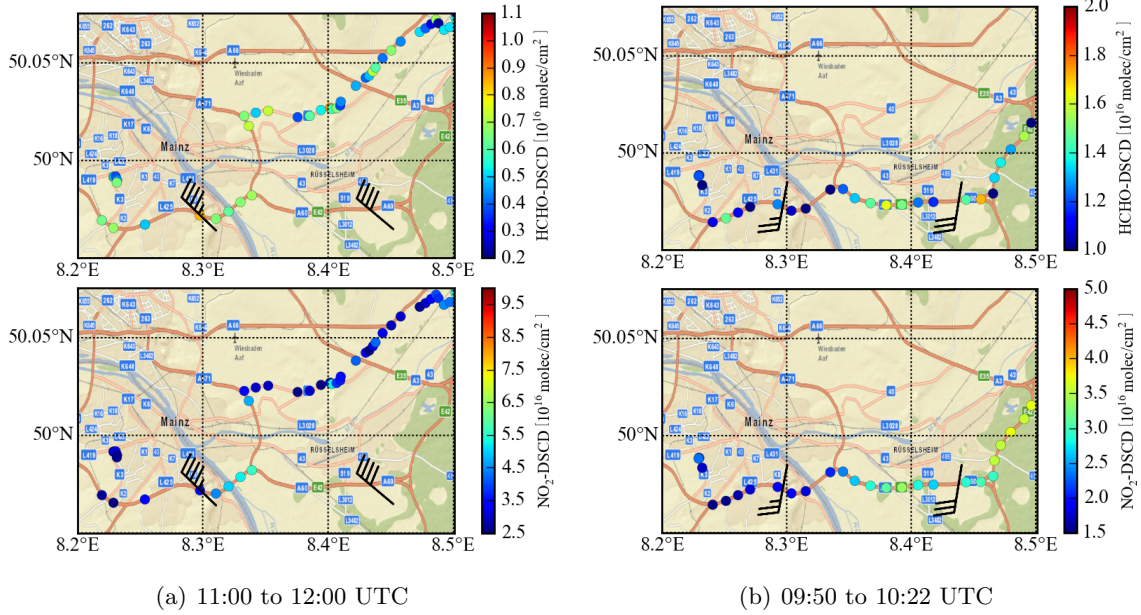
Figure A.9.: Spatial distribution of the HCHO (upper panel) and NO$_2$ (lower panel) DSCDs around Mainz on 23rd November 2015 (a) and 20th December 2015 (b).

(a) 12:43 to 13:16 UTC (b) 09:32 to 10:12 UTC
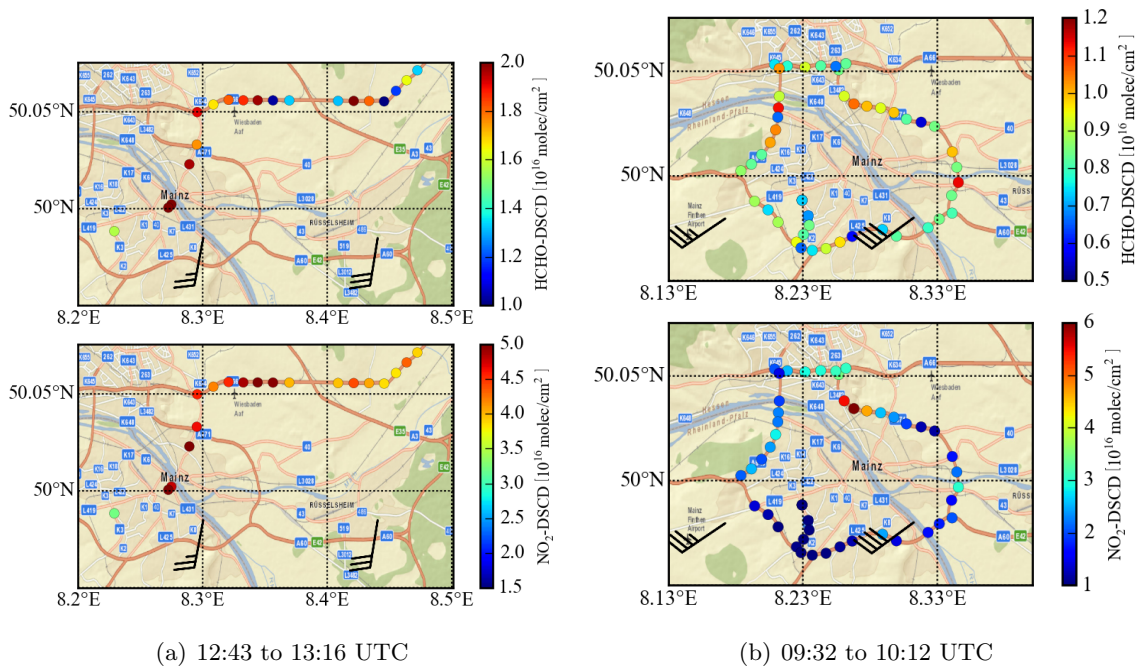
Figure A.10.: Spatial distribution of the HCHO (upper panel) and NO$_2$ (lower panel) DSCDs around Mainz on 20th December 2015 (a) and 08th January 2016 (b).

(a) 10:12 to 11:30 UTC

(b) 11:30 to 12:15 UTC
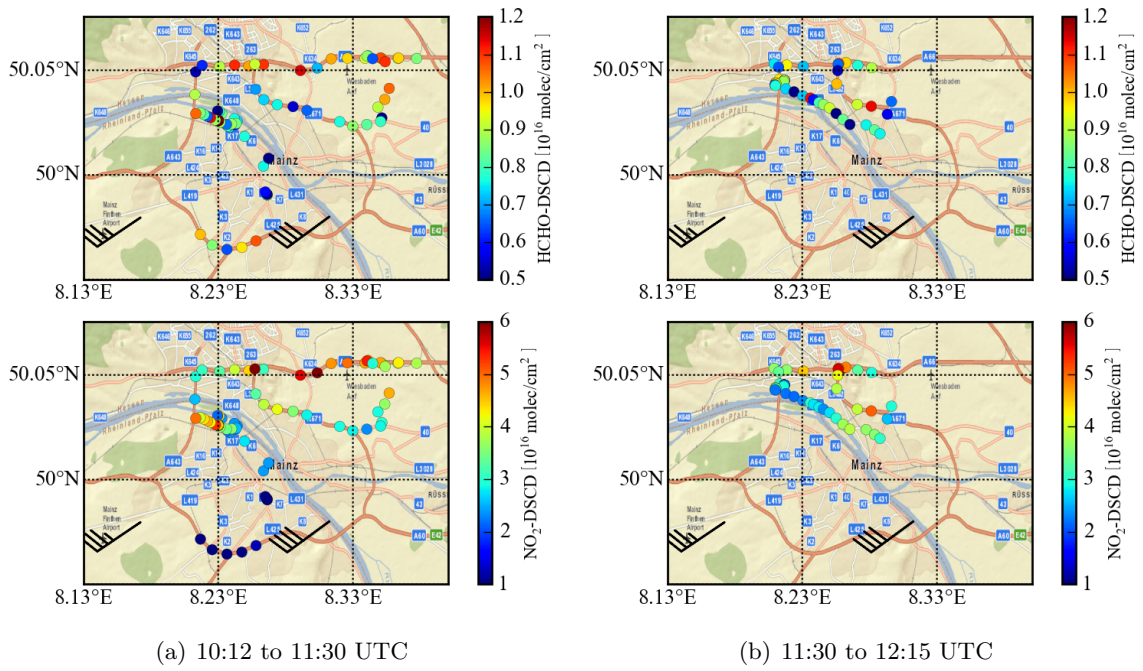
Figure A.11.: Spatial distribution of the HCHO (upper panel) and NO_2 (lower panel) DSCDs around Mainz on 08th January 2016.

(a) 12:15 to 12:56 UTC

(b) 12:56 to 14:00 UTC
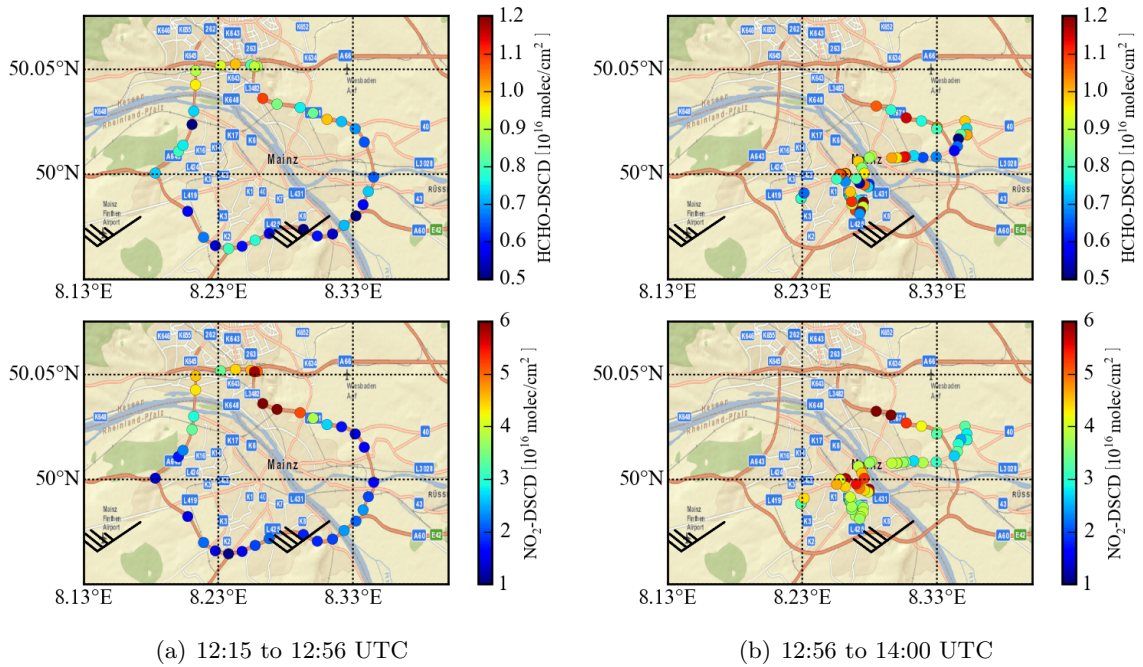
Figure A.12.: Spatial distribution of the HCHO (upper panel) and NO_2 (lower panel) DSCDs around Mainz on 08th January 2016.

(a) 10:26 to 11:50 UTC

(b) 11:50 to 12:49 UTC
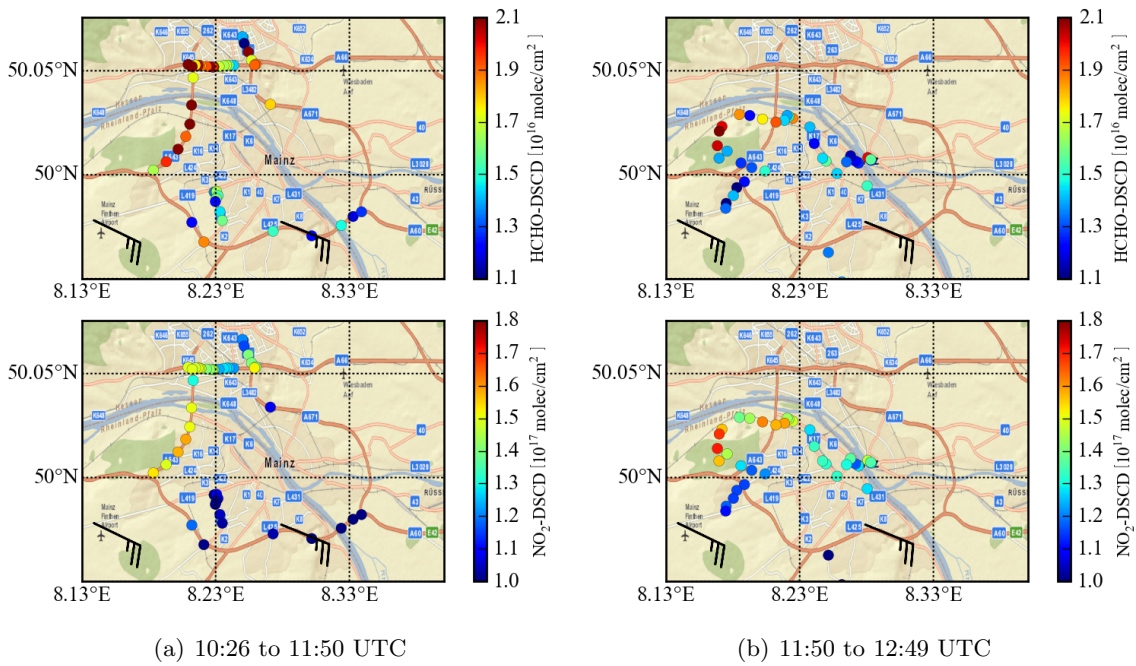
Figure A.13.: Spatial distribution of the HCHO (upper panel) and NO$_2$ (lower panel) DSCDs around Mainz on 21st January 2016.

(a) 12:49 to 13:40 UTC

(b) 09:53 to 10:30 UTC
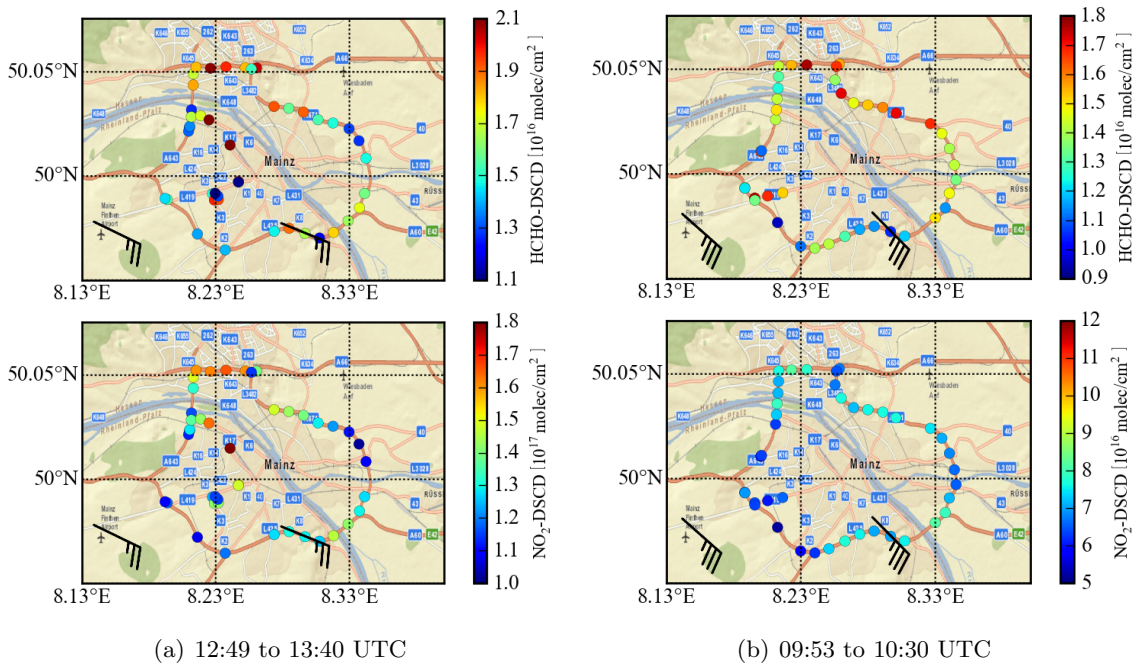
Figure A.14.: Spatial distribution of the HCHO (upper panel) and NO$_2$ (lower panel) DSCDs around Mainz on 21st January 2016 (a) and 22nd January 2016 (b).

(a) 10:30 to 10:53 UTC

(b) 12:47 to 13:23 UTC
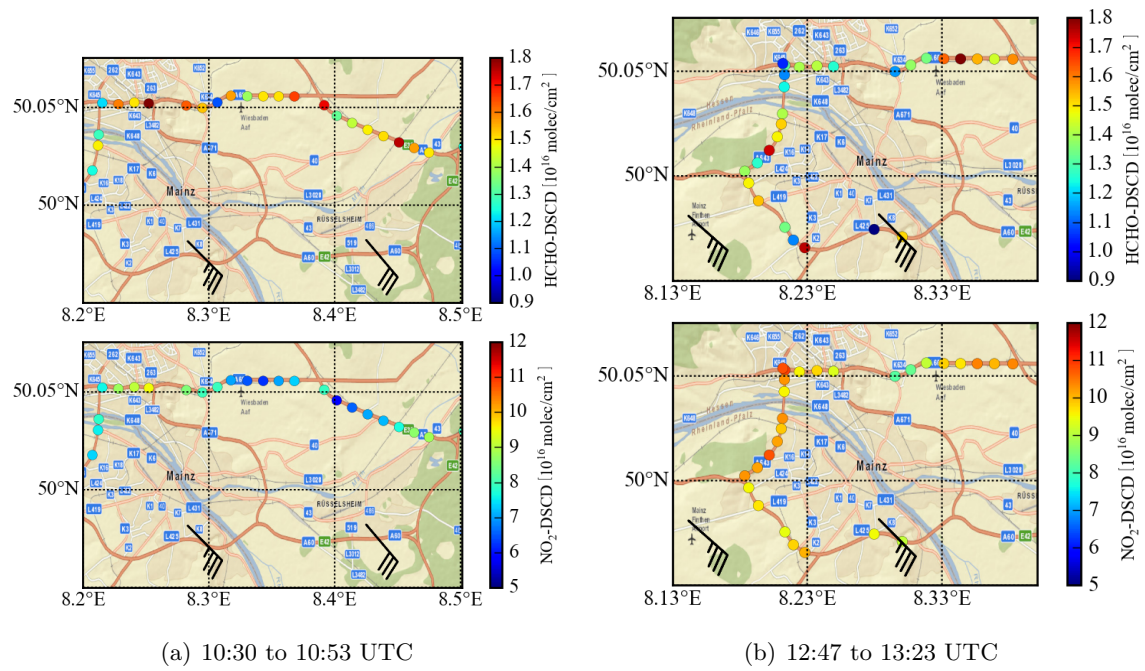
Figure A.15.: Spatial distribution of the HCHO (upper panel) and NO_2 (lower panel) DSCDs around Mainz on 22nd January 2016.

(a) 09:33 to 10:41 UTC

(b) 12:42 to 14:08 UTC
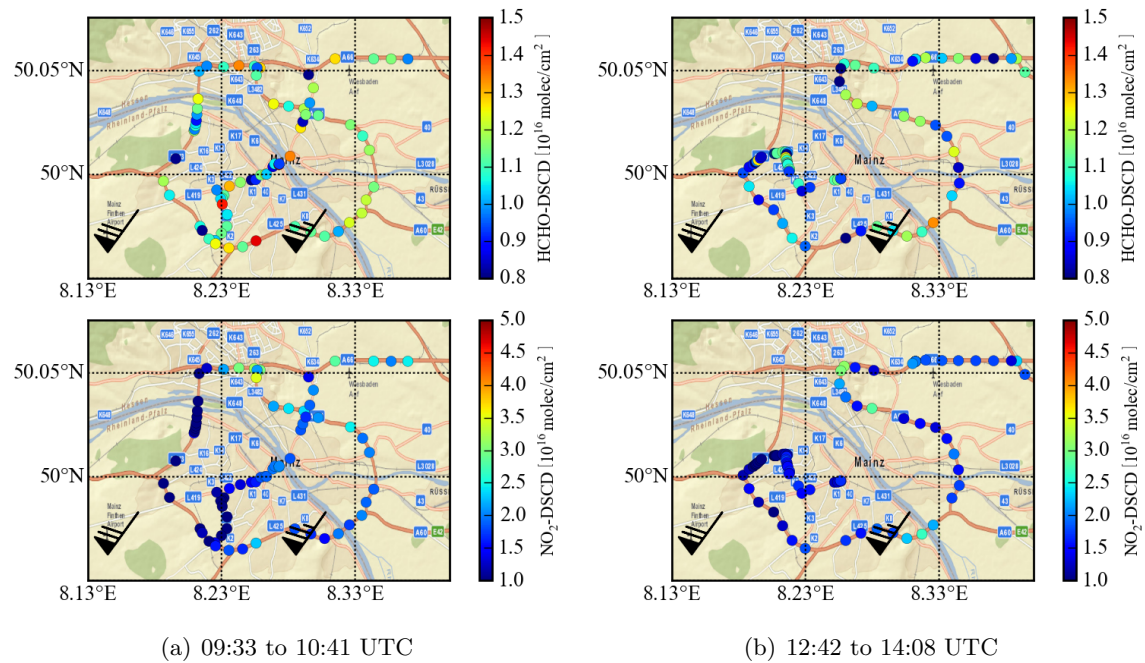
Figure A.16.: Spatial distribution of the HCHO (upper panel) and NO_2 (lower panel) DSCDs around Mainz on 29th January 2016.

(a) 09:38 to 10:08 UTC

(b) 11:39 to 12:50 UTC
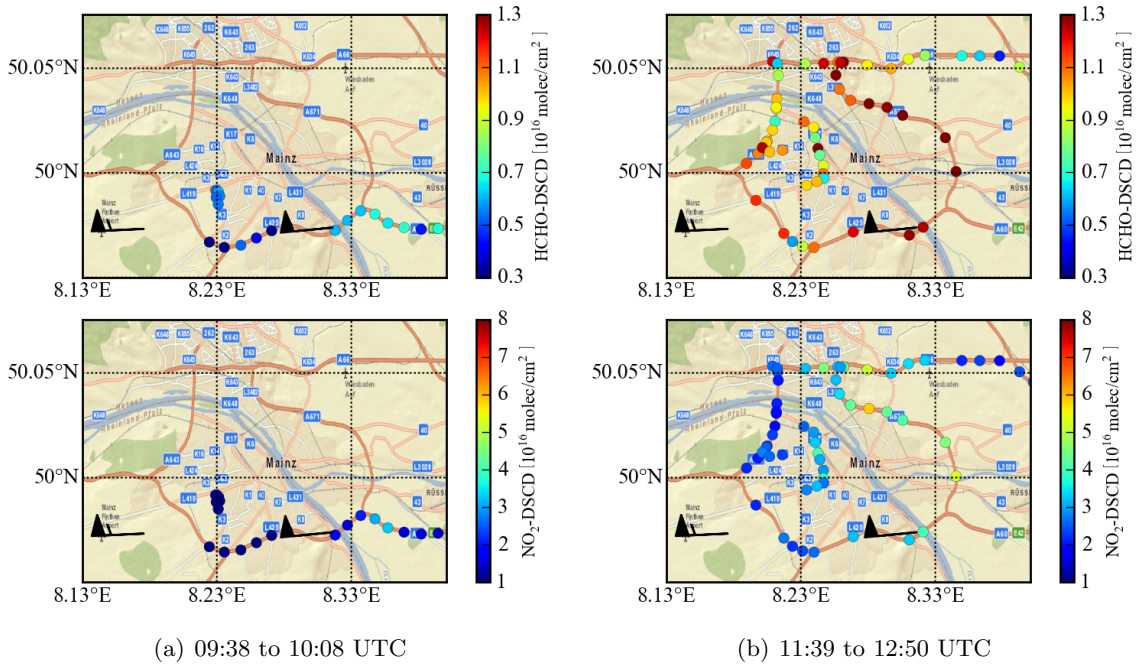
Figure A.17.: Spatial distribution of the HCHO (upper panel) and NO$_2$ (lower panel) DSCDs around Mainz on 03rd February 2016.

(a) 09:27 to 10:06 UTC

(b) 10:06 to 10:44 UTC
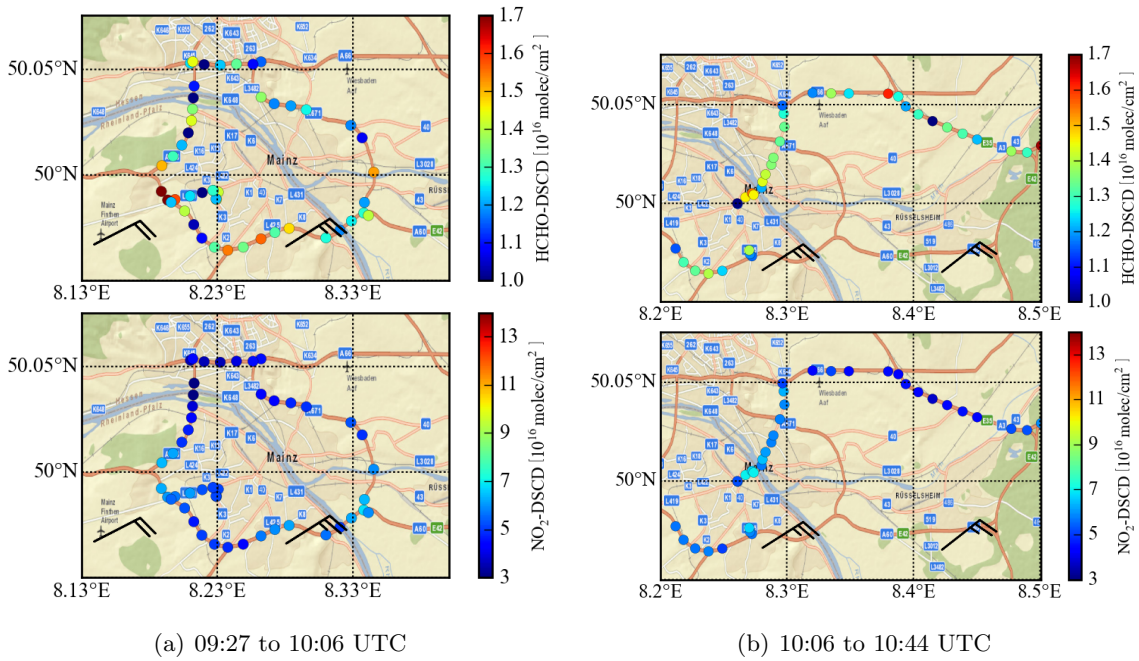
Figure A.18.: Spatial distribution of the HCHO (upper panel) and NO$_2$ (lower panel) DSCDs around Mainz on 17th February 2016.

(a) 13:27 to 14:31 UTC

(b) 09:12 to 10:04 UTC
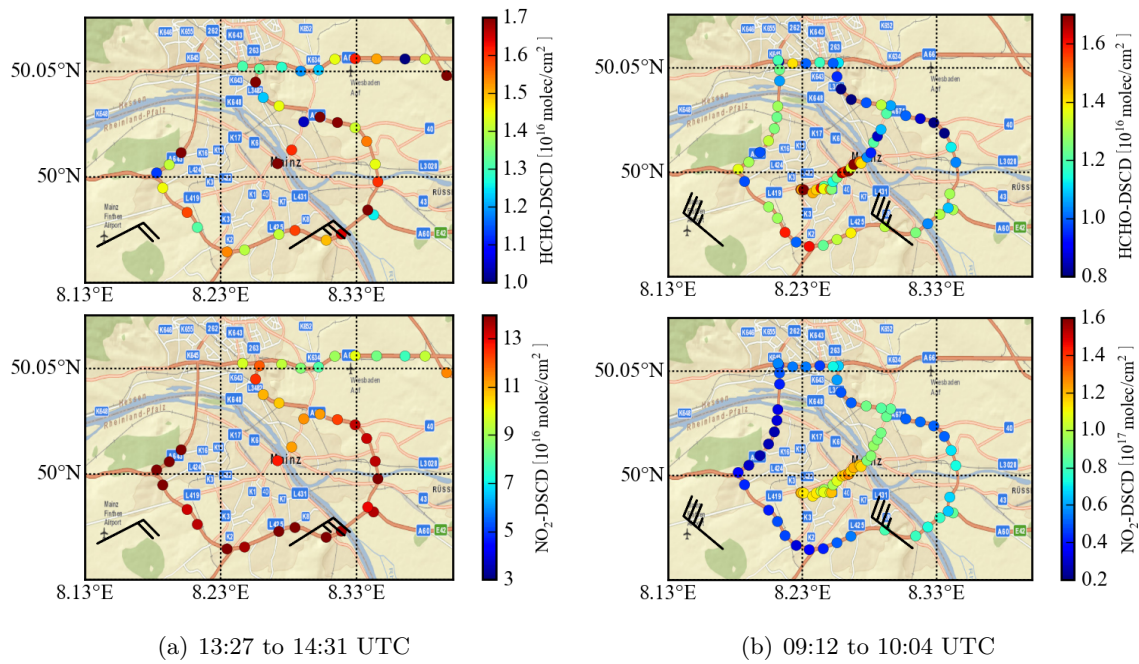
Figure A.19.: Spatial distribution of the HCHO (upper panel) and NO$_2$ (lower panel) DSCDs around Mainz on 17th February 2016 (a) and 25th February 2016 (b).

(a) 11:47 to 13:05 UTC

(b) 12:48 to 13:58 UTC
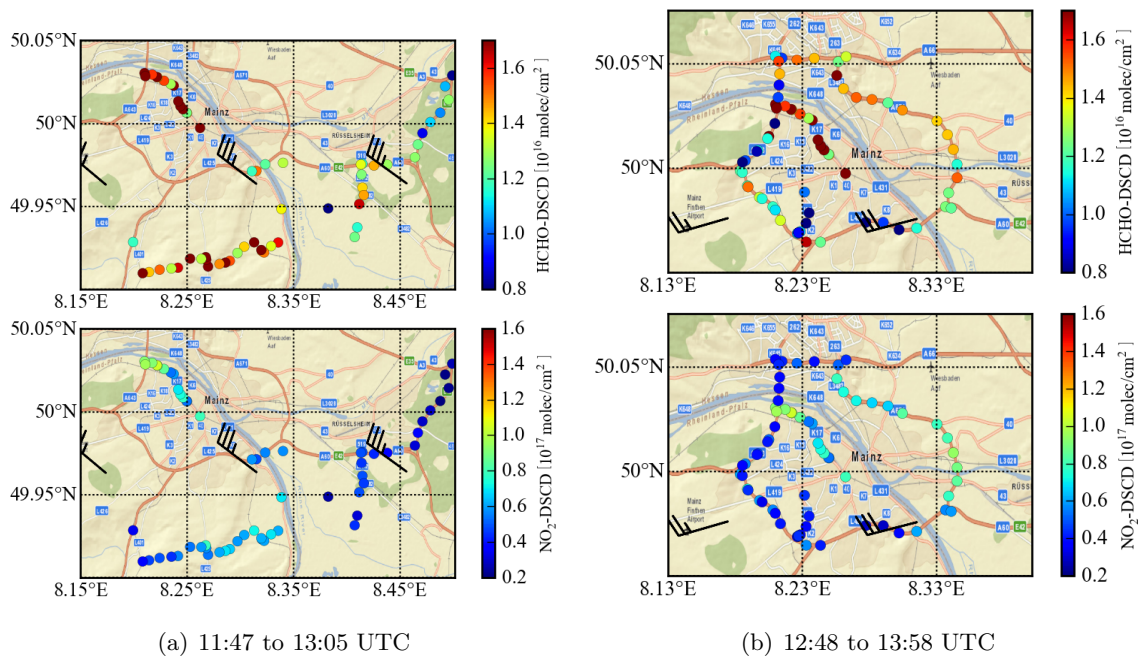
Figure A.20.: Spatial distribution of the HCHO (upper panel) and NO$_2$ (lower panel) DSCDs around Mainz on 25th February 2016.

(a) 09:30 to 10:32 UTC

(b) 14:06 to 14:56 UTC
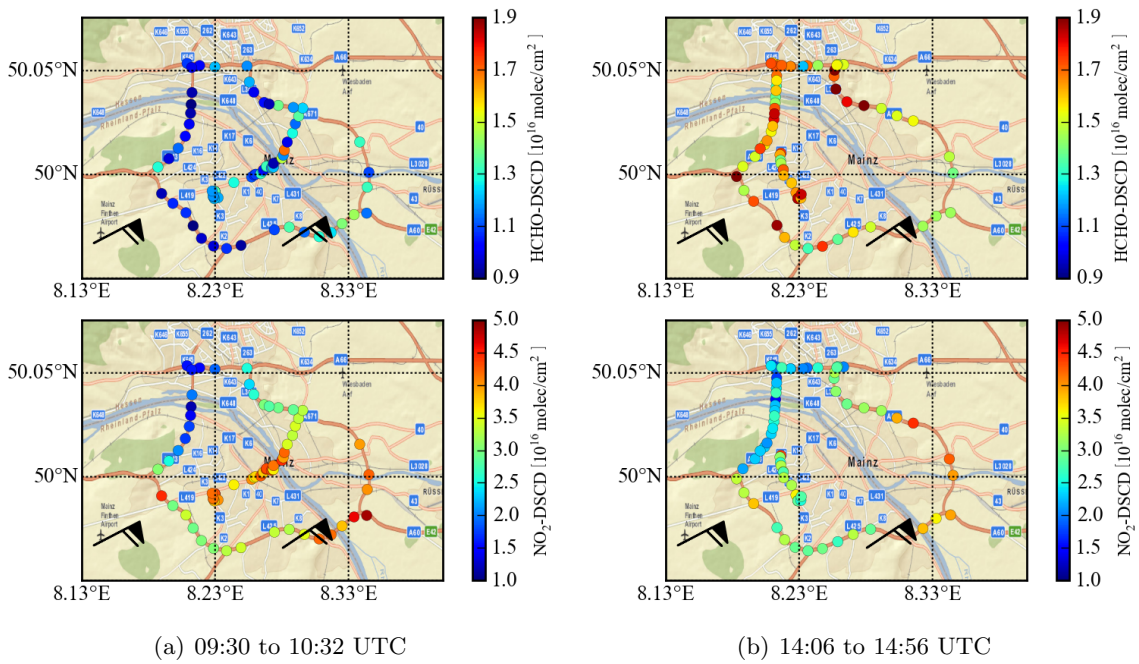
Figure A.21.: Spatial distribution of the HCHO (upper panel) and NO$_2$ (lower panel) DSCDs around Mainz on 14$^{\text{th}}$ March 2016.

(a) 09:35 to 10:25 UTC

(b) 13:49 to 14:57 UTC
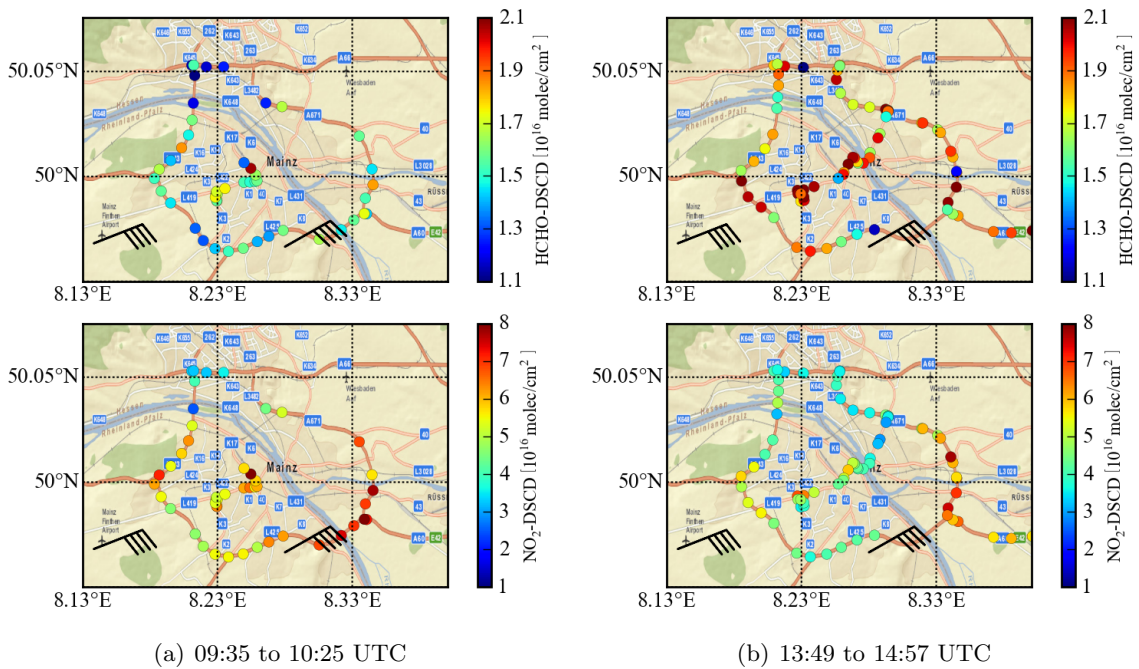
Figure A.22.: Spatial distribution of the HCHO (upper panel) and NO$_2$ (lower panel) DSCDs around Mainz on 17$^{\text{th}}$ March 2016.

A.2.2. Frankfurt

(a) 10:45 to 11:39 UTC

(b) 11:39 to 12:57 UTC
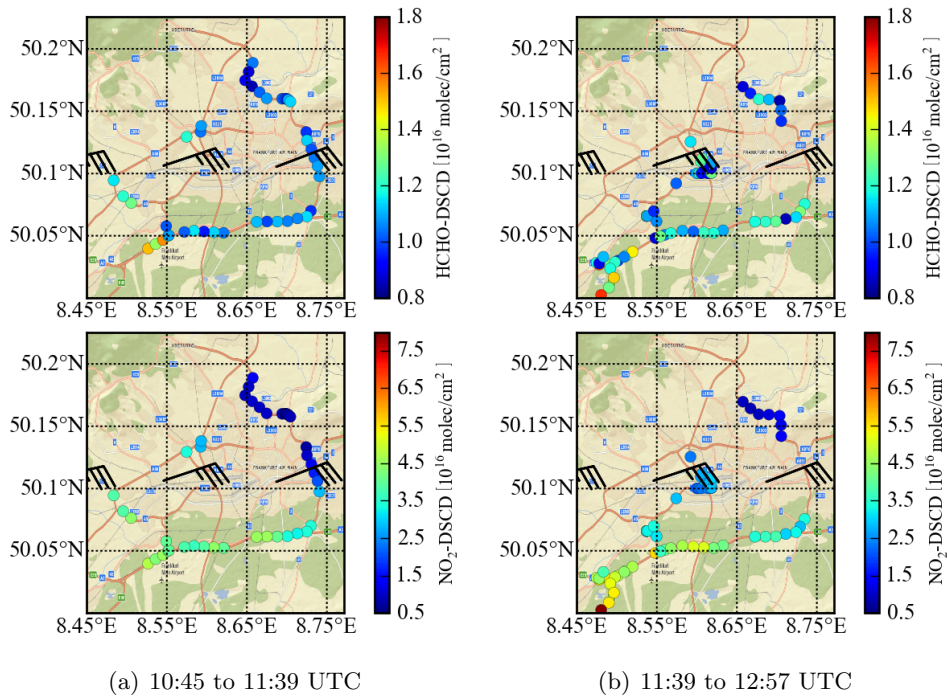
Figure A.23.: Spatial distribution of the HCHO (upper panel) and NO$_2$ (lower panel) DSCDs around Frankfurt on 12$^{\text{th}}$ October 2015.

(a) 08:54 to 09:52 UTC

(b) 09:52 to 10:30 UTC
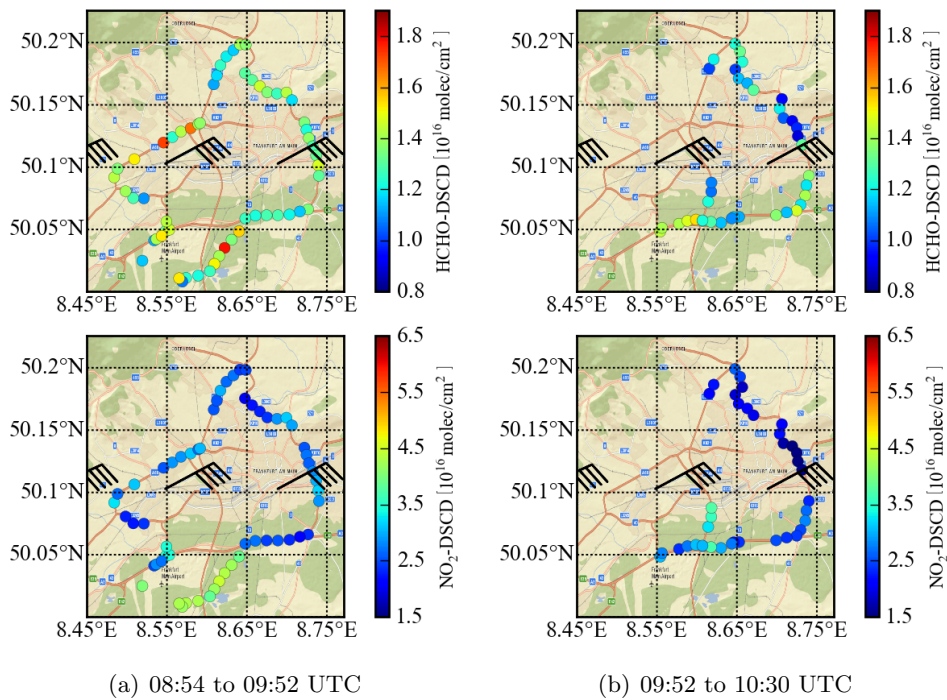
Figure A.24.: Spatial distribution of the HCHO (upper panel) and NO$_2$ (lower panel) DSCDs around Frankfurt on 13$^{\text{th}}$ October 2015.

(a) 09:32 to 10:43 UTC   (b) 10:43 to 12:27 UTC
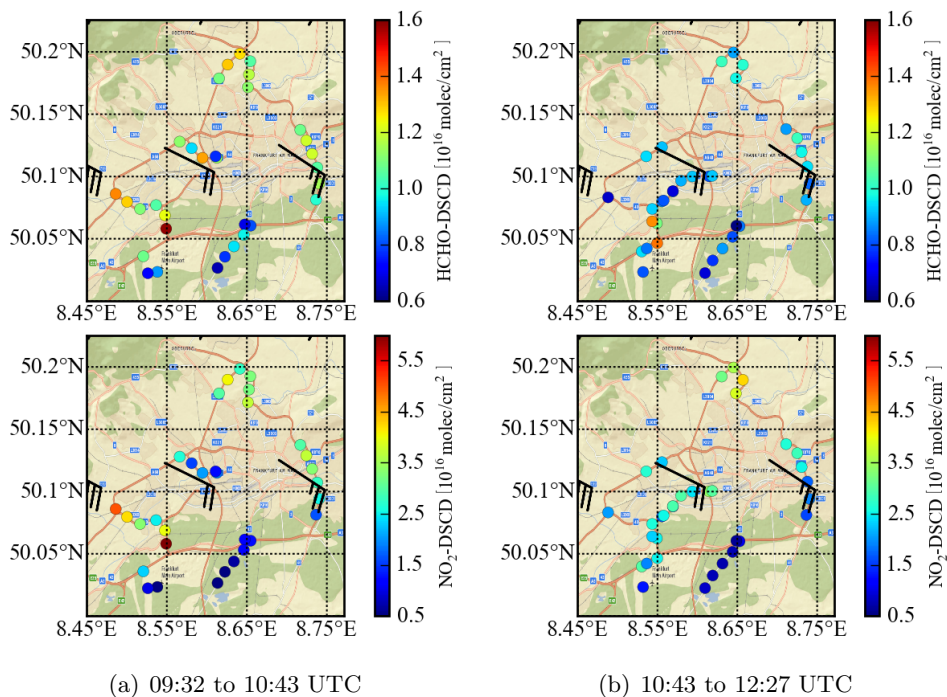
Figure A.25.: Spatial distribution of the HCHO (upper panel) and NO$_2$ (lower panel) DSCDs around Frankfurt on 27$^{\text{th}}$ October 2015.

(a) 12:27 to 13:40 UTC   (b) 10:40 to 11:49 UTC
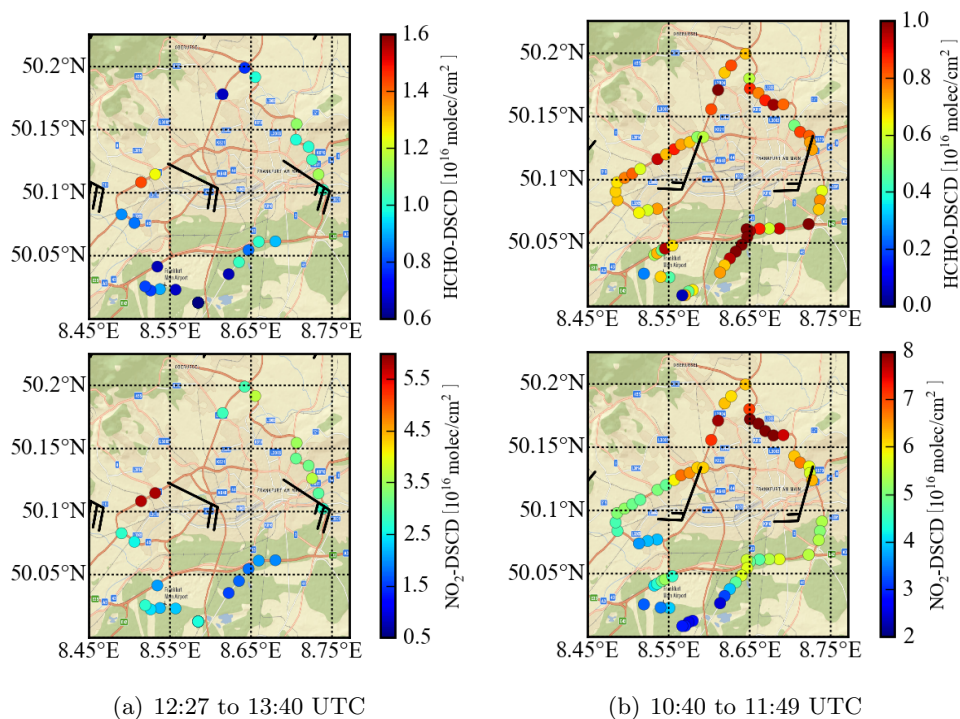
Figure A.26.: Spatial distribution of the HCHO (upper panel) and NO$_2$ (lower panel) DSCDs around Frankfurt on 27$^{\text{th}}$ (a) and 29$^{\text{th}}$ (b) October 2015.

(a) 10:12 to 11:00 UTC   (b) 11:46 to 12:31 UTC
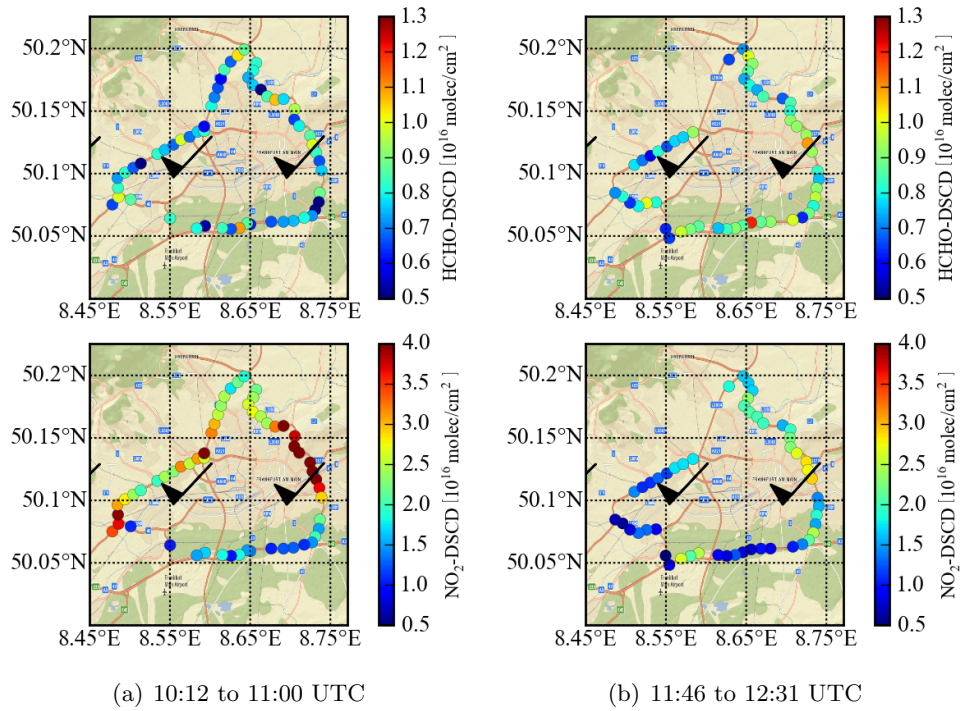
Figure A.27.: Spatial distribution of the HCHO (upper panel) and NO_2 (lower panel) DSCDs around Frankfurt on 11th November 2015.

(a) 11:50 to 12:47 UTC   (b) 10:22 to 11:10 UTC
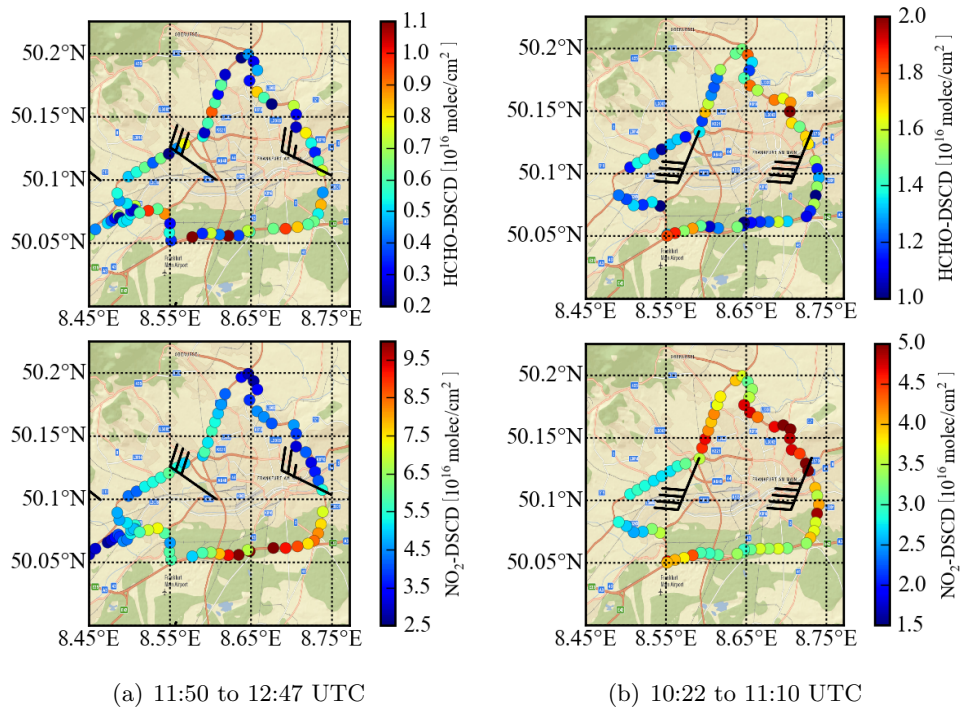
Figure A.28.: Spatial distribution of the HCHO (upper panel) and NO_2 (lower panel) DSCDs around Frankfurt on 11th November 2015 (a) and 20th December 2015 (b).

(a) 11:45 to 12:43 UTC   (b) 10:30 to 11:39 UTC
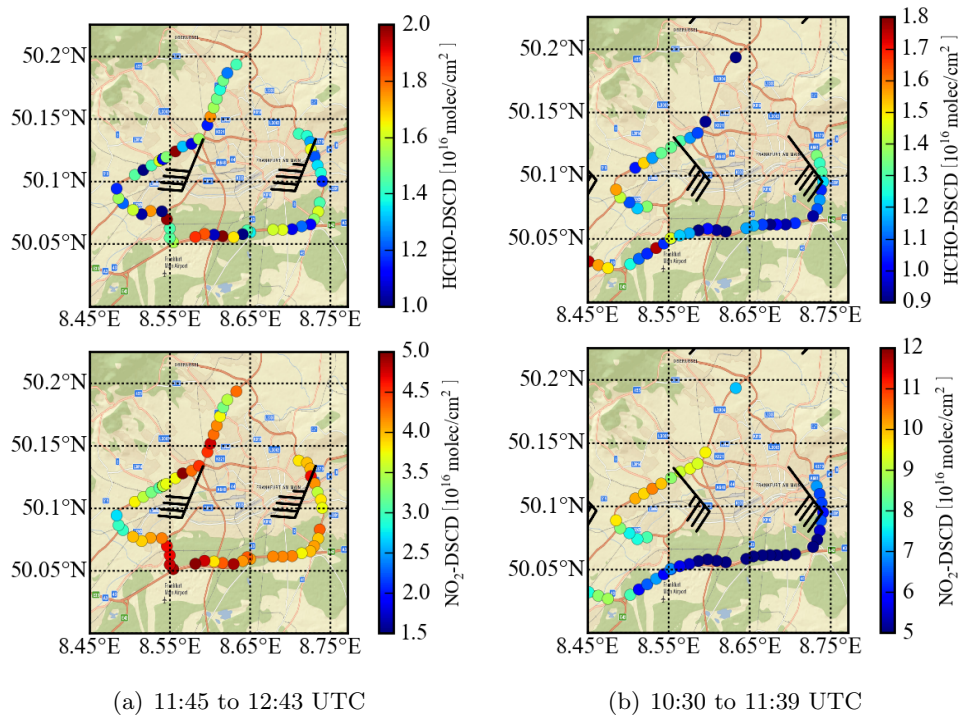
Figure A.29.: Spatial distribution of the HCHO (upper panel) and NO$_2$ (lower panel) DSCDs around Frankfurt on 20th December 2015 (a) and 22nd January 2016 (b).

(a) 10:08 to 10:55 UTC   (b) 11:22 to 12:08 UTC
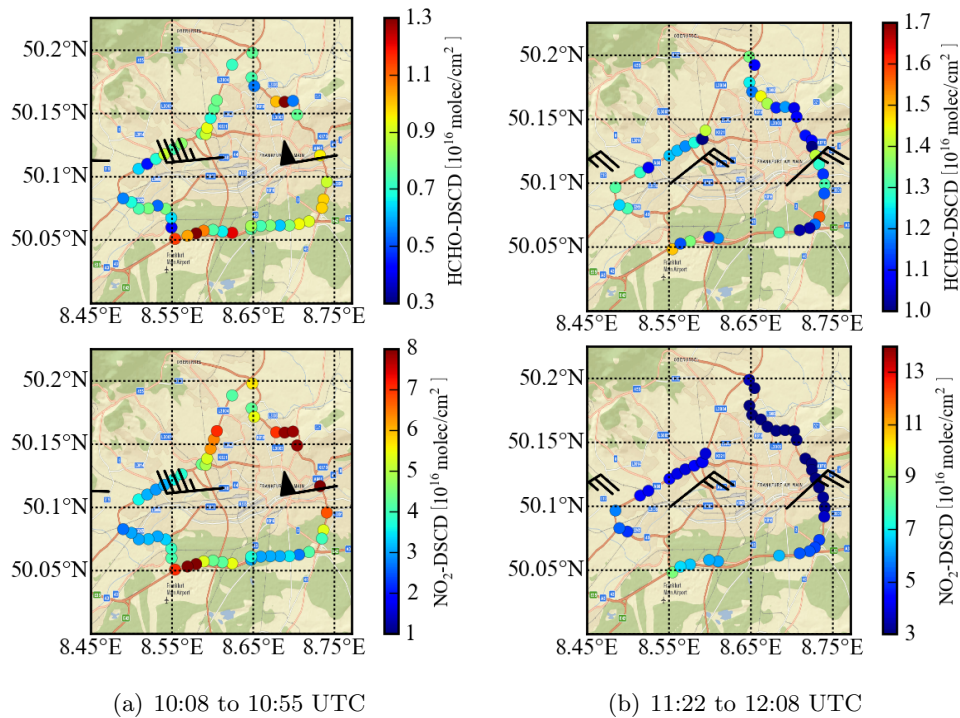
Figure A.30.: Spatial distribution of the HCHO (upper panel) and NO$_2$ (lower panel) DSCDs around Frankfurt on 03rd February 2016 (a) and 17th February 2016 (b).
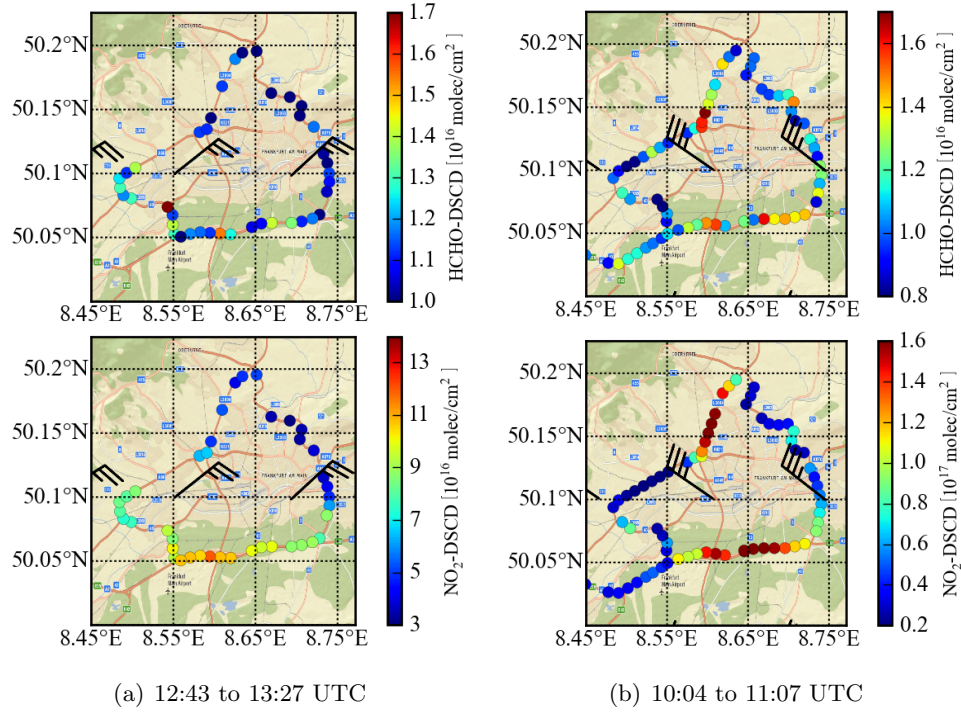
Figure A.31.: Spatial distribution of the HCHO (upper panel) and NO_2 (lower panel) DSCDs around Frankfurt on 17th (a) and 25th (b) February 2016.
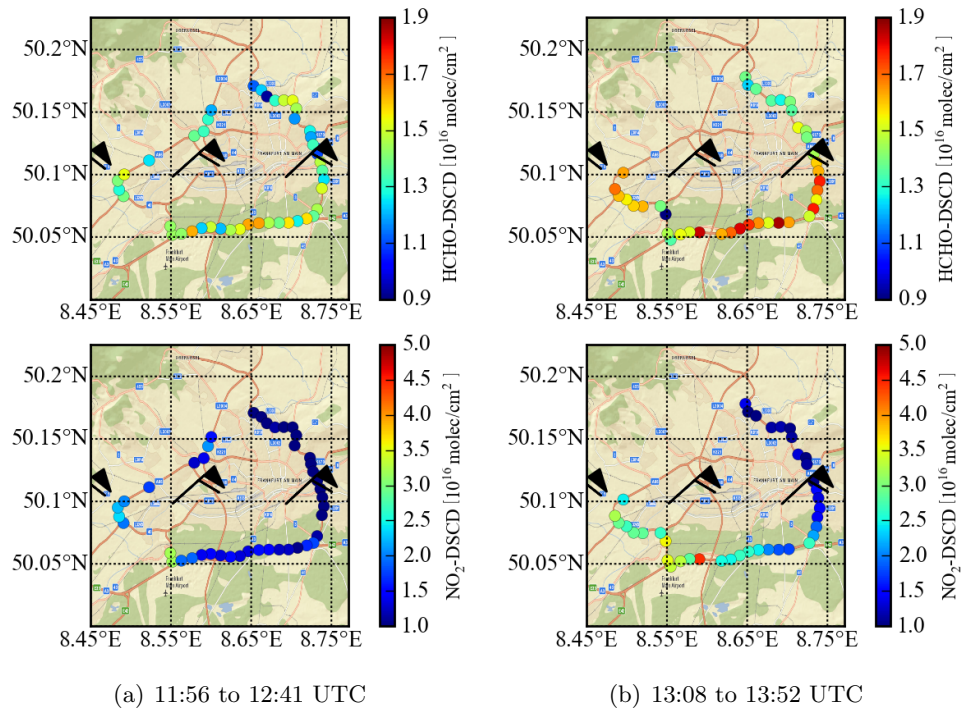
Figure A.32.: Spatial distribution of the HCHO (upper panel) and NO_2 (lower panel) DSCDs around Frankfurt on 14th March 2016.

(a) 10:25 to 11:39 UTC   (b) 13:05 to 13:49 UTC
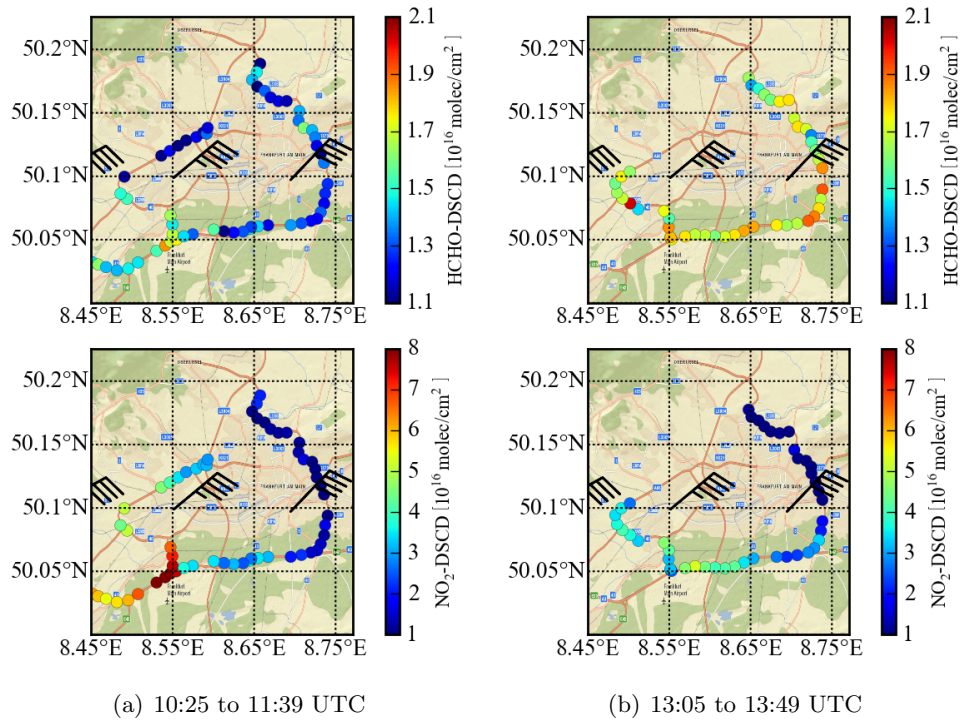
Figure A.33.: Spatial distribution of the HCHO (upper panel) and NO_2 (lower panel) DSCDs around Frankfurt on 17th March 2016.

A.2.3. Frankfurt Airport

(a) 10:10 to 10:45 UTC

(b) 10:30 to 11:03 UTC
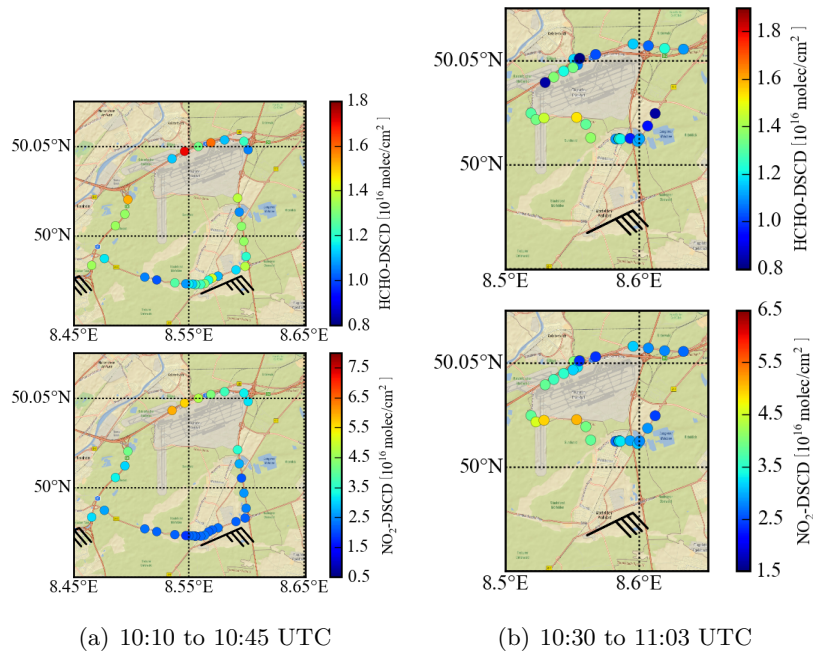
Figure A.34.: Spatial distribution of the HCHO (upper panel) and NO$_2$ (lower panel) DSCDs around the Frankfurt airport on 12th (a) and 13th (b) October 2015.

(a) 11:00 to 11:45 UTC

(b) 12:31 to 13:02 UTC
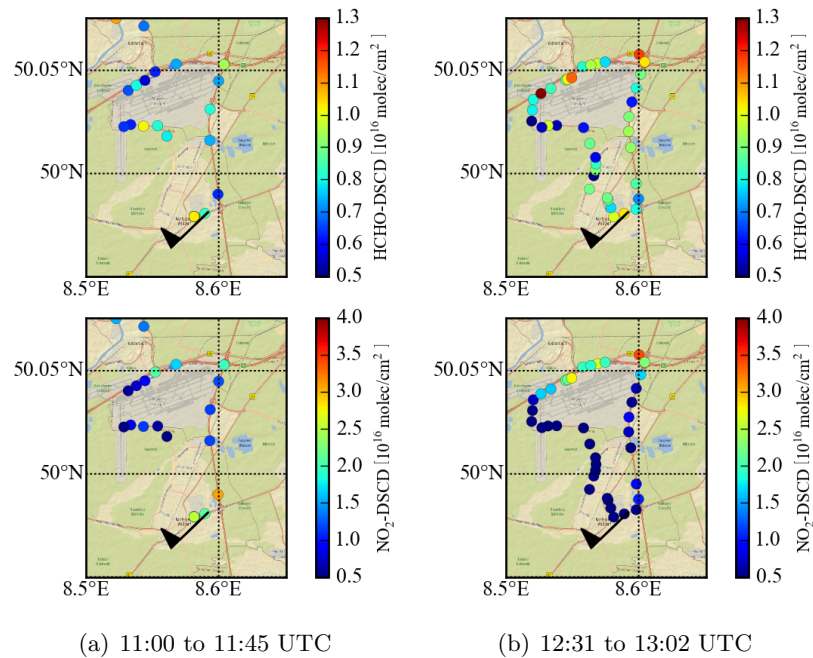
Figure A.35.: Spatial distribution of the HCHO (upper panel) and NO$_2$ (lower panel) DSCDs around the Frankfurt airport on 11th November 2015.

(a) 12:47 to 13:31 UTC

(b) 11:10 to 11:40 UTC
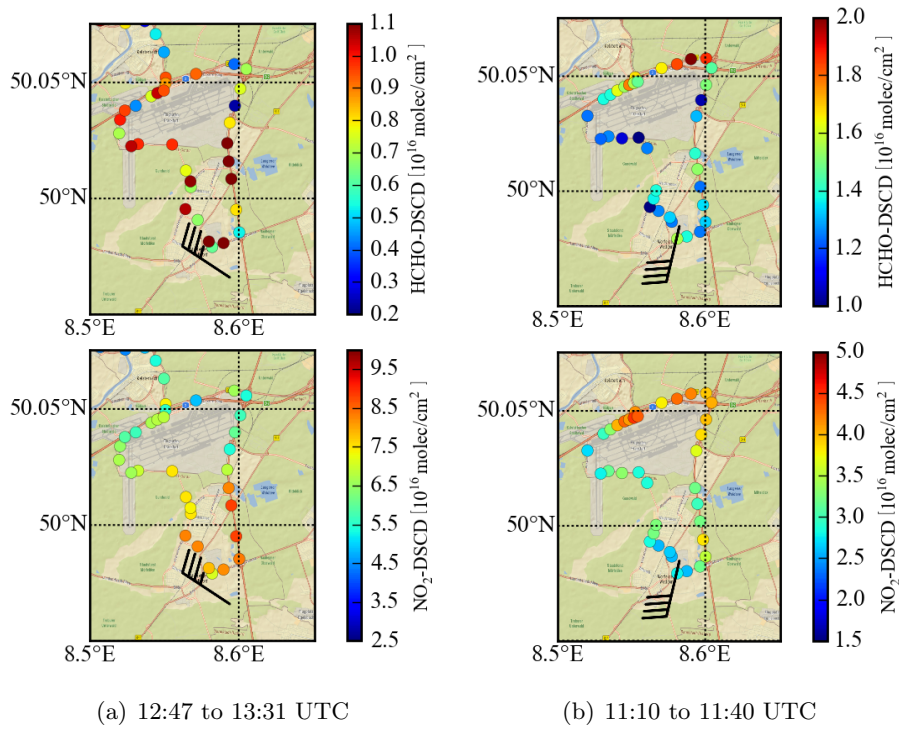
Figure A.36.: Spatial distribution of the HCHO (upper panel) and NO$_2$ (lower panel) DSCDs around the Frankfurt airport on 23$^{\text{th}}$ November 2015 (a) and 20$^{\text{th}}$ December 2015 (b).

(a) 11:39 to 12:47 UTC

(b) 11:26 to 12:42 UTC
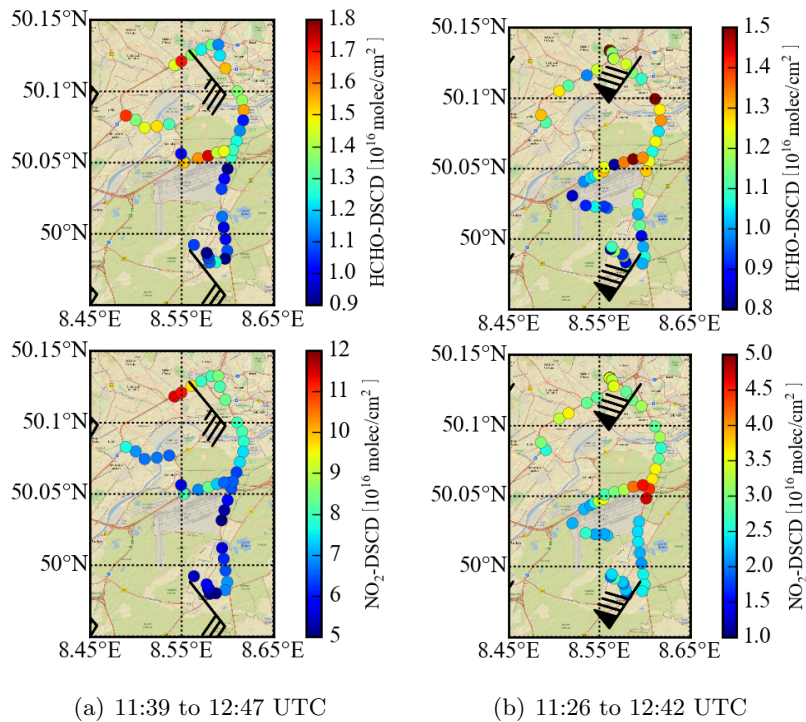
Figure A.37.: Spatial distribution of the HCHO (upper panel) and NO$_2$ (lower panel) DSCDs around the Frankfurt airport on 22$^{\text{nd}}$ (a) and 29$^{\text{th}}$ (b) January 2016.

(a) 12:42 to 13:15 UTC

(b) 10:55 to 11:39 UTC
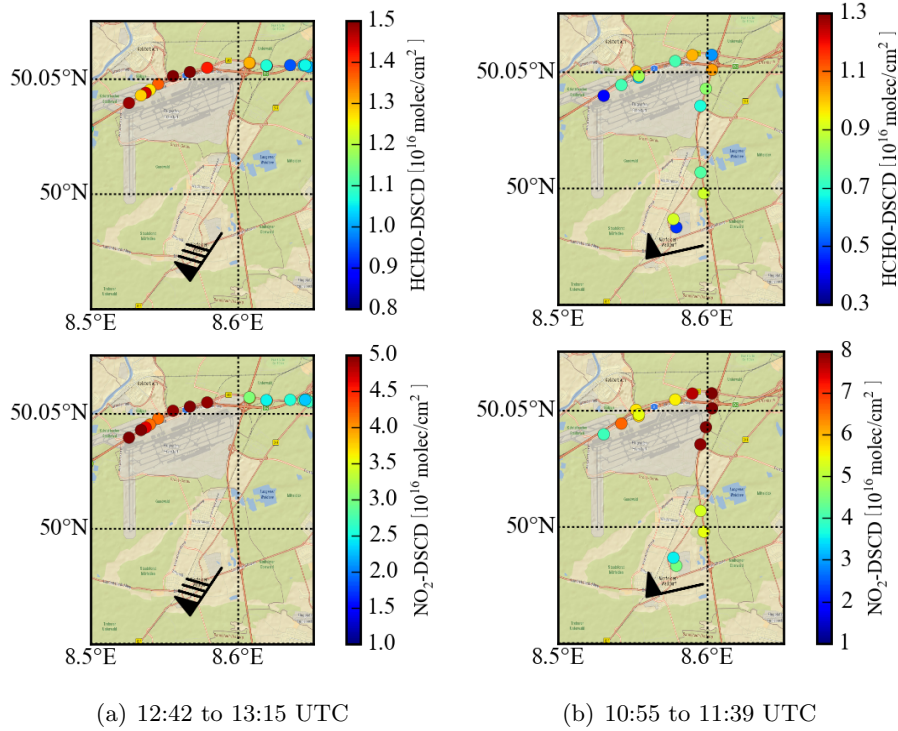
Figure A.38.: Spatial distribution of the HCHO (upper panel) and NO$_2$ (lower panel) DSCDs around the Frankfurt airport on 29th January 2016 (a) and 03rd February 2016.

(a) 10:44 to 11:22 UTC

(b) 12:08 to 12:43 UTC
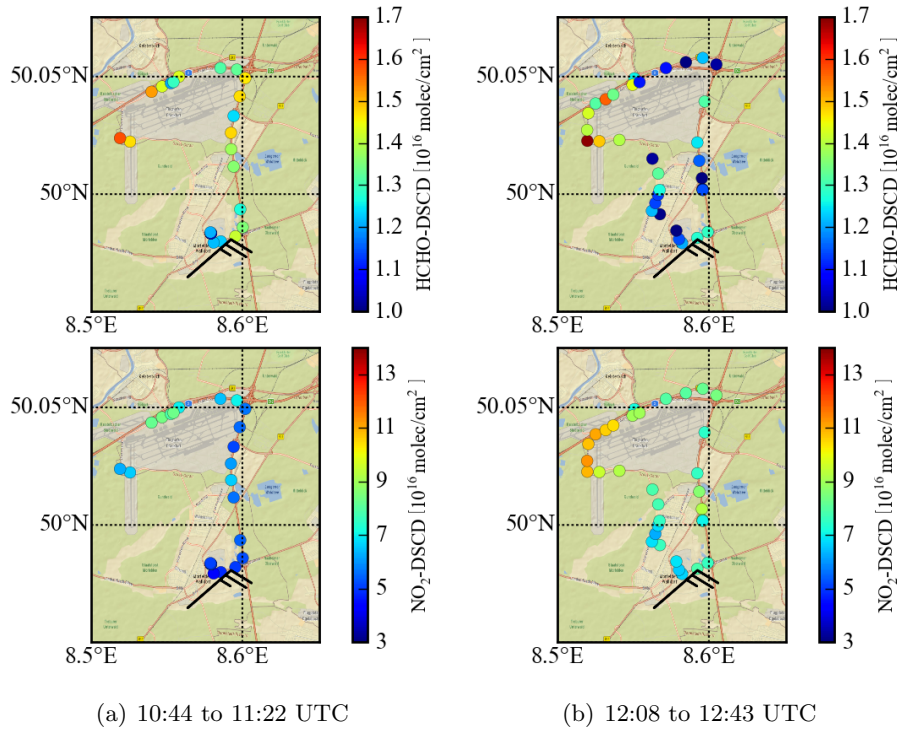
Figure A.39.: Spatial distribution of the HCHO (upper panel) and NO$_2$ (lower panel) DSCDs around the Frankfurt airport on 17th February 2016.

(a) 11:07 to 11:47 UTC   (b) 10:56 to 11:56 UTC
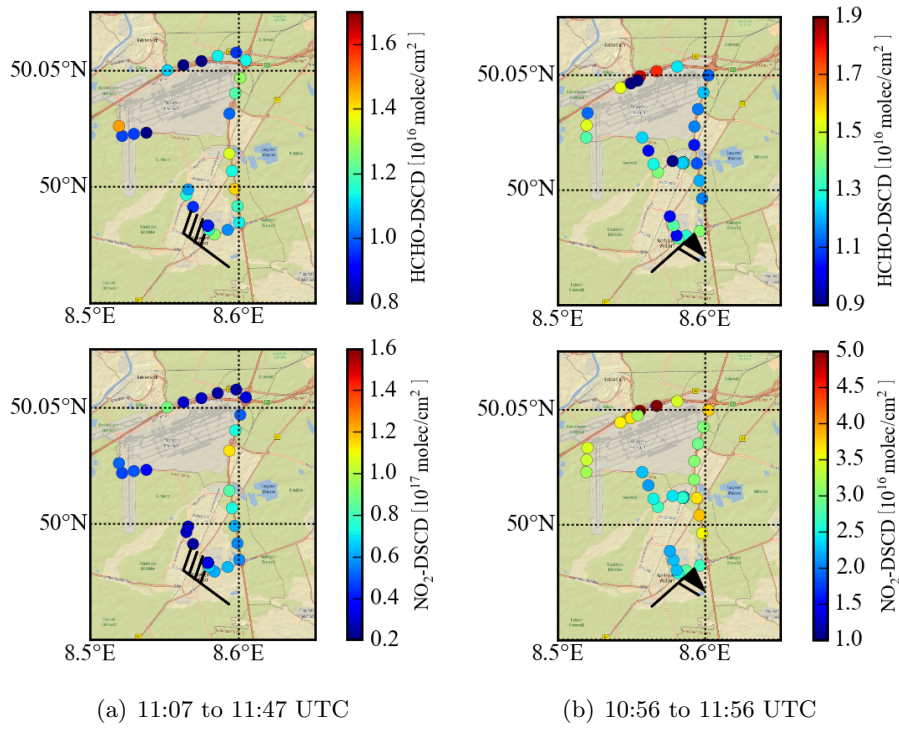
Figure A.40.: Spatial distribution of the HCHO (upper panel) and NO_2 (lower panel) DSCDs around the Frankfurt airport on 25th February 2016 (a) and 14th March 2016.

(a) 12:41 to 13:08 UTC   (b) 11:39 to 13:05 UTC
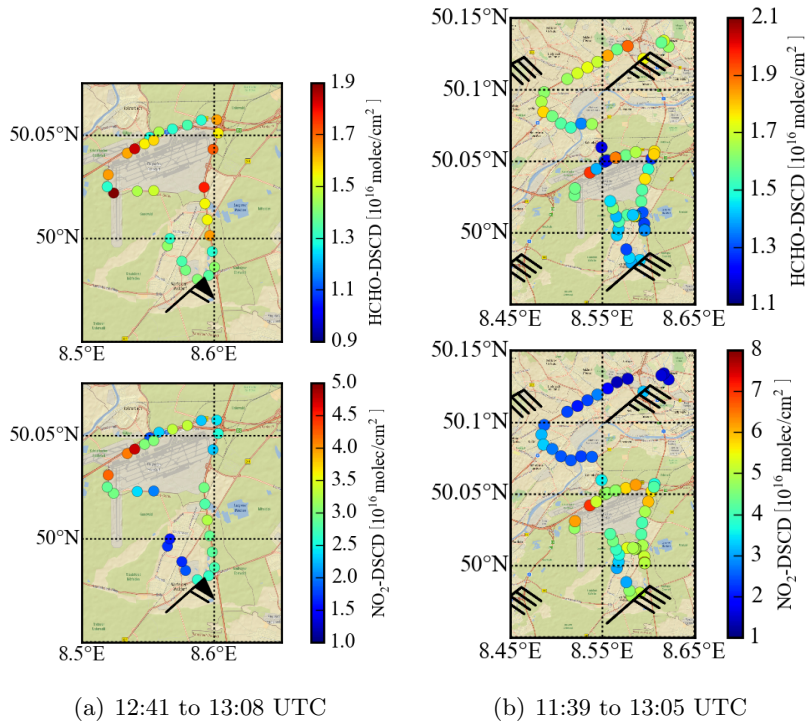
Figure A.41.: Spatial distribution of the HCHO (upper panel) and NO_2 (lower panel) DSCDs around the Frankfurt airport on 14th (a) and 17th (b) March 2016.

A.3. Correlation Plots of HCHO and NO$_2$ for all Days

This section provides an overview on all correlation plots of HCHO and NO$_2$ for all measurement days in the Frankfurt/Rhein-Main region.

A.3.1. DSCDs

(a) 12th October 2015
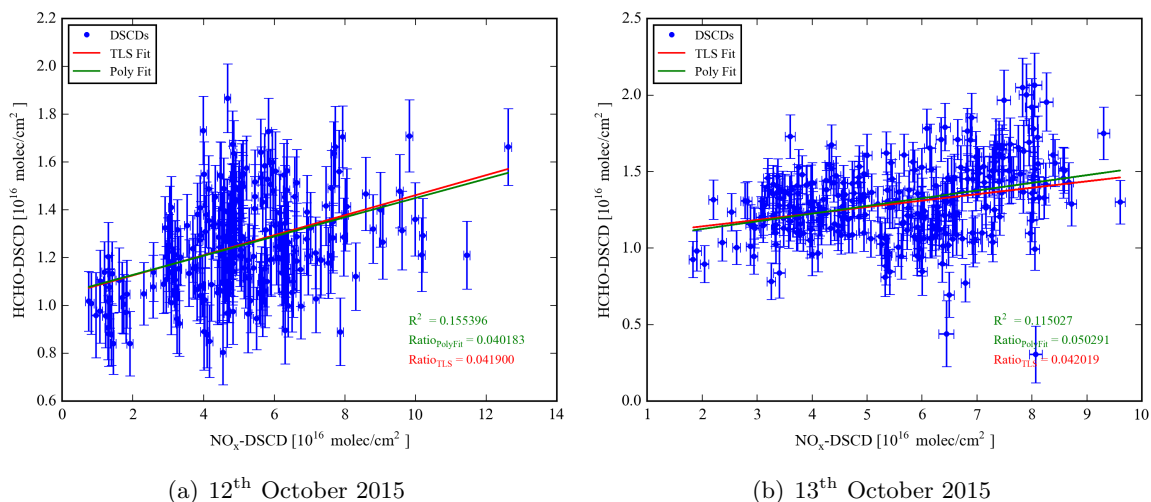
(b) 13th October 2015

Figure A.42.: HCHO-DSCDs plotted against NO$_x$-DSCDs for (a) 12th and (b) 13th October 2015. The regression results are represented by the green and red line, respectively. The emission ratios for the two approaches are indicated by the respective colour.

(a) 27th October 2015
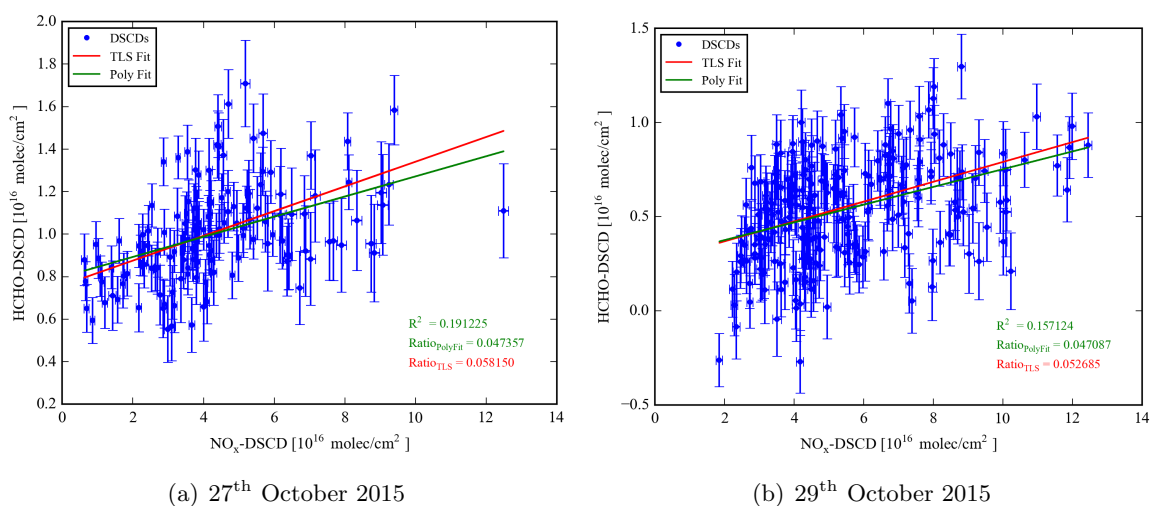
(b) 29th October 2015

Figure A.43.: HCHO-DSCDs plotted against NO$_x$-DSCDs for (a) 27th and (b) 29th October 2015. The regression results are represented by the green and red line, respectively. The emission ratios for the two approaches are indicated by the respective colour.
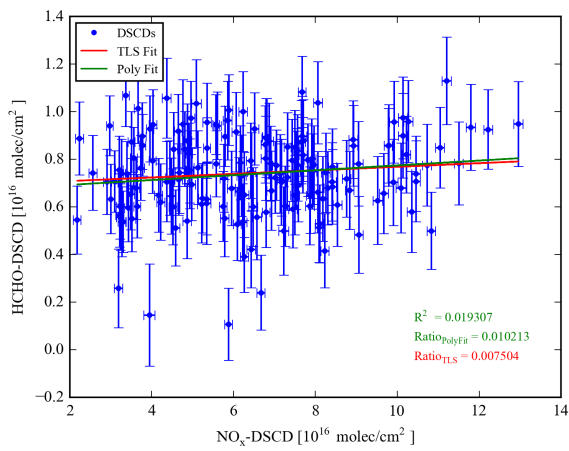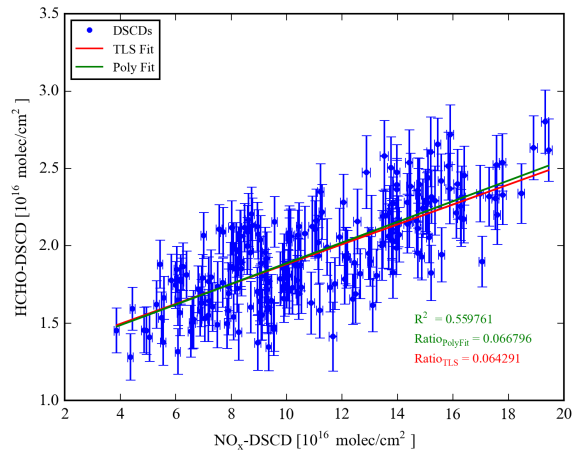
(a) 30$^{\text{th}}$ October 2015

(b) 05$^{\text{th}}$ November 2015

Figure A.44.: HCHO-DSCDs plotted against NO$_x$-DSCDs for (a) 30$^{\text{th}}$ October 2015 and (b) 05$^{\text{th}}$ November 2015. The regression results are represented by the green and red line, respectively. The emission ratios for the two approaches are indicated by the respective colour.
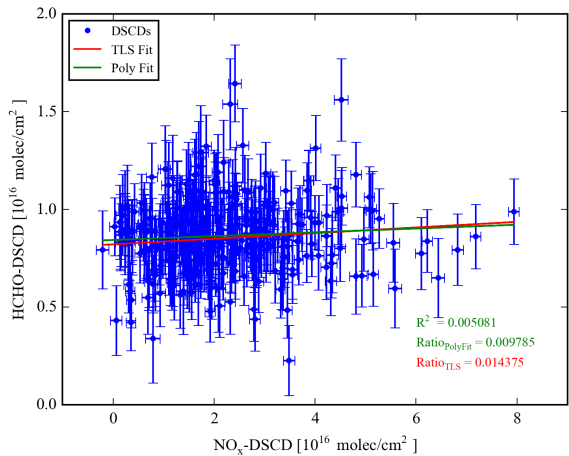
(a) 11$^{\text{th}}$ November 2015
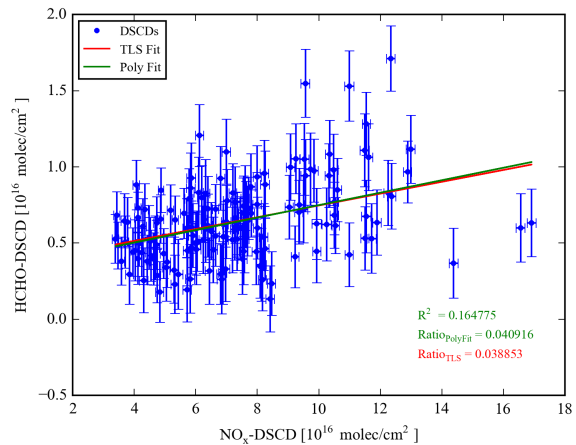
(b) 23$^{\text{rd}}$ November 2015

Figure A.45.: HCHO-DSCDs plotted against NO$_x$-DSCDs for (a) 11$^{\text{th}}$ and (b) 23$^{\text{rd}}$ November 2015. The regression results are represented by the green and red line, respectively. The emission ratios for the two approaches are indicated by the respective colour.
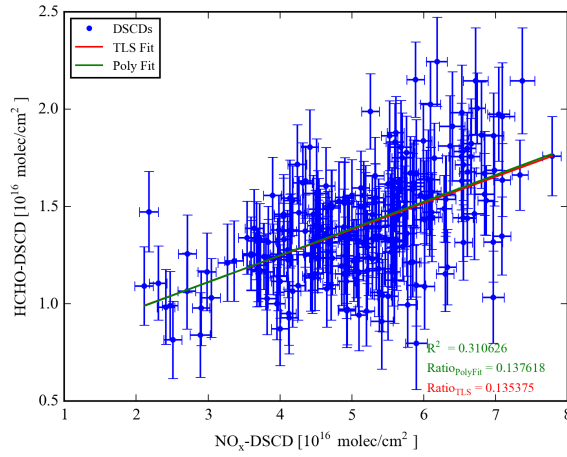
(a) 20$^{\text{th}}$ December 2015
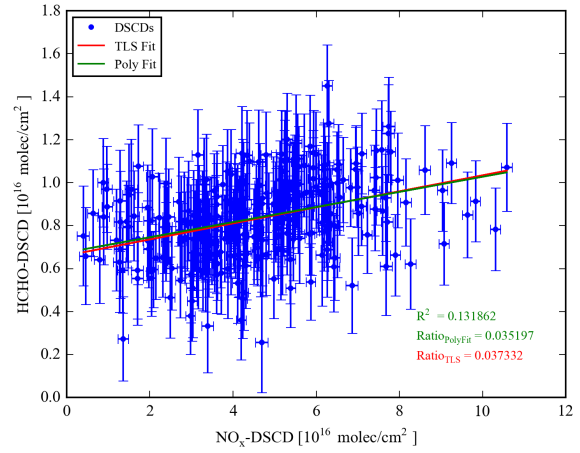
(b) 08$^{\text{th}}$ January 2016

Figure A.46.: HCHO-DSCDs plotted against NO$_x$-DSCDs for (a) 20$^{\text{th}}$ December 2015 and (b) 08$^{\text{th}}$ January 2016. The regression results are represented by the green and red line, respectively. The emission ratios for the two approaches are indicated by the respective colour.
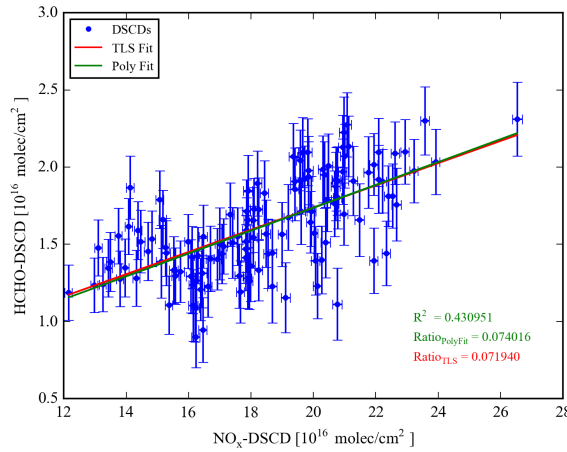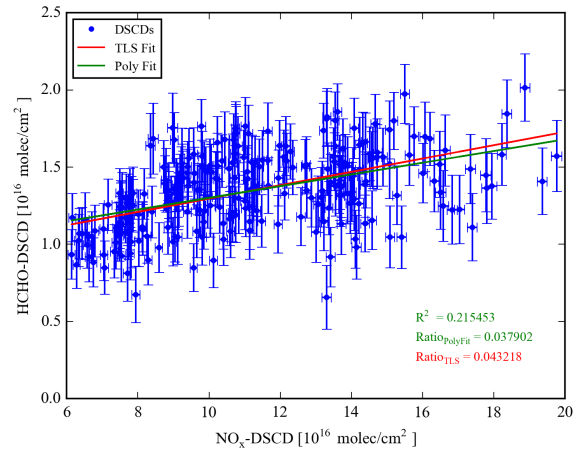
(a) 21$^{\text{st}}$ January 2016

(b) 22$^{\text{nd}}$ January 2016

Figure A.47.: HCHO-DSCDs plotted against NO$_x$-DSCDs for (a) 21$^{\text{st}}$ and (b) 22$^{\text{nd}}$ January 2016. The regression results are represented by the green and red line, respectively. The emission ratios for the two approaches are indicated by the respective colour.
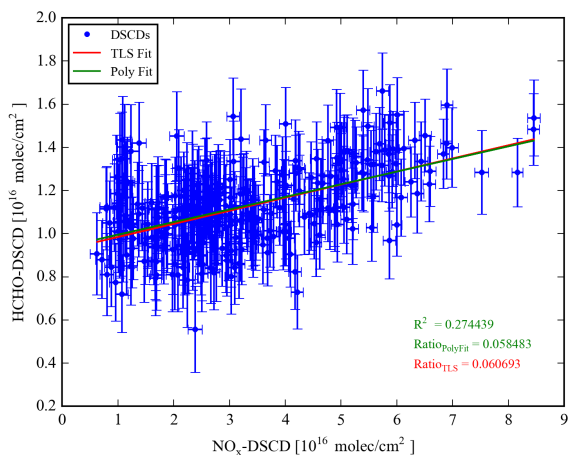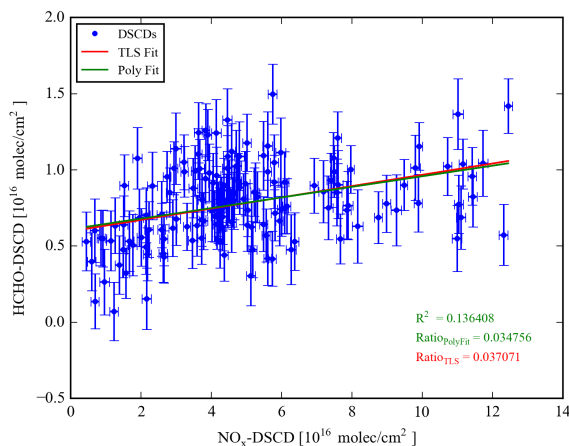
(a) 29$^{\text{th}}$ January 2016

(b) 03$^{\text{rd}}$ February 2016

Figure A.48.: HCHO-DSCDs plotted against NO$_x$-DSCDs for (a) 29$^{\text{th}}$ January 2016 and (b) 03$^{\text{rd}}$ February 2016. The regression results are represented by the green and red line, respectively. The emission ratios for the two approaches are indicated by the respective colour.
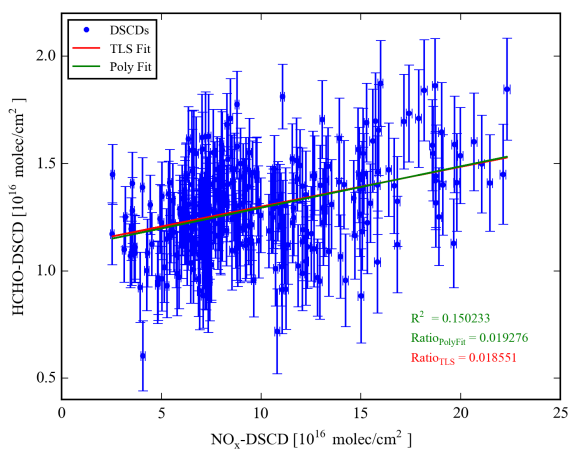
(a) 17$^{\text{th}}$ February 2016
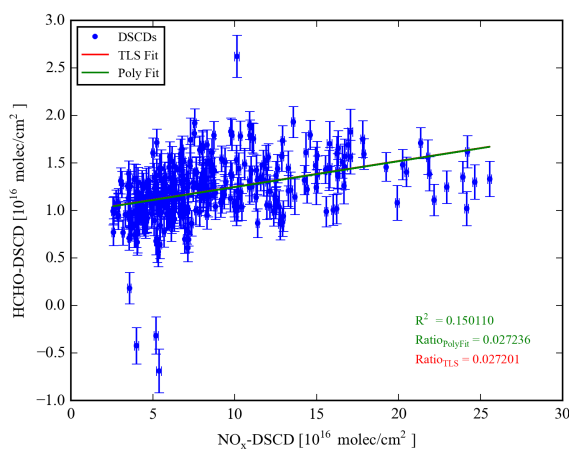
(b) 25$^{\text{th}}$ February 2016

Figure A.49.: HCHO-DSCDs plotted against NO$_x$-DSCDs for (a) 17$^{\text{th}}$ and (b) 25$^{\text{th}}$ February 2016. The regression results are represented by the green and red line, respectively. The emission ratios for the two approaches are indicated by the respective colour.
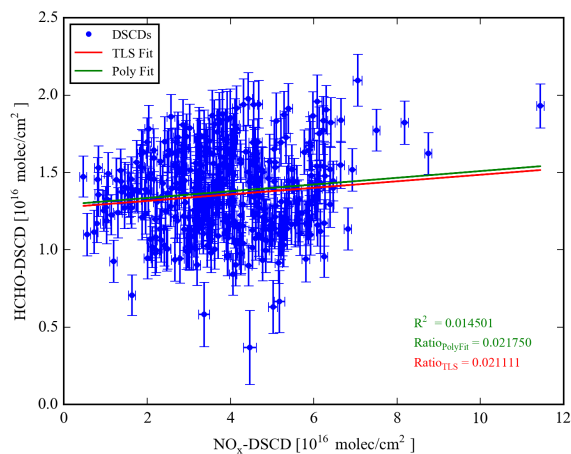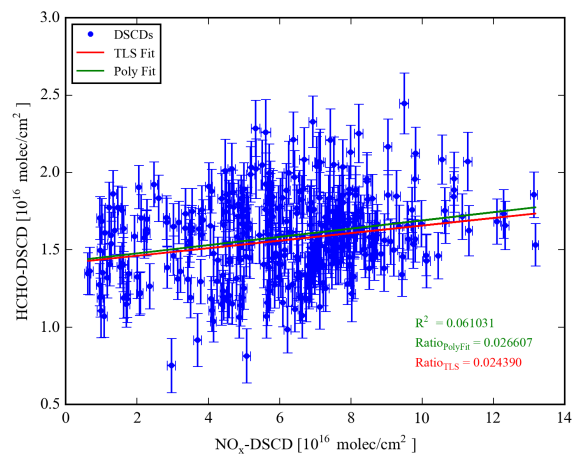
(a) 14th March 2016

(b) 25th March 2016

Figure A.50.: HCHO-DSCDs plotted against NO_x-DSCDs for (a) 14th and (b) 17th March 2016. The regression results are represented by the green and red line, respectively. The emission ratios for the two approaches are indicated by the respective colour.

A.3.2. VCDs

(a) 12th October 2015
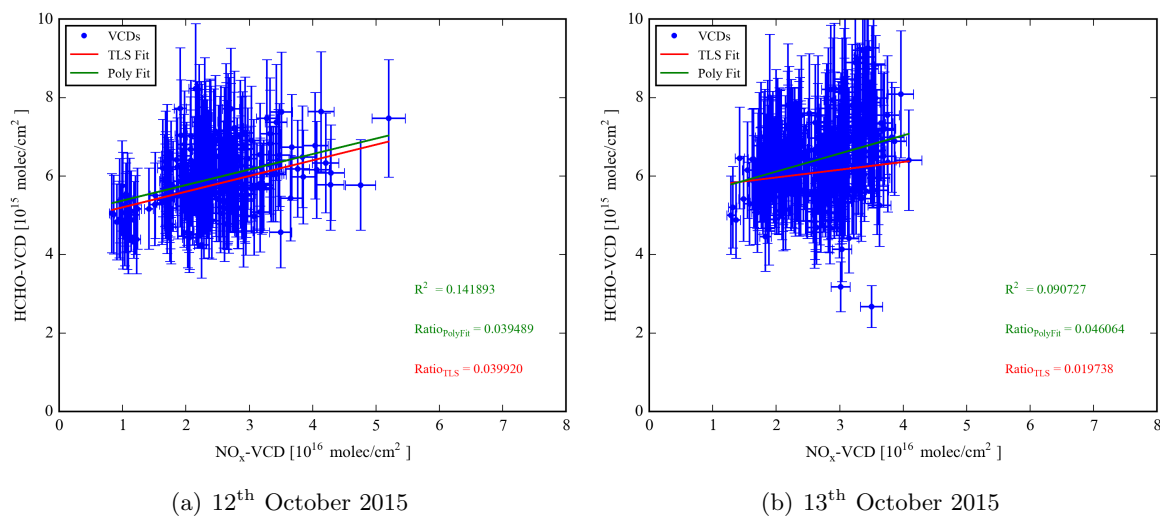
(b) 13th October 2015

Figure A.51.: HCHO-VCDs plotted against NO$_x$-VCDs for (a) 12th and (b) 13th October 2015. The regression results are represented by the green and red line, respectively. The emission ratios for the two approaches are indicated by the respective colour.

(a) 27th October 2015
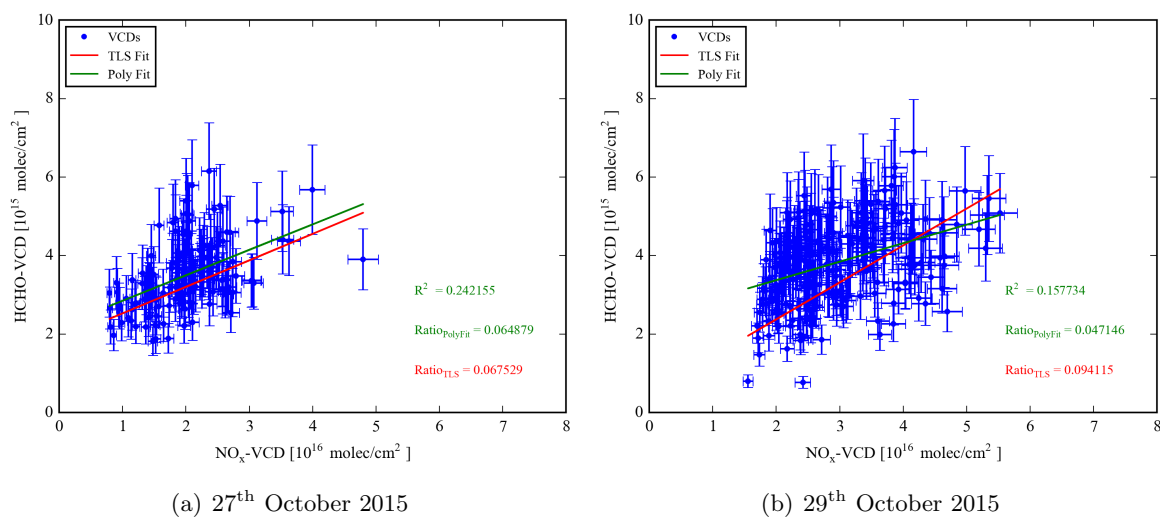
(b) 29th October 2015

Figure A.52.: HCHO-VCDs plotted against NO$_x$-VCDs for (a) 27th and (b) 29th October 2015. The regression results are represented by the green and red line, respectively. The emission ratios for the two approaches are indicated by the respective colour.
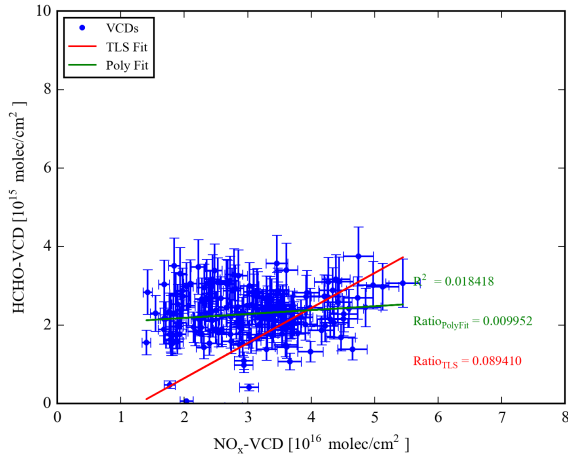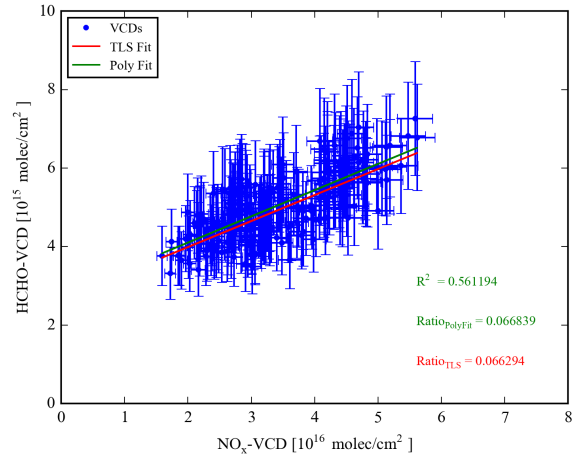
(a) 30th October 2015

(b) 05th November 2015

Figure A.53.: HCHO-VCDs plotted against NO$_x$-VCDs for (a) 30th October 2015 and (b) 05th November 2015. The regression results are represented by the green and red line, respectively. The emission ratios for the two approaches are indicated by the respective colour.
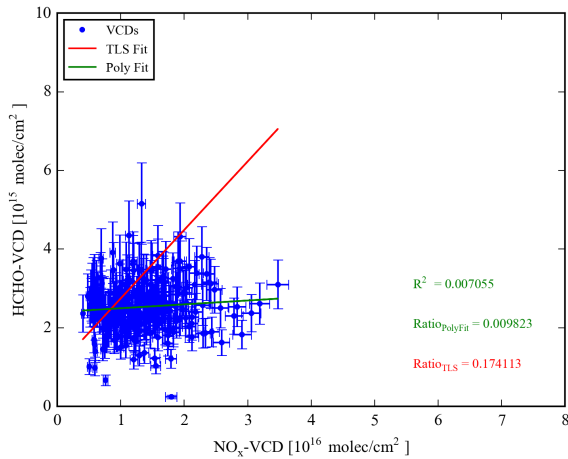
(a) 11th November 2015
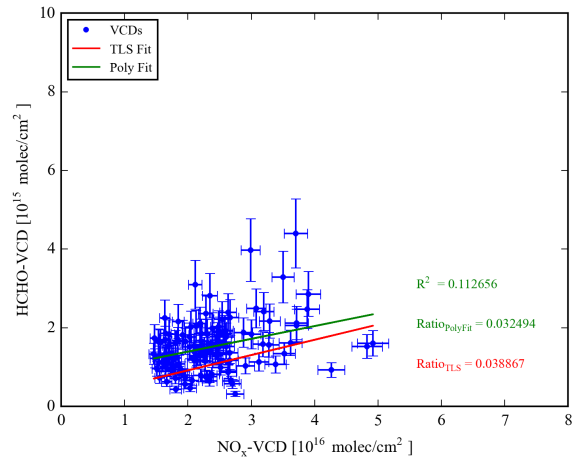
(b) 23rd November 2015

Figure A.54.: HCHO-VCDs plotted against NO$_x$-VCDs for (a) 11th and (b) 23rd November 2015. The regression results are represented by the green and red line, respectively. The emission ratios for the two approaches are indicated by the respective colour.
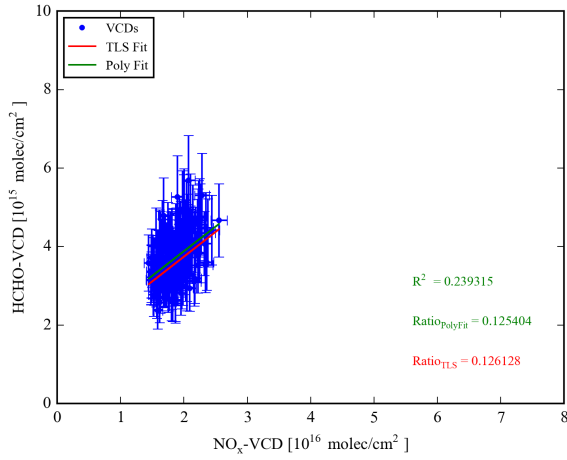
(a) 20$^{\text{th}}$ December 2015
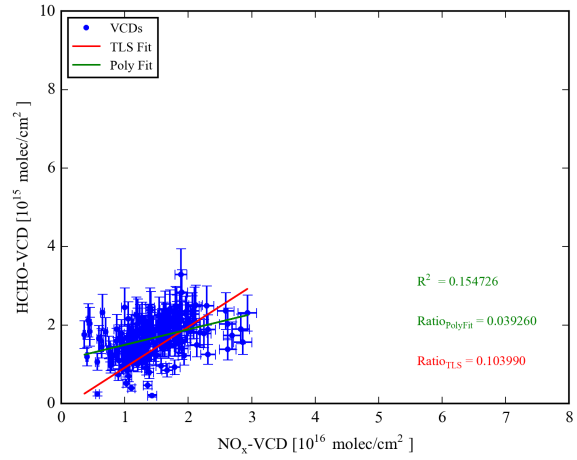
(b) 08$^{\text{th}}$ January 2016

Figure A.55.: HCHO-VCDs plotted against NO$_x$-VCDs for (a) 20$^{\text{th}}$ December 2015 and (b) 08$^{\text{th}}$ January 2016. The regression results are represented by the green and red line, respectively. The emission ratios for the two approaches are indicated by the respective colour.
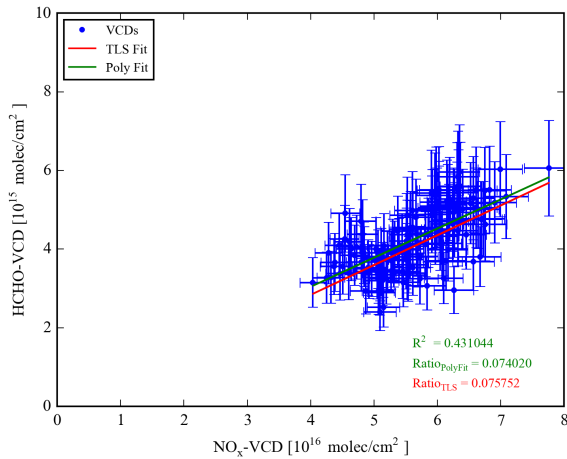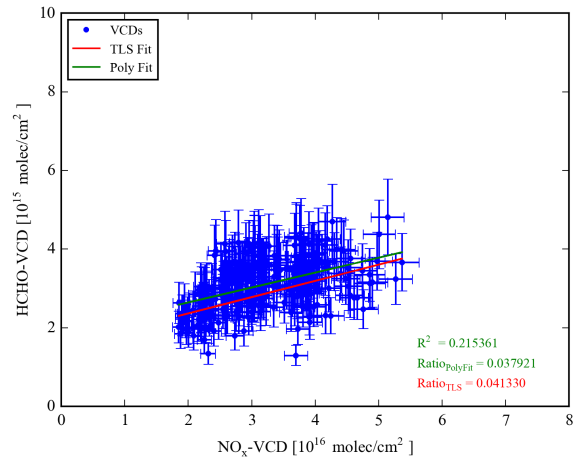
(a) 21$^{\text{st}}$ January 2016

(b) 22$^{\text{nd}}$ January 2016

Figure A.56.: HCHO-VCDs plotted against NO$_x$-VCDs for (a) 21$^{\text{st}}$ and (b) 22$^{\text{nd}}$ January 2016. The regression results are represented by the green and red line, respectively. The emission ratios for the two approaches are indicated by the respective colour.
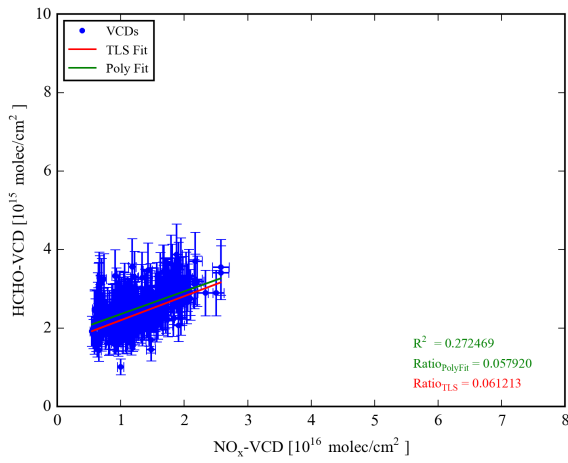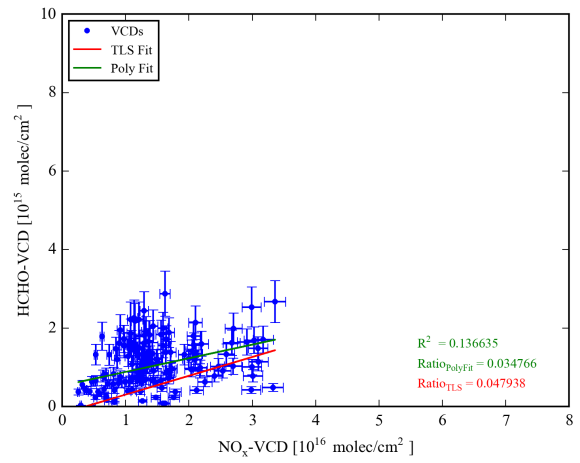
(a) 29$^{\text{th}}$ January 2016

(b) 03$^{\text{rd}}$ February 2016

Figure A.57.: HCHO-VCDs plotted against NO$_x$-VCDs for (a) 29$^{\text{th}}$ January 2016 and (b) 03$^{\text{rd}}$ February 2016. The regression results are represented by the green and red line, respectively. The emission ratios for the two approaches are indicated by the respective colour.
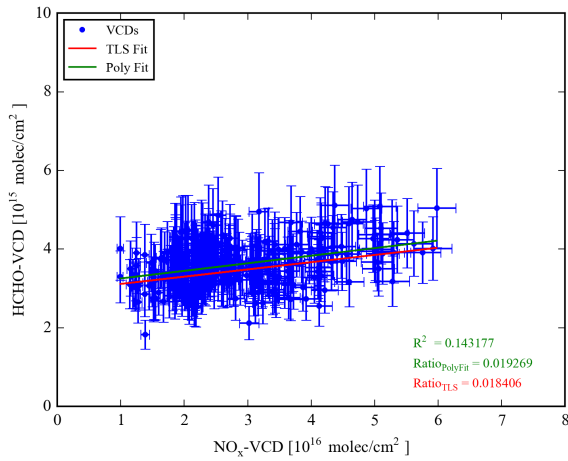
(a) 17$^{\text{th}}$ February 2016
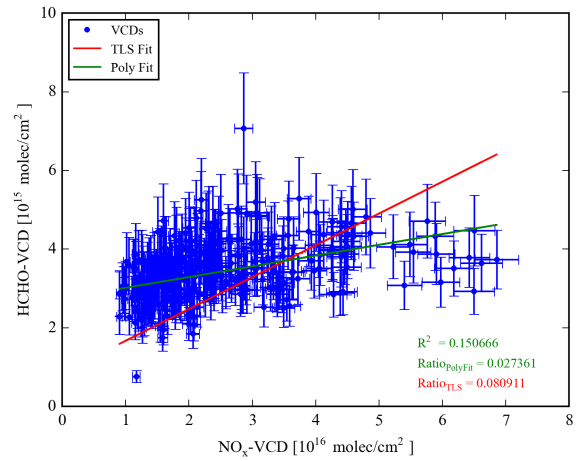
(b) 25$^{\text{th}}$ February 2016

Figure A.58.: HCHO-VCDs plotted against NO$_x$-VCDs for (a) 17$^{\text{th}}$ and (b) 25$^{\text{th}}$ February 2016. The regression results are represented by the green and red line, respectively. The emission ratios for the two approaches are indicated by the respective colour.
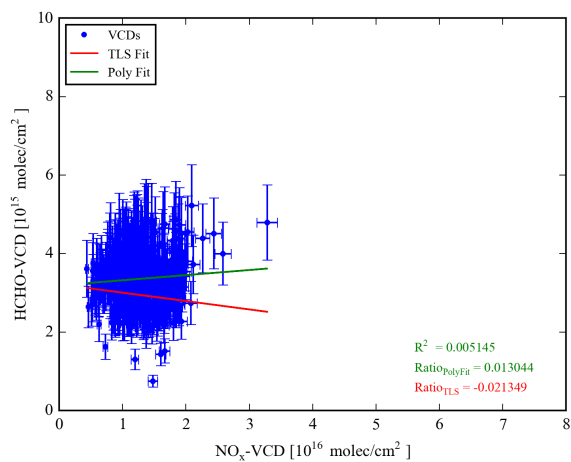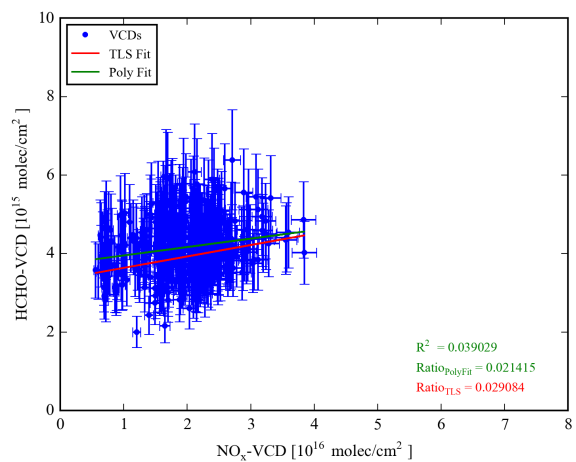
(a) 14$^{\text{th}}$ March 2016   (b) 17$^{\text{th}}$ March 2016

Figure A.59.: HCHO-VCDs plotted against NO$_x$-VCDs for (a) 14$^{\text{th}}$ and (b) 17$^{\text{th}}$ March 2016. The regression results are represented by the green and red line, respectively. The emission ratios for the two approaches are indicated by the respective colour.

A.4. Distribution of HCHO and NO$_2$ around Bucharest

(a) 06:45 to 09:30 UTC

(b) 10:19 to 12:00 UTC
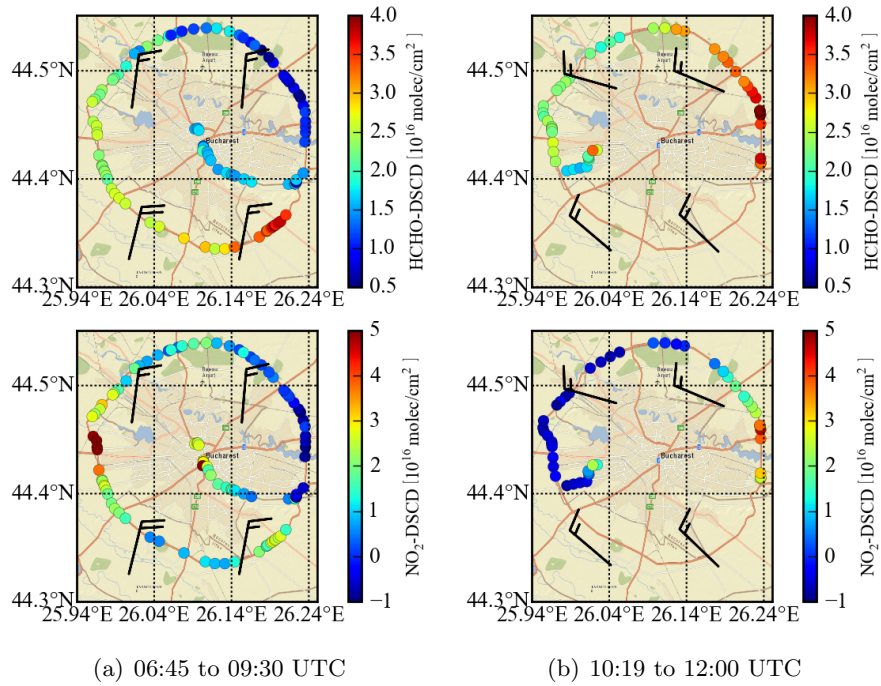
Figure A.60.: Spatial distribution of the HCHO (upper panel) and NO$_2$ (lower panel) DSCDs around Bucharest on 18th August 2015.

(a) 08:22 to 10:13 UTC

(b) 13:16 to 15:09 UTC
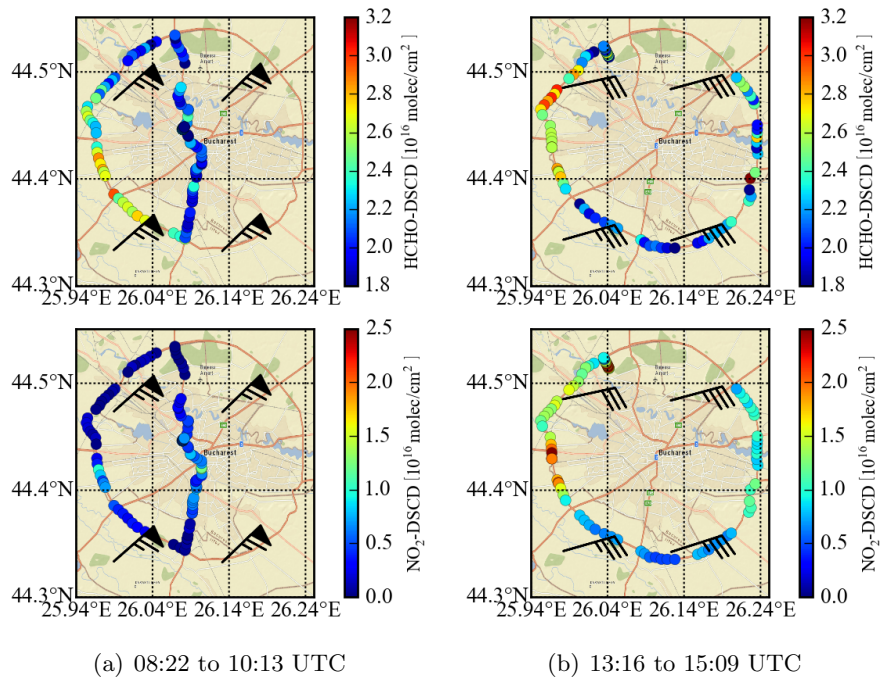
Figure A.61.: Spatial distribution of the HCHO (upper panel) and NO$_2$ (lower panel) DSCDs around Bucharest on 30th August 2015.

(a) 08:00 to 10:30 UTC   (b) 13:00 to 16:00 UTC
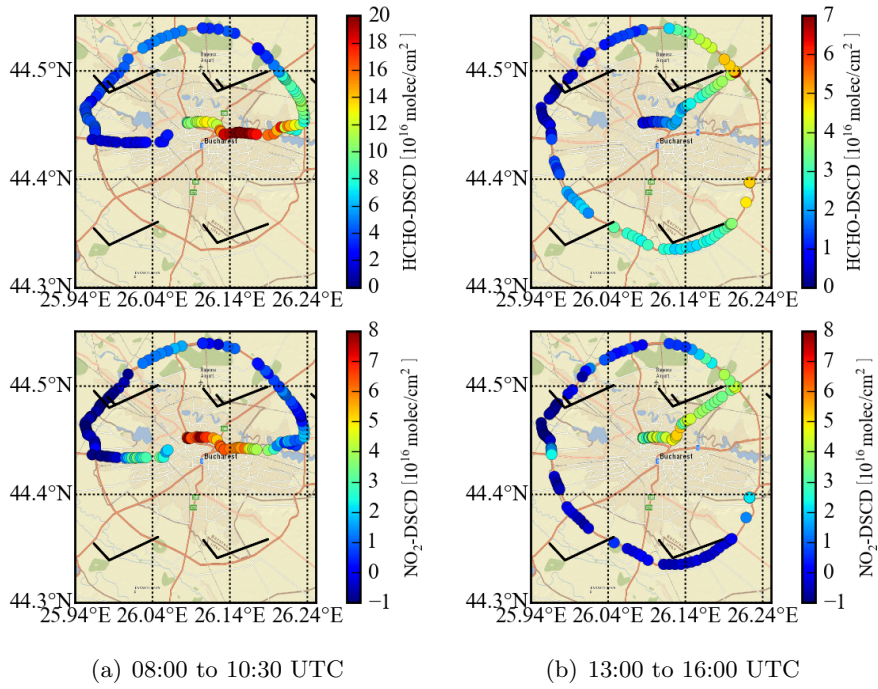
Figure A.62.: Spatial distribution of the HCHO (upper panel) and NO_2 (lower panel) DSCDs around Bucharest on 31th August 2015.

List of Figures

List of Tables

Bibliography

D. Klemp, K. Mannschreck, H. W. Pätz, M. Habram, P. Matuska, and F. Slemr. Determination of anthropogenic emission ratios in the Augsburg area from concentration ratios: results from long-term measurements. *Atmospheric Environment*, 36:61–80, 2002.

J. Slemr, W. Junkermann, and A. Volz-Thomas. Temporal variations in formaldehyde, acetaldehyde and acetone and budget of formaldehyde at a rural site in southern Germany. *Atmospheric Environment*, 30(21):3667–3676, 1996.

Helmut Kraus. *Die Atmosphäre der Erde: Eine Einführung in die Meteorologie*. Springer-Verlag, 2007.

Gerd Hönninger and Ulrich Platt. Observations of BrO and its vertical distribution during surface ozone depletion at Alert. *Atmospheric Environment*, 36(15):2481–2489, 2002.

G. Hönninger, C. von Friedeburg, and U. Platt. Multi axis differential optical absorption spectroscopy (MAX-DOAS). *Atmospheric Chemistry and Physics*, 4:231–254, 2004.

R. Shaiganfar, S. Beirle, Manish Sharma, A. Chauhan, Ramesh P. Singh, and T. Wagner. Estimation of NO_x emissions from Delhi using Car MAX-DOAS observations and comparison with OMI satellite data. *Atmospheric Chemistry and Physics*, 11(21):10871–10887, 2011.

O. Ibrahim, R. Shaiganfar, R. Sinreich, T. Stein, U. Platt, and T. Wagner. Car MAX-DOAS measurements around entire cities: quantification of NO_x emissions from the cities of Mannheim and Ludwigshafen (Germany). *Atmospheric Measurement Techniques*, 3(3): 709–721, 2010.

Ulrich Platt and Jochen Stutz. *Differential Optical Absorption Spectroscopy: Principles and Applications*. Springer, Berlin, 2008.

Andreas Richter and Thomas Wagner. The use of UV, Visible and Near IR solar back scattered radiation to determine trace gases. In *The Remote Sensing of Tropospheric Composition from Space*, pages 67–121. Springer, 2011.

T. Wagner, O. Ibrahim, R. Shaiganfar, and U. Platt. Mobile MAX-DOAS observations of tropospheric trace gases. *Atmospheric Measurement Techniques*, 3:129–140, 2010.

J. Lampel, U. Frieß, and U. Platt. The impact of vibrational Raman scattering of air on DOAS measurements of atmospheric trace gases. *Atmospheric Measurement Techniques*, 8(9):3767–3787, 2015.

John H. Seinfeld and Spyros N. Pandis. *Atmospheric chemistry and physics: from air pollution to climate change.* John Wiley & Sons, 2012.

Barbara J. Finlayson-Pitts and James N. Pitts Jr. *Chemistry of the upper and lower atmosphere: theory, experiments, and applications.* Academic press, 1999.

Reza Shaiganfar. *Estimation of NO_x Emissions from megacities using mobile MAX-DOAS and satellite observations.* Dissertation, Ruprecht-Karls-Universität Heidelberg, 2012.

W. Roedel and T. Wagner. *Physik unserer Umwelt: Die Atmosphäre.* Springer, 2011.

Ralf Koppmann. *Volatile Organic Compounds in the Atmosphere.* Blackwell Publishing, Oxford, 2007.

Gary D. Greenblatt, John J. Orlando, James B. Burkholder, and A. R. Ravishankara. Absorption measurements of oxygen between 330 and 1140 nm. *Journal of Geophysical Research: Atmospheres*, 95(D11):18577–18582, 1990.

A. Heckel, A. Richter, T. Tarsu, F. Wittrock, C. Hak, I. Pundt, W. Junkermann, and J. P. Burrows. MAX-DOAS measurements of formaldehyde in the Po-Valley. *Atmospheric Chemistry and Physics*, 5(4):909–918, 2005.

J. W. Ellis and H. O. Kneser. Kombinationsbeziehungen im Absorptionsspektrum des flüssigen Sauerstoffs. *Zeitschrift für Physik*, 86(9-10):583–591, 1933.

Schott AG. Produkte und Anwendungen, Bandpassfilter. `http://www.schott.com/advanced_optics/german/products/filteroverviewdetail-bandpass-bg-b.html`, February 2016. Accessed: 2016-02-14.

MountainPhotonics GmbH. Hersteller Avantes. `http://www.mountainphotonics.de/hersteller/avantes/`, February 2016. Accessed: 2016-02-14.

Martin Horbanski. *Emissions and Distribution of Reactive Iodine from Seaweed in Coastal Regions - Investigations using new mobile and in-situ DOAS techniques.* Dissertation, Ruprecht-Karls-Universität Heidelberg, 2015.

Johannes Lampel. Personal communication, July 2015.

Sebastian Donner. *Aufbau und Charakterisierung eines MAX-DOAS-Instruments.* Bachelor-Thesis, Johannes Gutenberg University Mainz, 2014.

Avantes BV. Avantes Spectrometers. `http://www.avantes.com/products/spectrometers/`, May 2016. Accessed: 2016-05-18.

Richard Meller and Geert K. Moortgat. Temperature dependence of the absorption cross sections of formaldehyde between 223 and 323 K in the wavelength range 225–375 nm. *Journal of Geophysical Research: Atmospheres*, 105(D6):7089–7101, 2000.

David M. Wilmouth, Thomas F. Hanisco, Neil M. Donahue, and James G. Anderson. Fourier transform ultraviolet spectroscopy of the A$^2\Pi_{3/2} < - $ X $^2\Pi_{3/2}$ transition of BrO. *The Journal of Physical Chemistry A*, 103(45):8935–8945, 1999.

Ann Carine Vandaele, Christian Hermans, Paul C. Simon, Michel Carleer, Réginald Colin, Sophie Fally, Marie-France Merienne, Alain Jenouvrier, and Bernard Coquart. Measurements of the NO$_2$ absorption cross-section from 42 000 cm^{-1} to 10 000 cm^{-1} (238-1000 nm) at 220 K and 294 K. *Journal of Quantitative Spectroscopy and Radiative Transfer*, 59 (3):171–184, 1998.

K. Bogumil, J. Orphal, T. Homann, S. Voigt, P. Spietz, O. C. Fleischmann, A. Vogel, M. Hartmann, H. Kromminga, H. Bovensmann, et al. Measurements of molecular absorption spectra with the SCIAMACHY pre-flight model: instrument characterization and reference data for atmospheric remote-sensing in the 230-2380 nm region. *Journal of Photochemistry and Photobiology A: Chemistry*, 157(2):167–184, 2003.

Ryan Thalman and Rainer Volkamer. Temperature dependent absorption cross-sections of O$_2$–O$_2$ collision pairs between 340 and 630 nm and at atmospherically relevant pressure. *Physical Chemistry Chemical Physics*, 15(37):15371–15381, 2013.

G. Pinardi, M. Van Roozendael, N. Abuhassan, C. Adams, A. Cede, K. Clémer, C. Fayt, U. Frieß, M. Gil, J. Herman, et al. MAX-DOAS formaldehyde slant column measurements during CINDI: intercomparison and analysis improvement. *Atmospheric Measurement Techniques*, 6(1):167–185, 2013.

H. Salow and W. Steiner. Die durch Wechselwirkungskräfte bedingten Absorptionsspektra des Sauerstoffes. *Zeitschrift für Physik*, 99(1-2):137–158, 1936.

Johannes Lampel. *Measurements of reactive trace gases in the marine boundary layer using novel DOAS methods*. Dissertation, Ruprecht-Karls-Universität Heidelberg, 2014.

Hessisches Landesamt für Statistik. Bevölkerung der hessischen Gemeinden. `http://www.statistik-hessen.de/themenauswahl/bevoelkerung-gebiet/regionaldaten/bevoelkerung-der-hessischen-gemeinden/index.html`, April 2016. Accessed: 2016-04-14.

Statistisches Landesamt Rheinland-Pfalz. Statistische Berichte. `http://www.statistik.rlp.de/fileadmin/dokumente/berichte/A1033_201422_hj_G.pdf`, April 2016. Accessed: 2016-04-14.

Eurostat. Bevölkerung nach Geschlecht und Altersgruppen. `http://appsso.eurostat.ec.europa.eu/nui/show.do`, April 2016. Accessed: 2016-04-14.

FRAPORT AG. Verkehrszahlen. `http://www.fraport.de/content/fraport/de/investor-relations/finanz-und-verkehrszahlen/verkehrszahlen.html`, April 2016. Accessed: 2016-04-14.

Steffen Beirle. Personal communication, May 2016.

Acknowledgements